

FR-type radio sources at 3 GHz VLA-COSMOS: Relation to physical properties and large-scale environment

E. Vardoulaki^{1,2,3*}, E. F. Jiménez Andrade^{4,3}, I. Delvecchio^{5,6}, V. Smolčić⁷, E. Schinnerer⁸,
M. T. Sargent⁹, G. Gozaliasi¹⁰, A. Finoguenov¹⁰, M. Bondi¹¹, G. Zamorani¹², T. Badescu³,
S. K. Leslie¹³, L. Ceraj⁷, K. Tisanić⁷, A. Karim³, B. Magnelli³, F. Bertoldi³, E. Romano-Diaz³, K.
Harrington³

¹ Thüringer Landessternwarte, Sternwarte 5, 07778 Tautenburg, Germany

² Max-Planck-Institut für Radioastronomie, Auf dem Hügel 69, 53121 Bonn, Germany

³ Argelander-Institut für Astronomie, Auf dem Hügel 71, D-53121 Bonn, Germany

⁴ National Radio Astronomy Observatory, 520 Edgemont Road, Charlottesville, VA 22903, USA

⁵ INAF - Osservatorio Astronomico di Brera, via Brera 28, I-20121, Milano, Italy & via Bianchi 46, I-23807, Merate, Italy

⁶ CEA, Irfu, DAp, AIM, Université Paris-Saclay, Université de Paris, CNRS, F-91191 Gif-sur-Yvette, France

⁷ Department of Physics, Faculty of Science, University of Zagreb, Bijenička cesta 32, 10000 Zagreb, Croatia

⁸ Max-Planck-Institut für Astronomie, Königstuhl 17, 69117, Heidelberg, Germany

⁹ Astronomy Centre, Department of Physics and Astronomy, University of Sussex, Brighton, BN1 9QH, UK

¹⁰ Department of Physics, University of Helsinki, P. O. Box 64, FI-00014, Helsinki, Finland

¹¹ INAF - Istituto di Radioastronomia, Via Gobetti 101, 40129 Bologna, Italy

¹² INAF-Osservatorio di Astrofisica e Scienza dello Spazio di Bologna, Via Piero Gobetti 93/3, I - 40129 Bologna, Italy

¹³ Leiden Observatory, Leiden University, PO Box 9513, NL-2300 RA Leiden, the Netherlands

Received ; accepted

ABSTRACT

Context. Radio active galactic nuclei (AGN) are traditionally separated in two classes, edge-brightened FR II sources or edge-darkened FR I sources. With the discovery of a plethora of radio AGN of different radio shapes, this dichotomy is becoming too simplistic in linking the radio structure to the physical properties of radio AGN, their hosts and their environment.

Aims. We probe the physical properties and large-scale environment of radio AGN in the faintest FR population to-date, and link them to their radio structure. We use the VLA-COSMOS Large Project at 3 GHz, with resolution and sensitivity of 0".75 and 2.3 μ Jy/beam, respectively, to explore the FR dichotomy down to μ Jy levels.

Methods. We classify objects as FRIs, FRIIs or hybrid FRI/FRII based on the surface-brightness distribution along their radio structure. Our control sample is the jet-less/compact radio AGN (COM AGN) which show excess radio emission at 3 GHz VLA-COSMOS exceeding what is coming from star-formation alone; this sample excludes FRs. Largest angular projected sizes of FR objects are measured by a machine-learning algorithm and also by hand, following a parametric approach to the FR classification. Eddington ratios are calculated using scaling relations from the X-rays, while we include the jet power by using radio luminosity as a probe. We investigate their host properties (star-formation ratio, stellar mass, morphology), and we explore their incidence within X-ray galaxy groups in COSMOS, as well as in the density fields and cosmic-web probes in COSMOS.

Results. Our sample is composed of 59 FRIIs, 32 FRI/FRIIs, 39 FRIs, and 1818 COM AGN at $0.03 \leq z \leq 6$. FR objects have on average similar radio luminosities ($L_{3 \text{ GHz}} \sim 10^{23} \text{ W Hz}^{-1} \text{ sr}^{-1}$), spanning a range of $10^{21-26} \text{ W Hz}^{-1} \text{ sr}^{-1}$, and lie at a median redshift of $z \sim 1$. The median linear-projected size of FRIIs is $106.6_{36.9}^{238.2}$ kpc, larger than of FRI/FRIIs and FRIs by a factor of 2-3. The COM AGN have sizes below 30 kpc, with a median value of $1.7_{1.5}^{4.7}$ kpc. The median Eddington ratio of FRIIs is $0.006_{0.005}^{0.007}$, a factor of 2.5 less than in FRIs and a factor of 2 more than in FRI/FRII. If the jet power is included, the median Eddington ratios of FRII and FRI/FRII increases by a factor of 12 and 15, respectively. FRs reside in their majority in massive quenched hosts ($M_* > 10^{10.5} M_\odot$), with older episodes of star-formation linked to lower X-ray galaxy group temperatures, suggesting radio-mode AGN quenching. Irrespective of their radio structure, FRs and COM AGN are found in all types and density environments (group or cluster, filaments, field).

Conclusions. By relating radio structure to radio luminosity, size, Eddington ratio and large-scale environment, we find that there is a broad distribution and overlap of FR and COM AGN populations. We discuss the need for a different classification scheme, expanding the classic FR classification by taking into consideration the physical properties of the objects rather than their projected radio structure which is frequency-, sensitivity- and resolution-dependent. This point is crucial in the advent of current and future all-sky radio surveys.

Key words. Galaxies: active – Galaxies: nuclei – Galaxies: hosts – Galaxies: jets – Galaxies: groups – Radio continuum: galaxies – Clusters: clusters: intra-cluster medium

1. Introduction

Extragalactic radio sources associated with active galactic nuclei (AGN) have been traditionally classified based on the surface-brightness distribution along their radio structure, following the FR-type classification scheme of [Fanaroff & Riley \(1974\)](#). Edge-brightened sources are deemed FR II and edge-darkened FRI. [Fanaroff & Riley \(1974\)](#) introduced this dichotomy, which was supported by the study of [Owen & Ledlow \(1994\)](#) and [Ledlow & Owen \(1996\)](#), described via the radio luminosity versus optical R -band luminosity diagram. In this diagram, FR IIs are more powerful at radio wavelengths than FR Is. The FR dichotomy was also supported by the study of [Gopal-Krishna & Witta \(2001\)](#) for redshifts $z < 0.5$ and by [Vardoulaki et al. \(2010\)](#) at $z_{\text{med}} \sim 1.25$, with a few exceptions. It has further been suggested that FRI sources will eventually evolve into FR II (e.g. [Gopal-Krishna & Witta, 1988](#); [Kaiser & Best, 2007](#); [Turner & Shabala, 2015](#)), while other studies present different evolutionary paths (e.g. [Kunert-Bajraszewska et al., 2010](#)). The FR morphological dichotomy, is also believed to be a result of interaction of AGN jets with the environment (e.g. [Laing, 1994](#); [Kaiser et al., 1997](#)) or due to mechanisms associated with jet production (e.g. [Meier, 2001](#)).

When it comes to the linear-projected sizes of FR-type objects in the sky, these can vary from sub-kpc/kpc to a few Mpc (e.g. [Blundell et al., 1999](#); [Dabhade et al., 2020](#)). In this wide distribution of sizes, FR IIs are traditionally larger than FR Is. [Gopal-Krishna & Witta \(2001\)](#) describe FR IIs as more powerful, with powerful collimated jets, contrary to FR Is. The reason for the different evolutionary picture in FR II and FRI jets according to [Kunert-Bajraszewska et al. \(2010\)](#) is disruption of the FRI jets when going through the interstellar medium (ISM) of the host, resulting in the loss of energy and forbidding them from forming large FR II jets.

FR objects are also categorised based on the properties of the black hole and how efficient accretion onto the supermassive black hole (SMBH) is. FR IIs are in their majority high-excitation radio galaxies while FR Is are mainly low-excitation radio galaxies ([Kauffmann et al., 2008](#); [Smolčić, 2009](#); [Best & Heckman, 2012](#)). Thus FR IIs are thought to follow a model with efficient near-Eddington accretion onto the SMBH, described well by the unified AGN model ([Heckman & Best, 2014](#)). FR Is are related to inefficient sub-Eddington accretion onto the SMBH, an advection dominated accretion flow (ADAF), giving rise to FRI-type jets ([Heckman & Best, 2014](#)). This division regarding accretion modes is supported by studies of bright-to-moderately faint (~ 100 mJy at 151 MHz) radio samples (e.g. [Mingo et al., 2014](#); [Fernandes et al., 2015](#)). When studying the intrinsically fainter radio universe, this division starts to disappear with FR II and FRI sources exhibiting sub-Eddington ratios and no clear division (e.g. [Lusso et al., 2012](#)).

More recent studies of radio AGN have revealed a plethora of radio structures which deviate from a straight radio structure, introducing additional classifications, e.g. head-tail, one-sided, wide-/narrow-angle-tail, core-jet, core-lobe, twin-jet, fat-double, classic-double radio source, compact, jet-less, even FR 0 (e.g. [Sadler, 2016](#)). Furthermore, as we explore the faint radio universe in enhanced sensitivity and resolution, we discover radio sources which do not follow the FR-type classification. For instance, using a sample at $z < 0.1$, [Gendre et al. \(2013\)](#) find that there is no dependence of radio structure on radio luminosity but rather an overlap of populations (see their Fig. 8). [Mingo et al. \(2019\)](#) also find a population of 3CR FR sources observed with

LOFAR not following the classic FR dichotomy, with FR IIs observed up to 3 orders of magnitude fainter than the traditional FR break in radio luminosity and their hosts being fainter than expected. These studies suggest that FR class does not correlate with host properties.

From the literature, it is evident that the small-scale environment plays a role in shaping the radio structure of extended AGN. By small-scale environment we can either refer to the SMBH and feeding processes or the ISM. At the same time, the large-scale environment has also been shown to play a role, with more radio luminous sources occupying massive and passive hosts (e.g. [Vardoulaki, 2009](#); [Willott et al., 2003](#); [Vardoulaki, 2013](#)), and preferring denser environments, such as galaxy clusters (e.g. [Magliocchetti et al., 2018](#)). Past studies have shown that FR Is prefer richer environments than FR IIs at low redshifts $z < 0.5$ (e.g. [Zirbel et al., 1997](#), at 408 MHz), at $z < 0.3$ (e.g. [Gendre et al., 2013](#), at 1.4 GHz) and at higher redshifts $1 < z < 2$ ([Castignani et al., 2014](#); [Chiaberge et al., 2009](#), at 1.4 GHz). Recent reviews suggest we should consider and study the AGN phenomenon as an interplay between small and large scales, through a self-regulated approach ([Gaspari et al., 2020](#)). It is clear that the AGN phenomenon and the different types of extended radio AGN, classified via the FR-type classification scheme, are not fully understood nor is the relation of AGN with their hosts and large-scale environment. AGN have an effect on their hosts and environment through feedback mechanisms, which were introduced in models to constrain galaxy growth and avoid having overly massive galaxies in the local universe (e.g. the Illustris TNG simulation [Weinberger et al., 2018](#)). Feedback can be either positive, enhancing star formation or negative, quenching star formation (see [Fabian, 2012](#), for a review). The mechanisms in play involve radiative-mode and kinetic/jet-mode feedback, with the latter needed to explain quenching of star formation (SF) in massive galaxies as the maintenance mode of feedback ([Fabian, 2012](#)), and the suppression of cooling flow in massive cluster cores ([Fabian, 2003](#)). Recent studies (e.g. [Lacerda et al., 2020](#)) are showing that the main role of AGN in quenching is believed to be the removal and/or heating of the molecular gas instead of an additional suppression of star formation. Thus the role of AGN is strongly linked to decreasing the molecular gas fraction of their host galaxies leading to quenching of star formation.

As some studies find the brightest radio AGN, thus FR IIs to reside in massive hosts within clusters, while others find that FR Is should reside in denser environments, the picture on the relation of radio structure, physical properties and environment is still under debate. To better understand what affects the structure of radio sources, we need to carry out a systematic study of the radio structure and host/BH properties, and large-scale environment of radio galaxies at both high resolution and sensitivity levels. For this purpose we use the 3 GHz VLA-COSMOS Large Project ([Smolčić et al., 2017a](#)) and extensive auxiliary data for the COSMOS¹ field, which cover a wide range of multi-wavelength properties and environmental probes, essential to performing such a study.

With this paper we investigate the reason for the different radio structures associated with AGN, whether the FRI/FR II dichotomy is present at μJy flux densities for median $z \sim 1$, and how the radio structure links to the physical properties of the sources and the large-scale environment. In Sec. 2, we present the sample. In Sec. 3, we present the analysis related to the physical properties and environment of the sources in our sample as

* email: elenivard@gmail.com

¹ <http://cosmos.astro.caltech.edu>

well as the results of this analysis: linear-projected size and radio luminosity in Sec. 3.1; Eddington ratio in Sec. 3.2; hosts and large-scale environment in Sec. 3.3. In Sec. 4, we discuss our findings and relate our results to the literature. Sec. 5 presents our conclusions. In Appendix A, we present a parametric approach to the FR classification, in Appendix B we provide notes on the objects and in Appendix C we present a semi-automatic method to measure the largest projected angular size of a radio source.

Throughout this paper we use the convention for all spectral indices, α , that flux density $S_\nu \propto \nu^{-\alpha}$, where ν is the observing frequency. Also, a low-density, Λ -dominated Universe in which $H_0 = 70 \text{ km s}^{-1} \text{ Mpc}^{-1}$, $\Omega_M = 0.3$ and $\Omega_\Lambda = 0.7$ is assumed throughout.

2. Sample selection and radio classification

Our sample is drawn from the VLA-COSMOS 3GHz Large Project (Smolčić et al., 2017a, 3 GHz VLA-COSMOS henceforth), observed with the *Karl J. Jansky* Very Large Array (VLA) in S-band (centred at 3 GHz with a bandwidth of 2,048 MHz). The 3 GHz mosaic extends beyond the COSMOS field covering 2.6 deg^2 at a resolution of 0.75 arcsec, while the median *rms* in the 2 deg^2 of the COSMOS field is $\sim 2.3 \mu\text{Jy}/\text{beam}$. Details on the observations and data reduction can be found in Smolčić et al. (2017a). The source extraction was performed using the algorithm BLOBCAT (Hales et al., 2012) which yields $\sim 11,000$ islands of radio emission or radio blobs. The final catalogue contains 10830 sources, 67 of which are multi-components, i.e. composed of two or more radio blobs (see Vardoulaki et al., 2019, for detailed description), while the rest are single-component sources (Smolčić et al., 2017a).

The aim of this paper is to study the FR-type radio sources in the 3 GHz VLA-COSMOS survey and explore the FR dichotomy. To identify which sources are extended amongst the 10830 radio sources in VLA-COSMOS we use the BLOBCAT size estimate parameter, R_{EST} , which provides an estimate for the size of each island/blob identified by the algorithm. The R_{EST} parameter is not intended to be used for quantitative analysis but can be useful to identify blobs that exhibit complex morphology. In Vardoulaki et al. (2019) we provide a detailed description of this selection, which we will briefly mention here. We select, based on the diagram in Fig. 1, the sources that lie above the envelope given by the relationship $R_{\text{EST}} > 1+30/(S/N)$. This envelope was chosen in order to include the most extended and brightest sources identified by BLOBCAT. This selection yields 351 blobs, which were visually inspected and matched to 350 sources. The matching procedure is described in detail in Vardoulaki et al. (2019).

2.1. FR classification

We provide an FR-type classification based on the radio structure at 3 GHz, taking advantage of the COSMOS auxiliary data to identify the host galaxy. The host identification was done by visually crossmatching the radio core of galaxies with the optical/infrared stacked *YJHK_S* image from the Ultra Deep Survey with the VISTA telescope (Ultra-VISTA; see Laigle et al., 2016; Smolčić et al., 2017b, and references therein), including regions observed at z^{++} with an upgrade of the Subaru Suprime-Cam (see Taniguchi et al., 2007; Smolčić et al., 2017b; Taniguchi et al., 2015).

The 350 radio sources within the envelope in Fig. 1 were classified by visual inspection in three stages. At stage one they

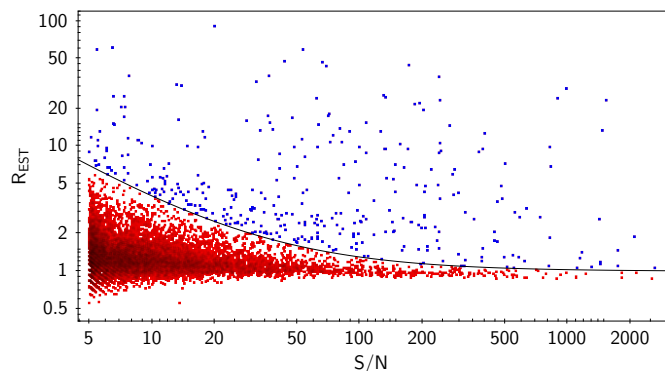


Fig. 1: R_{EST} parameter (a unit-less size estimate from BLOBCAT; Hales et al., 2012) versus signal-to-noise ratio (SNR) for the 10899 entries in the BLOBCAT catalogue identified from the 3 GHz mosaic of the COSMOS field. The black solid line gives the sources that obey the relation $R_{\text{EST}} > 1+30/(S/N)$ and were visually inspected

were given to a team of non-experts on radio AGN with a set of guidelines. These guidelines (see Sec. A.1) described how to separate visually the FRI, FRII, hybrid FRI/FRII and non-FR-type radio sources, based on the FR classification scheme (Fanaroff & Riley, 1974). The second stage of FR classification was a revision of the results from the first stage, and a selection by two experts on FR-type radio sources of a sub-sample of 130 objects which exhibit jets and lobes². These were taken to stage three, where we manually measured the distribution of flux-density along their structure based on the following criteria:

1. FRIIs or edge-brightened: the distance from the core to the brightest point along their structure is more than half of the total size of the source; these objects exhibit lobes (e.g. source 10902 in Fig. 2). Single lobed and one-side lobed objects are placed in this category.
2. FRIs or edge-darkened: the distance from the core to the brightest point along their structure is less than half of the total size of the source; these objects exhibit jets (e.g. source 80 in Fig. 2). Core-single-jet and wide-angle-tail objects are placed in this category.
3. FRI/FRII: this is a hybrid object with one side being an FRII and the other an FRI (e.g. source 10910 in Fig. 2).

This classification yields 59 FRIIs, 32 FRI/FRIIs and 39 FRIs. A detailed description on the FR classification is given in Appendix A, and the final classification is presented in Table A.1; a question-mark is used in the case of uncertain classification. In Table C.1, we report the 3 GHz FR classification, and present for comparison the 1.4-GHz radio classification (Schinnerer et al., 2010). Notes on the objects are given in the Appendix B. 46 out of the 130 radio sources in our sample are classified as FRI, FRII, or wide-angle-tail (WAT) based on the 1.4 GHz data. The rest lack an FR-type classification. The 3 GHz include 13 extra objects which are not identified at 1.4 GHz. These lie in masked areas or outside the coverage of the 1.4-GHz observations.

For the purposes of our analysis we compare the FR sample at 3 GHz to a control sample of radio AGN with compact or jet-less radio structure, i.e. objects that do not exhibit lobes

² The 220 objects which were excluded from the FR sample did not show any signs of radio jets or lobes at 3 GHz. These can be a combination of SFGs and COM AGN. We select the COM AGN from this sub-sample via the radio excess flag (Delvecchio et al., 2017) and use them in our analysis.

or jets in their radio structure but are associated with an AGN. These were selected on the basis of their radio excess (Delvecchio et al., 2017): i.e. radio emission which exceeds that coming from star formation alone (Smolčić et al., 2017b, see their Fig. 7-Top). From these radio excess objects we exclude all extended jet/lobed objects which were identified by cross-matching the FR sample to the radio-excess sample, and additionally performing visual inspection. The final sample of compact AGN (COM AGN henceforth) yields 1818 objects.

The radio-excess selection is a rather conservative selection for radio AGN, which requires the ratio³ of radio luminosity to the star-formation rate (SFR⁴; $L_{1.4\text{GHz}}/\text{SFR}_{\text{IR}}$) to be 3σ the median value (Delvecchio et al., 2017). As a result, we might be missing low-luminosity radio AGN with compact radio structure. The latter are not possible to distinguish from star-forming radio sources via visual inspection as they show no clear signs of radio jets. Including these objects requires another approach and different AGN diagnostics than that this study is using. Thus our COM AGN sample is not complete, but missing low luminosity compact radio AGN.

One important point we need to mention is that, had we selected FR objects based on their radio excess, we would have missed $\sim 6\%$ of the FR objects in our sample, as they fall below the radio excess cut of Delvecchio et al. (2017). This can be visually seen in Fig. 3-Bottom where FR objects without radio excess are marked as squares. These are randomly distributed in the $L - z$ plane of Fig. 3-Bottom. The radio excess flag is given in Table C.1.

Finally, we note that due to the surface brightness decreasing with redshift, we are only sensitive to bright sources as redshift increases, which will have an effect on how many FR sources we are able to detect at higher redshifts and thus limiting our sample.

2.2. Multi-wavelength data

We make use of the 3 GHz VLA-COSMOS counterparts identified by Smolčić et al. (2017b), who associate the 3 GHz radio sources to their hosts by using a multi-wavelength approach. Basic properties for the hosts are listed in Table C.1 (redshift) and Table C.2 (SFR and stellar mass). The SFR and M_* used in this analysis are calculated by Delvecchio et al. (2017) after fitting the multi-wavelength SED with MAGPHYS (da Cunha et al., 2008) and the three-component SED-fitting code SED3FIT by Berta et al. (2013), which accounts for an additional AGN component. Shortly, they exploit the optical to mid-infrared photometry from the COSMOS2015 catalogue (Laigle et al., 2016). To constrain the far-infrared part of the SED, they further include *Herschel* PACS (Lutz et al., 2011) and SPIRE (Oliver et al., 2012) data. For the higher redshift galaxies they use a large dataset of sub-millimetre (sub-mm) photometry from JCMT/SCUBA-2, LABOCA, Bolocam, JCMT/AzTEC, MAMBO, ALMA, and PdBI (see Sect. 2.2 in Delvecchio et al., 2017, for references and discussion). For classification purposes, they also make use of the Chandra-COSMOS (Elvis et al., 2009; Civano et al., 2012) and COSMOS-Legacy (Civano et al., 2016) X-ray catalogues.

We further cross-correlate our FR and COM AGN samples with the most up-to-date X-ray group catalogue for the COSMOS field, from Gozaliasl et al. (2019), which is an updated version of the George et al. (2011) X-ray group catalogue. By

³ No redshift-dependent threshold was applied.

⁴ Derived by fitting the spectral energy distribution (SED; Delvecchio et al., 2017; Smolčić et al., 2017b).

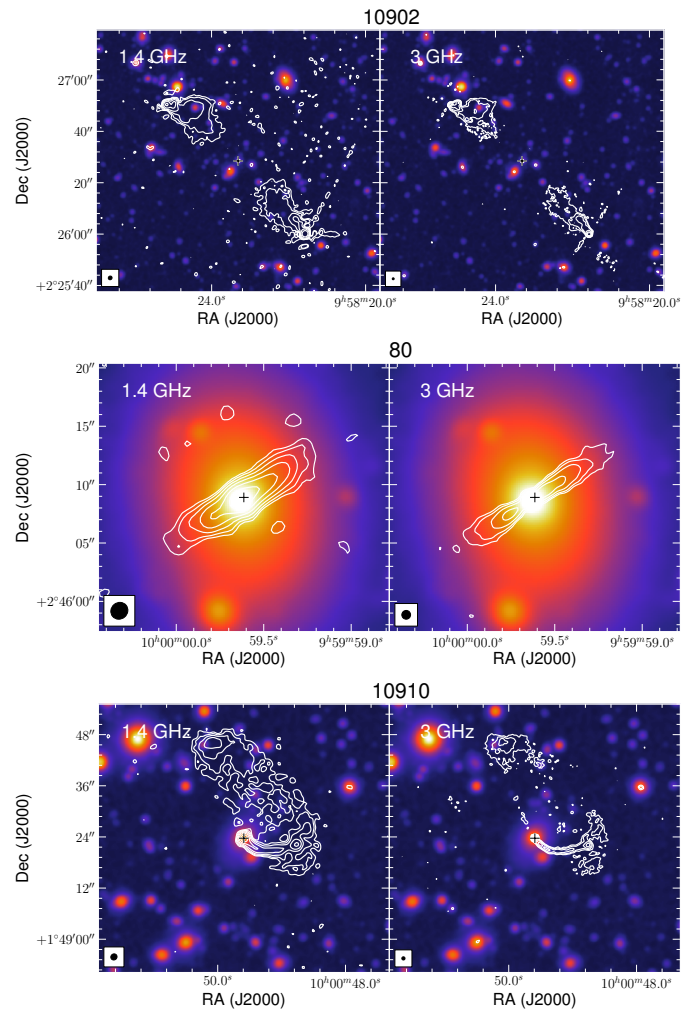


Fig. 2: Set of 1.4-GHz VLA (left) and 3 GHz VLA (right) stamps for examples of FR II (top), FR I (middle), and FR I/FR II (bottom) objects, shown as white contours. These are overlaid on the Ultra-VISTA near-IR stacked image shown in colour-scale in arbitrary units. The beam size for the radio observations is shown at the bottom-left corner of the stamp: $1.4 \times 1.5 \text{ arcsec}^2$ for the 1.4 GHz and 0.75 arcsec FWHM for the 3 GHz maps. The contour levels are equally spaced on a log-scale, where the lowest is set at 3σ and the highest at the maximum peak flux-density of the radio structure. The remainder of the FR objects can be found in the Appendix in Fig. C.5.

groups we refer to a set of galaxies with a common dark matter halo (George et al., 2011). The Gozaliasl et al. (2019) catalogue includes 247 groups at $0.08 \leq z < 1.53$ from Chandra/XMM-Newton data, with halo masses (M_{200}) of the order of $10^{12-14} M_{\odot}$ (see Gozaliasl et al., 2019). To cross-correlate with the FR and COM AGN objects in our sample we use a search radius (r_{200}) within the virial radius of each group and the redshift of each object with $\Delta z = \pm 0.007 \times (1 + z_{\text{group}})$ in order to match the photometric redshift accuracy of our data (Laigle et al., 2016). Up to $z < 1.53$ we find 24/86 FRs (12/48 FR IIs, 4/28 FR I/FR IIs, 8/33 FR Is) and 87/966 COM AGN associated with an X-ray group⁵.

⁵ We have not accounted for differences in field coverage between the X-ray groups and 3 GHz VLA-COSMOS. From the 130 FRs, 44 lie above redshift $z = 1.53$.

3. Analysis and results

Here we present the analysis and results on 130 FR-type radio sources from the 3 GHz VLA-COSMOS, which were visually classified (59 FRIIs, 32 FRI/FRIIs, 39 FRIs), and 1818 COM AGN. Most FR objects (119 out of 130) have a counterpart in the optical/infrared based on the Smolčić et al. (2017b) study on counterpart association of VLA-COSMOS detections. Likewise, the majority of the FR sources (119 out of 130; $\sim 91\%$) have available redshifts, $\sim 57\%$ (68 out of 119) of which are spectroscopic and $\sim 43\%$ (51 out of 119) photometric. The control sample of compact COM AGN includes 1818 objects, all of which have counterpart association and redshifts, with a spectroscopic completeness of $\sim 32\%$ (575 out of 1818). The redshift distribution of the FR and COM AGN objects in our sample is presented in Fig. 3-Top, ranging between $0.03 \leq z \leq 6$, and the $L - z$ plane in Fig. 3-Bottom. The redshift distribution for the FR-type objects peaks around $z \sim 1$, while for the COM AGN peaks at slightly higher redshift⁶ ($z \sim 1.5$). Similarly, the FR-type objects have on average radio luminosities at 3 GHz of $L_{3 \text{ GHz}} \sim 10^{23} \text{ W Hz}^{-1} \text{ sr}^{-1}$, while the COM AGN are on average fainter at $L_{3 \text{ GHz}} \sim 10^{22} \text{ W Hz}^{-1} \text{ sr}^{-1}$. At each redshift the $L_{3 \text{ GHz}}$ of FRs tend to be in the high $L_{3 \text{ GHz}}$ tail of the overall $L_{3 \text{ GHz}}$ distribution. Fig. 3-Bottom shows that we are probing FR-type objects with radio luminosities above $L_{3 \text{ GHz}} \sim 10^{21} \text{ W Hz}^{-1} \text{ sr}^{-1}$. Table 5 shows the median radio luminosity values for the different populations and their dispersion, indicating an overlap of distributions. These results show no clear dichotomy in radio luminosity at 3 GHz between FRIs and FRIIs, with median values and the 84 & 16 percentiles for FRIIs at $\log_{10}(L_{3 \text{ GHz}}/\text{W Hz}^{-1} \text{ sr}^{-1}) = 23.30_{22.26}^{24.14}$ and for FRIs at $\log_{10}(L_{3 \text{ GHz}}/\text{W Hz}^{-1} \text{ sr}^{-1}) = 22.59_{22.15}^{23.32}$.

To investigate whether the differences between FRI- and FRII-type radio AGN presented in the classic FR classification scheme (Fanaroff & Riley, 1974) are inherent to their host galaxy/SMBH properties, or acquired, i.e., due to a denser environment, we compare the radio structure to physical properties of the radio sources and the large-scale environment. We refer to radio luminosity, size and Eddington ratio as 'physical properties' and use host properties and kpc-/Mpc-scale surroundings as indicators of 'environment'. Average values from this analysis are given in Table 5.

3.1. Linear-projected sizes and radio luminosity

An important physical parameter for radio AGN is their linear-projected size. This is not a straightforward parameter to measure, as most radio AGN with extended sizes are far from straight. They rather exhibit bends in their radio structure making the measurement more complex. Additionally, jet-less AGN required a different approach, as described below. Thus, the radio sizes of the objects in our sample are measured with two different techniques. The FR-type objects were put through a semi-automatic machine learning code which measures the largest angular size (LAS) of the sources in arcsec. The code is described in detail in Appendix C, and provides accurate size estimates for $\sim 90\%$ of the FR sample. As a secondary check, we measured by hand the largest angular sizes, presented in Table C.1. As the

⁶ This difference in the mean redshift values between FRIIs or FRIs and COM AGN seems to be statistically significant. For example, a Z-test between FRI/FRII and COM AGN gives: z-score = -3.35 and p-value = 0.0008.

⁷ A steep radio spectral index of 0.8 is assumed in the calculation of radio luminosities at 3 GHz.

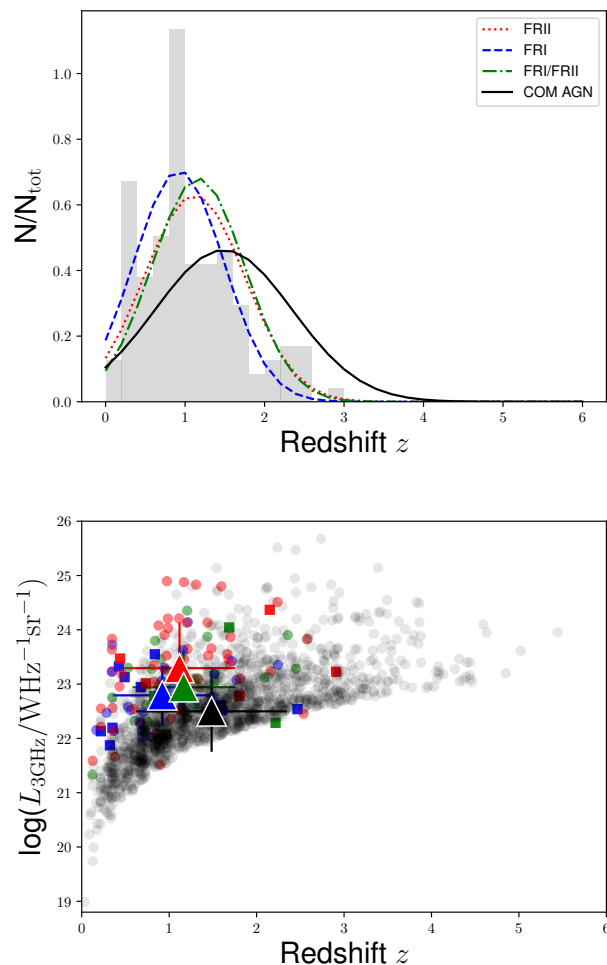


Fig. 3: **Top:** Redshift distribution of the FR-type sources in our sample shown in grey. The Gaussian distributions show Gaussian fits to the redshift distribution of different populations, colour-coded based on radio classification: FRIIs (red), FRIs (blue), FRI/FRII (green). We also show the COM AGN control sample as a black solid line. **Bottom:** Radio luminosity at 3 GHz versus redshift for the FRIIs (red), FRIs (blue), FRI/FRII (green) and COM AGN (black) in our sample. The large triangles give the corresponding mean values for each population and the standard deviation. Squares are objects without radio excess.

machine learning code does not provide robust size estimates for the full sample, we use the by-hand measurements in our analysis for consistency. A comparison of the estimated and measured by hand sizes is given in Appendix C and Fig. C.3. We then convert the LAS quantity to linear-projected size of the sources D in kpc (Table C.1), by taking into account the redshift of each object, resulting in sizes for 119 out of the 130 ($\sim 91\%$) FRs in our sample. The COM AGN had their sizes measured by a gaussian fit using the publicly available code `pyBDSF` (Mohan & Rafferty, 2015). The size for the COM AGN used in our analysis is the intrinsic size, after deconvolution from the synthesised beam (Jiménez-Andrade et al., 2019). Sizes for the COM AGN are given in the Appendix in Table C.4.

In Fig. 4 we present the $L - D$ diagram for the sources in our sample. FR objects have on average similar radio luminosities at 3 GHz independent of FR type, and they also have similar luminosities to COM AGN. Their linear-projected sizes, though, differ. FRs have sizes ranging from 10 kpc to 1 Mpc, forming

the FR cloud, while COM AGN are less than ~ 30 kpc at 3 GHz, forming the COM cloud in the $L - D$ diagram. Additionally, FRII-type objects are on average larger than FRI/FRII and FRI objects by a factor of ~ 2 and ~ 3 , respectively. Still, there is an overlap of the distributions and no clear dichotomy in FR type.

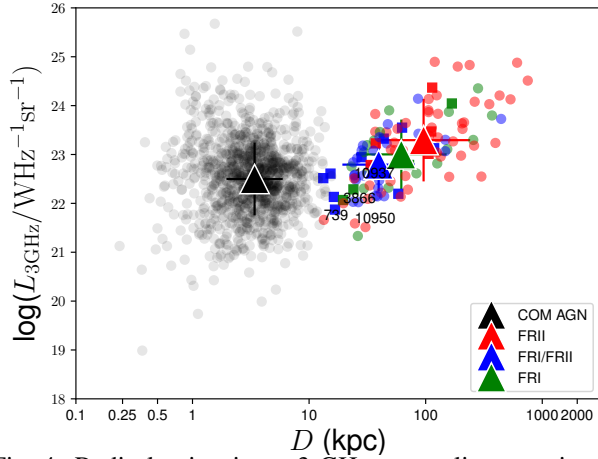


Fig. 4: Radio luminosity at 3 GHz versus linear-projected size D . Symbols: filled red circles denote FRII objects, filled blue circles denote FRI objects, filled green circles are FRI/FRII objects, and filled black circles denote compact AGN. FR objects without radio excess (see Sec. 2) are shown as squares instead of circles.

3.2. Eddington ratios

The Eddington ratio is a physical quantity directly related to how efficiently a black hole is accreting matter around it. It is the ratio of luminosity emitted by the source over the Eddington luminosity, i.e. the maximum luminosity an object can achieve when the gravitational pull and emitted radiation are balanced. The reason we explore this quantity is to investigate how many of the objects in our sample are efficient or inefficient accreters, and to search for trends with radio structure. For the purposes of our study we calculate the Eddington ratios using the X-ray catalogue of Marchesi et al. (2016). Cross-correlation with the Chandra COSMOS-Legacy Survey X-ray catalogue yields 19 FRIIs, 8 FRI/FRIIs, 6 FRIs, and 291 COM AGN with a secure X-ray detection.

The Eddington ratio was calculated in two ways:

1. $\lambda_r = L_{\text{rad}} / L_{\text{Edd}}$, i.e. the radiative luminosity over the Eddington luminosity. The intrinsic AGN X-ray luminosities L_{rad} were scaled to bolometric luminosities via a set of luminosity-dependent bolometric corrections by Lusso et al. (2012). The Eddington luminosity was calculated using the standard conversion $M_{\text{BH}}/M_{\text{bulge}} \sim 0.002$ (Marconi & Hunt, 2003).
2. $\lambda_{\text{rk}} = (L_{\text{rad}} + Q_{\text{jet}}) / L_{\text{Edd}}$, i.e. same as λ_r but with the addition of the jet kinetic energy to the numerator. The kinetic energy is calculated from the radio luminosity at 1.4 GHz using the empirical relation by Cavagnolo et al. (2010). The 1.4 GHz luminosity comes from 3 GHz fluxes, then converted to 1.4 GHz using a typical steep spectral index of 0.7 (if not detected at 1.4 GHz), or using the observed 1.4-3 GHz slope (if detected at 1.4 GHz).

In order to decide which scaling relation to use for the calculation of kinetic energy, or jet power Q_{jet} , we compare several

scaling relations between radio luminosity and jet power. This comparison is presented in Fig. 5. We over-plot the 3 GHz VLA-COSMOS data for different inclinations of the jet with respect to the observer. Objects with inclination of 0 deg (face-on) follow well the Cavagnolo et al. (2010) scaling relation, thus we take this as a conservative approach for the calculation of jet power. We should acknowledge that the radio jet power strongly depends on the viewing angle. When it comes to the kinetic Eddington ratio, it should be made clear that the kinetic component could be > 100 times smaller, producing zero change in the Eddington ratio. For larger inclinations (> 10 deg) none of the scaling relations shown represent the data.

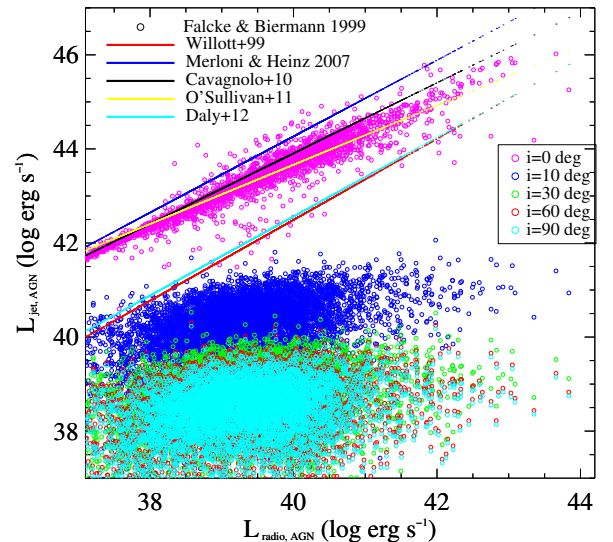


Fig. 5: Scaling relations between L_{jet} and radio luminosity at 1.4 GHz. The 3 GHz VLA-COSMOS data are plotted as coloured circles using the relations of Falcke & Biermann (1999) for different inclination angles of the jet, from 0 (face on - towards observer) to 90 (edge on) degrees. Lines show scaling relations from literature: red line for Willott et al. (1999), blue line for Merloni & Heinz (2007), black line for Cavagnolo et al. (2010), yellow line for O'Sullivan et al. (2011) and cyan line for Daly et al. (2012).

For non-X-ray detected objects, we use a stacking approach to estimate a median Eddington ratio. We used the publicly available X-ray stacking tool CSTACK⁸ developed by T. Miyaji. This tool provides stacked count-rates and fluxes, as well as reliable uncertainties estimated from a bootstrapping procedure. Each bootstrap yields a mean stacked L_X (rest-frame 2-10 keV). After bootstrapping 500 times, we took the median of the resulting distribution in order to alleviate the effect of possible outliers. From the median L_X , we subtracted the expected contribution arising from star formation⁹, given by the L_X -SFR relation derived by Symeonidis et al. (2014), and later on we considered only the remaining X-ray emission (if any), which is likely attributable to the AGN. The X-ray emission was then corrected for nuclear obscuration, based on the Hardness ratio (Xue et al., 2010), and by assuming an intrinsic power-law X-ray spectrum with a constant slope $\Gamma = 1.8$ (e.g. Tozzi et al., 2006).

In Fig. 6 we present the radiative Eddington ratio λ_r and in Fig. 7 we present the radiative plus kinetic Eddington ratio λ_{rk}

⁸ <http://lambic.astrosen.unam.mx/cstack/>

⁹ SFR is estimated from the fit to the infrared SED.

Table 1: Eddington ratios from radiative luminosity, not corrected for redshift dependence

| radio class | | N | $\text{Log}_{10}(\lambda_r)$ | | | $\text{Log}_{10}(L_X/L_{\text{radio}})$ | | |
|-------------|----------|------|------------------------------|-------|-------|---|------|------|
| | | | median | 16% | 84% | median | 16% | 84% |
| FRII | detected | 18 | -2.20 | -2.27 | -2.11 | 1.76 | 1.72 | 1.81 |
| | stacked | 30 | -3.43 | -3.55 | -3.30 | 1.00 | 0.87 | 1.13 |
| FRI | detected | 6 | -1.82 | -1.90 | -1.74 | 2.64 | 2.58 | 2.71 |
| | stacked | 25 | <-3.52 | – | – | <1.65 | – | – |
| FRI/FRII | detected | 8 | -2.43 | -2.52 | -2.26 | 1.88 | 1.83 | 1.92 |
| | stacked | 12 | -3.19 | -3.37 | -3.00 | 1.62 | 1.44 | 1.81 |
| COM AGN | detected | 291 | -1.96 | -1.99 | -1.94 | 3.47 | 3.45 | 3.49 |
| | stacked | 1386 | -3.22 | -3.35 | -3.08 | 2.35 | 2.21 | 2.49 |

Notes. Eddington ratios using radiative luminosity, $\lambda_r = L_{\text{rad}} / L_{\text{Edd}}$ (see Sec. 3.2). The 16th and 84th percentile values indicate uncertainties on the medians.

Table 2: Eddington ratios from radiative luminosity and Q_{jet} , not corrected for redshift dependence

| radio class | | N | $\text{Log}_{10}(\lambda_{\text{rk}})$ | | | $\text{Log}_{10}(L_X/L_{\text{radio}})$ | | |
|-------------|----------|------|--|-------|-------|---|------|------|
| | | | median | 16% | 84% | median | 16% | 84% |
| FRII | detected | 18 | -1.13 | -1.15 | -1.10 | 1.76 | 1.71 | 1.81 |
| | stacked | 30 | -1.65 | -1.65 | -1.64 | 1.00 | 0.87 | 1.13 |
| FRI | detected | 6 | -1.50 | -1.56 | -1.43 | 2.64 | 2.58 | 2.71 |
| | stacked | 25 | <-2.21 | – | – | <1.67 | – | – |
| FRI/FRII | detected | 8 | -1.32 | -1.40 | -1.28 | 1.88 | 1.83 | 1.93 |
| | stacked | 12 | -1.91 | -1.92 | -1.89 | 1.65 | 1.45 | 1.85 |
| COM AGN | detected | 291 | -1.79 | -1.82 | -1.77 | 3.47 | 3.45 | 3.49 |
| | stacked | 1386 | -2.35 | -2.37 | -2.33 | 2.35 | 2.22 | 2.49 |

Notes. Eddington ratios including radiative luminosity and kinetic energy Q_{jet} , $\lambda_{\text{rk}} = (L_{\text{rad}} + Q_{\text{jet}}) / L_{\text{Edd}}$ (see Sec. 3.2). The 16th and 84th percentile values indicate uncertainties on the medians.

for the FRs and COM AGN with respect to the ratio of X-ray to radio luminosity. It is obvious that the addition of jet power boosts the Eddington ratio of FR sources, but only slightly increases the Eddington ratio of COM AGN.

The L/L_{radio} is higher for COM AGN because the average L_{radio} is lower than for the other classes (Fig. 3), despite the mean redshift being even higher. We plot this luminosity ratio in respect to the Eddington ratio in order compare how fast BHs are accreting relative to their mass against the predominant type of AGN feedback, radiative versus mechanical given by the L/L_{radio} . In principle, we get information about which form (mainly radiative or mainly mechanical) the feedback of the AGN is predominantly exerted, as a function of BH accretion rate. Ideally, we should calculate the Eddington ratios from an independent tracer, not the X-rays. The latter is not possible as BH masses are available only for a small subset. The target of this analysis is to compare different populations to each other, i.e. the relative behaviour between FR classes and COM AGN, without over-interpreting the relation between L/L_{radio} and Eddington ratio itself.

The stacked Eddington ratios of FRs also show a boost in their values with the addition of kinetic energy. This time, also COM AGN show a boost in the stacked λ_{rk} values. This is different from the measured values and in particular for COM AGN. The stacks allow us to reveal the fainter X-ray population not probed by the flux-limited X-ray data, and lower the L_X/L_{rad} ratio. The Eddington ratio is no longer dominated by the brightest X-ray sources, thus the jet power has a stronger effect on the stacked Eddington ratio. Additionally, there seems to be a slight dichotomy in the stacked λ_{rk} values between FRIs and FRIIs, with FRIs having lower stacked Eddington ratios than FRIIs. Nevertheless, the FRI stacked values are upper limits. The boost given to the stacked λ_{rk} values is due to the radio luminosity, which is used to calculate the kinetic energy, and is dependent on redshift. Thus the slight difference in the values of FRI and

FRII objects can be attributed to the differences in radio luminosity between the populations, but also has a dependence on their redshift.

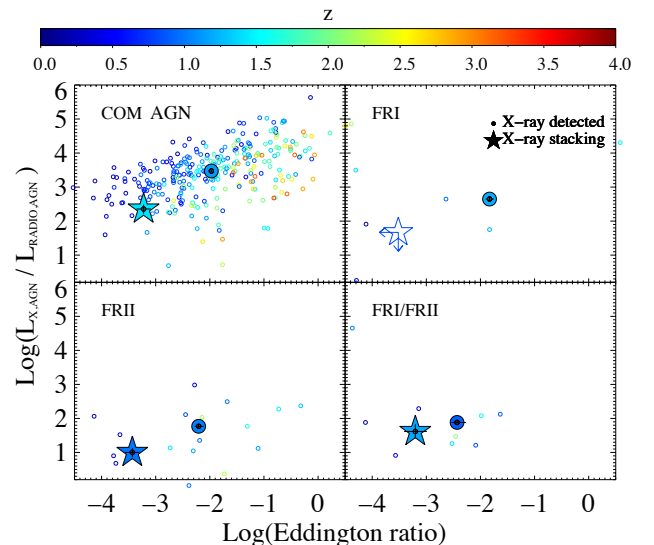


Fig. 6: The ratio of X-ray to radio luminosity at 1.4 GHz versus radiative Eddington ratios for the FR and COM AGN objects. Panels: **Top left** for COM AGN, **top right** for FRI, **bottom left** for FRII, **bottom right** for FRI/FRII. Colours represent redshifts. Small circles are individual X-ray detections. Large circles show median values. Stars are the stacked values as listed in Table 1. The standard deviation is also plotted on the median and stacked values. Upper limits are given at 90% level.

Since the purpose of this paper is to investigate the classic FR dichotomy, ideally the FR populations should be at the same redshift, which is not the case (see Fig. 3-Top). Additionally, the X-ray data used for the calculation of the Eddington ratios

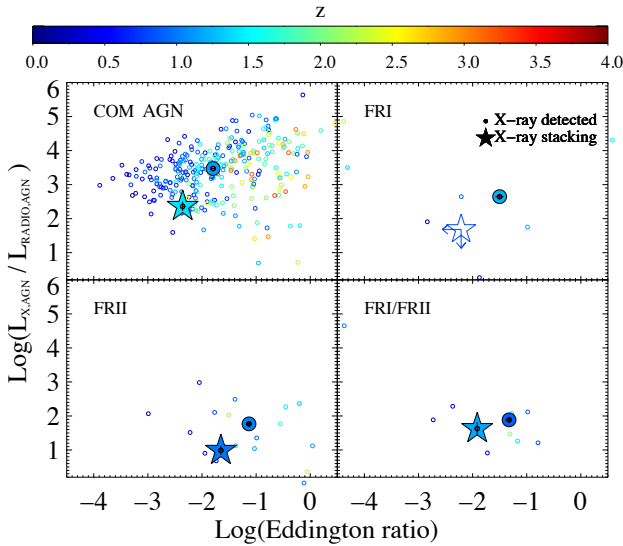


Fig. 7: The ratio of X-ray to radio luminosity at 1.4 GHz versus radiative plus kinetic Eddington ratios for the FR and COM AGN objects. Panels: **Top left** for COM AGN, **top right** for FRI, **bottom left** for FRII, **bottom right** for FRI/FRII. Colours represent redshifts. Small circles are individual X-ray detections. Large circles show median values. Stars are the stacked values as listed in Table 2. The standard deviation is also plotted on the median and stacked values. Upper limits are given at 90% level.

are flux limited, which could introduce a redshift dependence to the Eddington ratios. Another dependence to the Eddington ratio might be introduced by the stellar mass of the host used in the calculations. We investigate the relationship between Eddington ratio and redshift and find an increase of λ with higher redshift (see Fig. 8). We also investigate the relationship between M_* and redshift and find no dependence. We thus assume the relationship between L_X and redshift z is the main driver for the increase of the Eddington ratio with redshift. To account for this dependence on redshift we correct the Eddington ratios by dividing with D_L^2 . For the purpose of comparing the FR and COM AGN populations to each other we will use the D_L^2 corrected Eddington ratios throughout the paper, unless otherwise stated. We will use throughout λ^* for the D_L^2 corrected Eddington ratio and λ for the uncorrected. We caution the reader not to take the D_L^2 corrected Eddington ratios as absolute values, but rather as a means of comparison between the populations presented here. In Tables 1 & 2 we give the Eddington ratio values for the radiative and radiative plus kinetic calculations, respectively, before we applied the D_L^2 correction. The uncorrected Eddington ratios are being discussed in Sec. 4 where we compare them to literature results from past radio studies. The Eddington ratio values for individual objects are presented in Fig. C.3 in the Appendix. Finally, in Fig. 9 we plot the histogram of Eddington ratios of X-ray detected sources split into different radio classes.

In Fig. 10 we plot the radio luminosity at 3 GHz versus the Eddington ratio for corrected and uncorrected values. For the radiative case we see that FRIs, FRIIs and FRI/FRIIs have on average similar λ_r^* values and similar distribution of Eddington ratios. When we add the contribution from kinetic energy to the Eddington ratio, we find that the mean values of λ_{rk}^* increase for all FR objects, and due to the difference in radio luminosity, there is an offset between the distributions. Still, there is no statistically significant dichotomy found for the FR population when considering their Eddington ratios (with and without including the jet power).

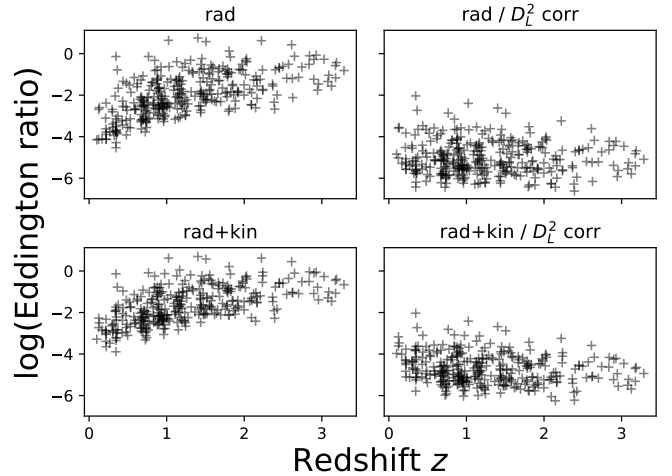


Fig. 8: **Left:** Redshift dependence of Eddington ratios λ calculated from the X-rays. **Right:** Eddington ratios corrected for redshift dependence by dividing with D_L^2 . **Top panels** show the radiative Eddington ratios, and **bottom** the radiative including kinetic energy contribution, as described in Sec. 3.2.

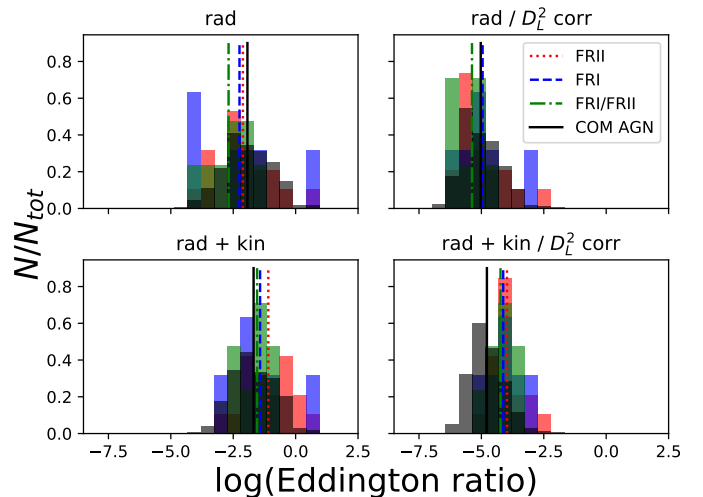


Fig. 9: Histogram of Eddington ratios of X-ray detected sources, colour-coded based on our classification scheme in FRII (red), FRI (blue), FRI/FRII (green) and COM AGN (black). **Top panels:** radiative Eddington ratio (**left**) and redshift-dependence corrected (**right**). **Bottom panels:** radiative and kinetic Eddington ratio (**left**) and redshift-dependence corrected (**right**). The median values of the Eddington ratio for each population are shown as lines: red dotted lines for FRIIs, blue dashed for FRIs, green dash-dotted for FRI/FRIIs and black solid lines for COM AGN.

For the COM AGN we note that the average λ_r^* and λ_{rk}^* values are similar and the kinetic energy does not contribute significantly to the Eddington ratio in this class of objects, since the radiative luminosity from the X-rays is the dominant contributor to the Eddington ratio. On average we see that the COM AGN are much brighter at X-rays than the FR-type objects (Figs 6 & 7), but there is a large spread in the L_X/L_{rad} ratio. Their λ_r^* Eddington ratios are on average similar to the FR objects within the error. The difference between FRs and COM AGN lies in the

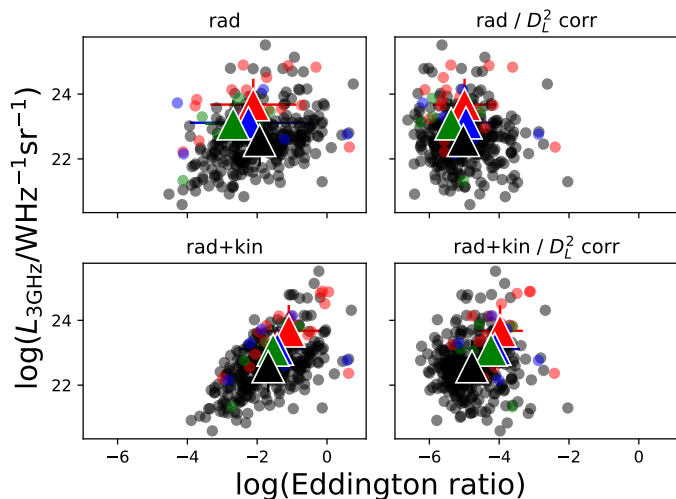


Fig. 10: Radio power at 3 GHz versus Eddington ratio, radiative (**top panels**) and kinetic (**bottom panels**), for D_L^2 uncorrected (**left panels**) and corrected values (**right panels**). FRII (red), FRI (blue), FRI/FRII (green) and COM AGN (black). Mean values and standard deviations shown in large triangles, colour-coded based on the radio class.

inclusion of jet power, with FRs getting a boost due to their jet power.

3.3. Environmental probes

To address the large-scale environment of the objects in our sample we use several environmental probes, from kpc to Mpc scales. Below we describe in detail the analysis and results on relating the hosts (Sec. 3.3.1), X-ray groups (Sec. 3.3.2), and large-scale environment (Sec. 3.3.3) to the radio structure of the FRs and COM AGN in our sample.

3.3.1. Host galaxies

In order to study what types of hosts the FRs and COM AGN of our sample inhabit, we plot the $\Delta\text{sSFR}-M_*$ diagram in Fig. 11–Left. This gives the difference between specific SFR (sSFR) of each object (SFR/M_*) to the specific SFR it would have at the main sequence (MS) for star-forming galaxies given its redshift (sSFR_{MS}), versus the stellar mass; or the "main-sequence offset $\Delta(\text{MS})$ ". We also plot the main sequence for star forming galaxies (see Whitaker et al., 2012) as a solid black line. More recent MS prescriptions include a bending at high M_* (e.g. Speagle et al., 2014; Schreiber et al., 2015; Lee et al., 2015; Scoville et al., 2017; Leslie et al., 2020), which would place the sources in our sample a bit closer to the MS, though still systematically below. At $z > 1$ we would have a negligible fraction of fully quiescent hosts (Davidzon et al., 2017), since the M_* function drops exponentially.

From Fig. 11–Left we see that the majority of FR objects lie below the MS in the green valley and the red-and-dead region of the diagram. In Table C.2 we also present the optical morphology of these hosts from Schinnerer et al. (2010). We see that not all of FR objects in our sample reside in elliptical hosts. When accounting for the optical classification, we find 3 elliptical hosts within the MS for SFGs while at the same time we have 20 disk galaxies below the MS. Furthermore, we have marked objects with their names for five cases which do not follow the general trend of the FR population. Objects 195, 773, 10940, 10947,

10963 have hosts in the starburst (SB) region of the $\Delta\text{sSFR}-M_*$ diagram, above the MS for SFGs. Additionally, 10943 is also an outlier in the low-mass end ($< 10^{10.5} M_\odot$) of the diagram. We visually inspect these outliers to avoid misidentifications. These objects have small and unusual shapes, but they either exhibit radio excess (195, 773, 10940, 10943, 10947; Table C.1) and/or are classified as AGN based on their SED fit (773, 10940; see Table C.2). Object 10963 does not exhibit radio excess nor an AGN SED, so we caution the reader. We conclude that outliers of the sort can exist in samples of radio AGN and may represent an early evolutionary stage, co-existence of starburst and AGN, or a starburst on its way to quenching.

Fig. 11 thus indicates that there is no observed dichotomy in the host properties of FR galaxies, rather we assure a mix of distributions. What we see in Fig. 11 is that the general trend of the FR populations suggests objects moving from the MS to the quiescent region through the green valley. The majority of the COM AGN population is following the FR population trend in the $\Delta\text{sSFR}-M_*$ diagram but with higher fraction of sources at the SB and low stellar mass regions ($< 10^{10.5} M_\odot$). In Table 3 we present median properties for ΔsSFR and M_* for FRs and COMS AGN, as well as the results of a linear regression model fitted to the data. We find an anti-correlation between ΔsSFR and M_* for both FRs and COM AGN, indicating quenching of star formation.

Given the fact that FR objects display jets, we need to investigate the possibility we are witnessing radio-mode feedback from AGN in their hosts. For that purpose we plot the $\Delta\text{sSFR}-\text{SFH}$ diagram shown in Fig. 11–Right. We use the last burst of star formation to investigate when was the last star-forming episode in each host. This quantity was estimated from the fit to the SED, as SFR and M_* were (Delvecchio et al., 2017). We find FR objects with more recent bursts of SF to still occupy the MS, while objects with later $t_{\text{last burst}}$ to be located below the MS for SFGs. This tells us that less star-forming galaxies have longer $t_{\text{last burst}}$, which is also seen in the COM AGN sample. We note that this anti-correlation is expected from the co-dependence between sSFR and $t_{\text{last burst}}$ in the SED-fitting code. Outliers with recent bursts below the MS do exist (e.g. 404 and 10943). We deduct from these plots that FR objects have quenched hosts as they systematically lie below the MS. We discuss this further in Sec. 4.

3.3.2. Galaxy group environment: X-ray groups

To probe if our galaxies preferentially lie within galaxy groups, we cross-correlate their positions with the X-ray group catalogue of Gozaliasl et al. (2019). Our goal is to investigate whether FR-type radio sources prefer an environment type over another. For example, do they tend to reside within group environment or in the field. For that purpose we compare objects which lie within the X-ray groups in COSMOS (Gozaliasl et al., 2019) to the ones which lie outside X-ray groups. This is shown in Fig. 12 where we present histograms for the FR and COM AGN objects within X-ray groups and in the field, for redshift $0.08 \leq z < 1.53$. Given that we have more objects outside the X-ray groups than inside in this redshift range, we select randomly an equal number of objects for the ones outside as those inside the X-ray groups, to have an unbiased comparison. We randomly draw objects from the "outside a group" sub-sample from the 4 classes presented and compare the histograms in Fig. 12. Our results show that there is no preference on being inside X-ray groups or in the field for the radio AGN presented here. These results seem to be in contrast to the study of Smolčić et al. (2011), who find that ra-

Table 3: Median and fitted values for $\Delta\text{sSFR}-M_*/\text{SFH}$ diagrams

| | N | $\langle \Delta\text{sSFR} \rangle$ | $\langle M_* \rangle$ | linear regression (intercept, slope) | N | $\langle \Delta\text{sSFR} \rangle$ | $\langle t_{\text{last burst}} \rangle$ |
|---------|------|-------------------------------------|-----------------------|---|------|-------------------------------------|---|
| FR | 105 | -0.58 (0.516) | 11.17 (0.440) | 1.46, -0.18 | 100 | -0.57 (0.437) | 9.25 (0.410) |
| COM AGN | 1800 | -0.60 (0.488) | 10.90 (0.558) | 0.27, -0.07 | 1738 | -0.61 (0.481) | 9.24 (0.420) |

Notes. Median values derived for the FRs and COM AGN from Fig. 11. Values in parenthesis are standard deviations. SFR, M_* and $t_{\text{last burst}}$ are estimated from the fit to the infrared SED (Delvecchio et al., 2017). Note: We do not provide the results of the linear regression between ΔsSFR and $t_{\text{last burst}}$ as the observed anti-correlation is artificially induced by the co-dependence between these quantities in the SED-fitting code.

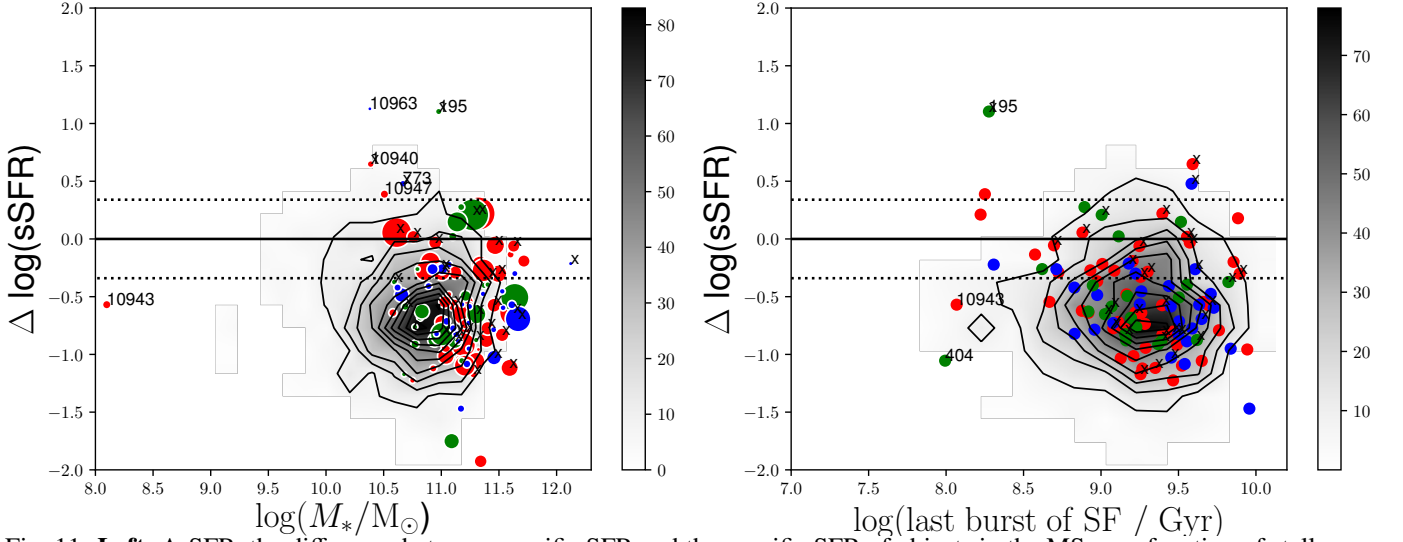


Fig. 11: **Left:** ΔsSFR , the difference between specific SFR and the specific SFR of objects in the MS, as a function of stellar mass for the four populations of radio AGN presented in this paper. For FR objects, symbols are scaled based on their linear-projected size, with larger symbols corresponding to larger objects. The jet-less COM AGN are shown in black as density plot. The solid and dotted lines show the main sequence for star forming galaxies and spread, based on Whitaker et al. (2012). **Right:** ΔsSFR , as on the left, versus the star-formation history (SFH) of each object. SFHs are estimated from a fit to the SED as described in Sec. 2.2. Median values are shown in Table 3. In both plots an 'x' marks objects that have an X-ray detection based on the catalogue of Marchesi et al. (2016).

radio AGN from 1.4 GHz VLA-COSMOS preferentially lie within group environments. There is also no strong trend regarding the different FR types. We find slightly more FRIIs within X-ray groups than FRIs, while hybrids are much less. These values are similar to the numbers of objects expected outside X-ray groups.

The objects lying outside X-ray groups could also belong to a group which has not been identified by X-ray observations as yet. Higher resolution and sensitivity X-ray observations could reveal more low-mass groups not currently included in the Gozaliasl et al. (2019) catalogue. In Vardoulaki et al. (2019) we show that by using the radio structure of jetted AGN as a probe, and how disturbed it is (i.e. bending caused by interaction with the large-scale environment) we can identify locations of possible X-ray groups which have not been identified by Gozaliasl et al. (2019) X-ray observations of COSMOS.

Additionally, we investigate whether FR-type objects have a preferred location in the X-ray groups they reside within and how does their location compare to jet-less AGN objects. This is shown in Fig. 13, where we give the distance r of the radio source from the group centre normalised to the virial radius r_{200} of the X-ray group for redshifts $0.08 \leq z < 1.53$. We compare the r/r_{200} ratio to the radio luminosity at 3 GHz and the linear-projected size D . We see that FR-type objects, independent of their type (FRII, FRI/FRII, FRI), can be found on any position within the virial radius of the X-ray group. This is also seen in COM AGN.

To investigate the preference in location within the X-ray groups for the FR and COM AGN populations we firstly estimate the average number density of objects within the X-ray groups. For FRs this number is $\langle N_X \rangle = 1.55 \pm 0.97$, for COM AGN $\langle N_X \rangle = 2.06 \pm 1.24$, and for the whole X-ray group sample $\langle N_X \rangle = 2.51 \pm 1.37$; the difference between the populations is not statistically significant. We then estimate their average distances from the X-ray group centres. FRs peak at $r/r_{200} = 0.26 \pm 0.21$ and COM AGN at $r/r_{200} = 0.31 \pm 0.26$. These results indicate that FRs and COM AGN, on average, reside close to the X-ray group centre. The latter is in line with the findings of Smolčić et al. (2011) utilising the 1.4 GHz VLA-COSMOS data.

About half of the radio AGN in our sample reside in brightest group galaxies (BGG), the most massive galaxy of the group. In particular $\sim 51\%$ (44 out of the 87) COM AGN and $\sim 46\%$ (11 out of 24) of FRs within X-ray groups are associated with a BGG. It has been shown by Gozaliasl et al. (2019) that BGGs are not always found in the centre of the X-ray group, suggesting the systems are not yet relaxed (Gozaliasl et al., 2020). The location of FRs within X-ray groups seems to be independent of physical properties such as radio luminosity and linear-projected size of the source. Similarly for COM AGN, with the exception of a trend found between radio luminosity of COM AGN

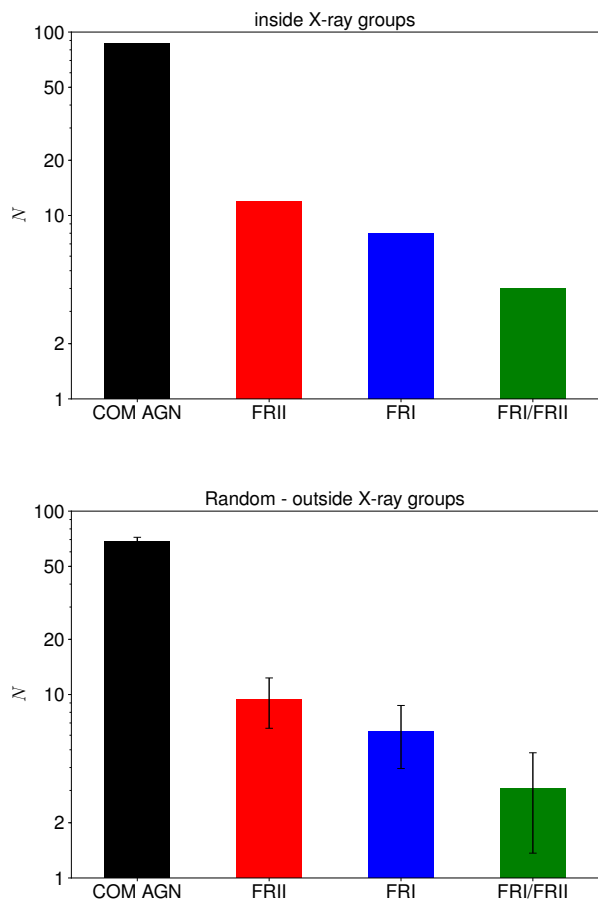


Fig. 12: Bar histogram of objects inside (**top**) and outside (**bottom**) the COSMOS X-ray groups from [Gozaliasl et al. \(2019\)](#), for $0.08 \leq z < 1.53$. The objects outside X-ray groups are selected via running a random number generator 1000 times with the same number of objects as the ones inside groups, and taking the mean and standard deviation. Colours: red for FRIIs, blue for FRIs, green for FRI/FRIIs and black for COM AGN. The number of objects inside X-ray groups: 87 COM AGN, 12 FRII, 4 FRI/FRII and 8 FRI. Outside the X-ray groups numbers are: 68 ± 3.9 COM AGN, 9 ± 2.9 FRII, 3 ± 1.7 FRI/FRII and 6 ± 2.3 FRI.

and distance from the X-ray group centre¹⁰, suggesting lower radio luminosities with increasing distance from the group centre. Otherwise, the brightest COM AGN tend to be closer to the X-ray group centre. Lastly, we also investigate the relation between redshift and r/r_{200} , with larger symbols being objects further away, but no trend becomes evident.

Finally, we investigate the hosts of FR and COM AGN within X-ray groups, plotting $\Delta sSFR$ and M_* versus the X-ray temperature of the group (Fig. 14). We see that objects below the MS lie mainly in X-ray groups with temperatures between 0.5 and 2 keV, with some exceptions of COM AGN at higher temperature. These FR objects lie in massive hosts, while there is a slight trend for quenched massive hosts at lower redshifts to be found in cooler X-ray groups than those at higher redshifts. Furthermore, the hosts with the oldest episode of SF are the ones

¹⁰ We calculate the Pearson correlation coefficient between $L_{3 \text{ GHz}}$ and r/r_{200} in COM AGN and find an anti-correlation (slope = -0.19, P = 0.070).

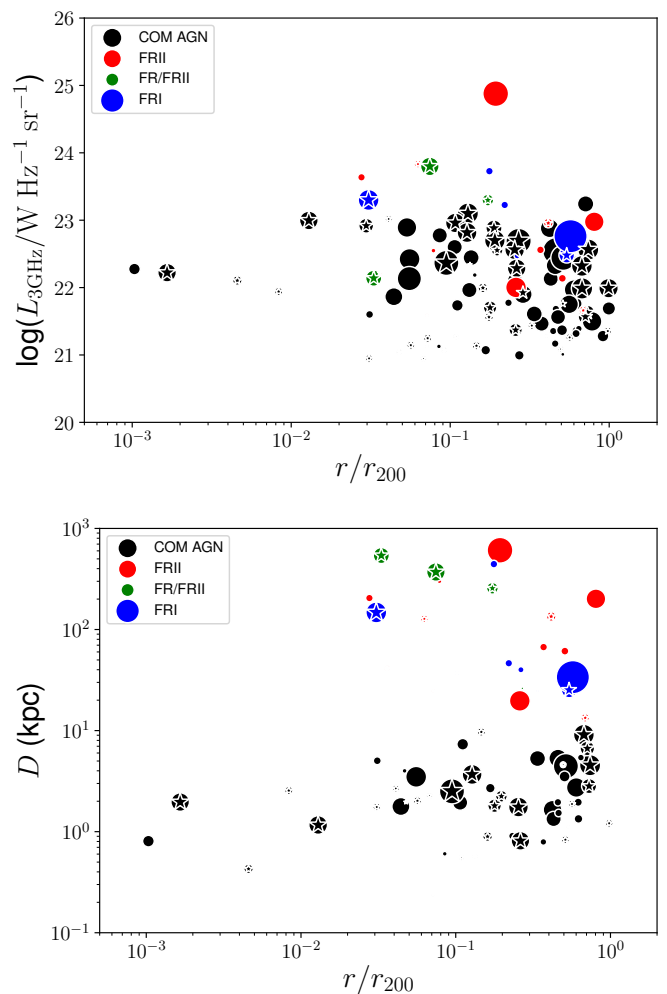


Fig. 13: **Top**: Radio luminosity at 3 GHz for the galaxies which lie within the X-ray groups in the COSMOS field ([Gozaliasl et al., 2019](#)) versus their distance from the group centre, normalised by the virial radius r_{200} , for $0.08 \leq z < 1.53$. **Bottom**: linear-projected size D as in Table C.1 versus distance from the group centre normalised to the virial radius, for the same redshift bins as on the figure above. Colours: red for FRIIs, blue for FRIs, green for FRI/FRIIs and black for COM AGN. In both plots symbol size is proportional to redshift (larger the symbol, larger the redshift). Stars highlight sources which are the brightest group galaxy.

in cooler X-ray groups, with some exceptions of COM AGN and FRIs. We also see that both FRs and COM AGN lie in similar IGM temperature X-ray groups on average, with median temperatures of 1.16 ± 0.46 keV and 1.04 ± 0.59 keV for FRs and COM AGN, respectively. There is no observed dichotomy in FRs regarding their X-ray group temperature. Finally, the location of the AGN within the X-ray group is not linked to the group temperature. ([Dubois et al., 2011](#)) show that the interaction between AGN energy released from jets and the ICM gas can result in the creation of cool-core clusters, assuming no metals are taken into account. Thus our results, showing a trend between quenched massive hosts and cooler X-ray groups could support a scenario where AGN radio-mode feedback is in play.

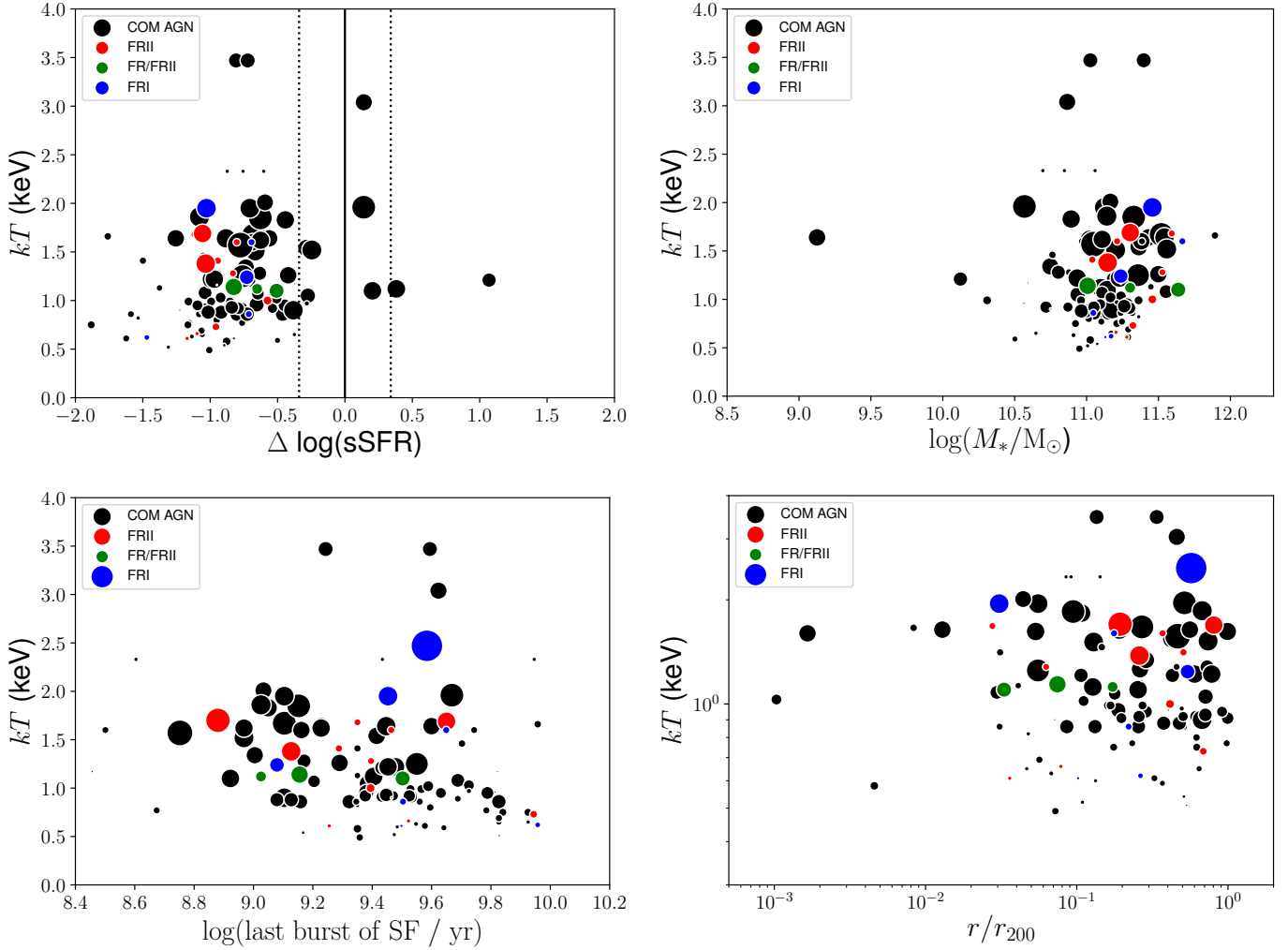


Fig. 14: **Top Left:** IGM temperature kT of the X-ray group in keV versus $\Delta \log(\text{sSFR})$ for the FRs and COM AGN which lie within the X-ray groups ($0.08 \leq z < 1.53$) in the COSMOS field (Gozali *et al.*, 2019). The solid and dotted lines show the main sequence for star forming galaxies and spread, based on Whitaker *et al.* (2012). **Top Right:** IGM temperature kT of the X-ray group in keV versus M_* of the FRs and COM AGN which lie within the X-ray groups. Colours: red for FRIIs, blue for FRIs, green for FRI/FRIIs and black for COM AGN. **Bottom Left:** IGM temperature in keV versus last burst of star formation. **Bottom Right:** IGM temperature in keV versus distance of FR or COM AGN from X-ray group centre, normalised to the virial radius r_{200} . In all plots symbol size is proportional to redshift (symbol size increases with redshift). Symbols: red for FRII, green for FRI/FRII, blue for FRI and black for COM AGN. The median IGM temperature corresponding to FRs and COM AGN is 1.16 ± 0.46 and 1.04 ± 0.59 , respectively.

3.3.3. Mpc-scale environments

To study the Mpc-scale environment we use 1) the density fields from Scoville *et al.* (2013) and 2) the large-scale environments from Darvish *et al.* (2015) and Darvish *et al.* (2017), and we compare to the radio structure of the FR and COM AGN objects in our sample. The density fields from Scoville *et al.* (2013) are given in redshift slices¹¹ up to redshift of 3, thus any object in our sample above this redshift is excluded from the analysis. The total surface densities of galaxies per comoving Mpc^2 , which were created using two techniques, adaptive smoothing and Voronoi tessellation, as described in Scoville *et al.* (2013). The large-scale-structure mapping made use of the K -band selected objects catalogue and photometric redshifts for COSMOS from the Ultra-VISTA survey, in addition to other COSMOS photometry (see Ilbert *et al.*, 2013). Darvish *et al.* (2015) and Darvish *et al.*

(2017) expand the study of Scoville *et al.* (2013) to include specific types of environment, such as cluster, filaments and the field, and also provide information on whether the galaxy is a central galaxy, a satellite, or isolated.

In Fig. 15 we present the density per Mpc^2 for the objects in our sample after cross-correlating with the density fields from Scoville *et al.* (2013). There is a large scatter in the environments that COM AGN inhabit, also seen for the FR-type objects. On average FRIs, FRIIs, FRI/FRIIs and COM AGN occupy similar density environments, as can be seen by their distributions. This suggests there is no preference in the environment between FR-type objects and no dichotomy in FR sources, which we will further discuss in Sec. 4. Similar results are obtained if we use the over-densities from Scoville *et al.* (2013) instead of the number density/ Mpc^2 of galaxies in the field.

As a probe of the cosmic web we use the study of Darvish *et al.* (2017) who separate the large-scale environment, the density fields in COSMOS in Cluster, Filament or Field using a Hessian

¹¹ Data are publicly available through this link: <http://irsa.ipac.caltech.edu/data/COSMOS/ancillary/densities/>

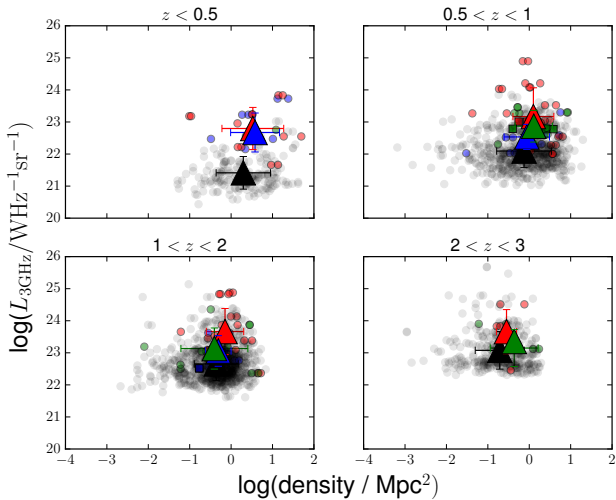


Fig. 15: Radio luminosity at 3 GHz versus number density per Mpc^2 of galaxies in COSMOS, in four redshift bins. The density fields are from Scoville et al. (2013). Symbols as in Fig. 4. Circles are objects with radio excess; squares are object without radio excess (Delvecchio et al., 2017). The mean values are given by large triangles, along with their standard deviations for the FRIIs (red), FRI/FRIIs (green) and COM AGN (black). The bins are selected so we can compare to literature.

matrix. They further add a classification based on whether the galaxy is the most massive of a group (Central), is within a group but not the most massive galaxy (Satellite) and is not associated with a group (Isolated) by applying a friends-of-friends algorithm. We cross-correlate their catalogue (Darvish et al., 2017) with the FR and COM AGN samples. The results are presented in Table 4 and Fig. 16. The match was done within a $30''$ radius and in a $\Delta z = 0.1$ redshift slice. We find 35 FRIIs, 15 FRI/FRIIs, 22 FRI and 362 COM AGN.

We note that all FRs which cross-matched with the Darvish et al. (2017) environmental probes lie below the spread of the MS for SFGs. The biggest difference visible is within a cluster environment, for FR objects that lie in satellite galaxies. FRII associated with satellite hosts are located closer to the MS for SFGs than FRIIs and FRI/FRIIs, which are embedded in the quiescent region, providing the only clear division in the current study between FR-type objects. The COM AGN show similar ΔsSFR with FRIIs which are associated with satellites inside clusters.

We further investigate whether there are any links between FRs, the Darvish et al. (2017) environments, and the last burst of star formation. The purpose is to trace the effects of kinetic feedback from FRs in different environments. In Fig. 17 we plot the FR objects, cross-correlated to these different environments versus the last burst of star formation in their host. In combination with Fig. 16, we see that satellite hosts of FR objects within clusters have similar $t_{\text{last burst}}$ but very different ΔsSFR values. The latter suggests differences in the quenching of SF, with FRII and FRI/FRII quenching their hosts more efficiently than FRI and COM AGN. Since FRIIs and FRI/FRIIs are on average radio brighter than FRI, this is an indication that radio-mode feedback from FRII and FRI/FRIIs which lie in satellite galaxies within clusters is the cause of star-formation quenching in their hosts. We note the result suffers from small number statistics, with 6 FRIIs, 2 FRI/FRIIs and 2 FRI in satellites within clusters.

Table 4: FRs and COM AGN within different environments

| Radio class | cluster | filament | field |
|-------------|---------|----------|-------|
| FRII | 8 | 17 | 10 |
| FRI/FRII | 6 | 5 | 4 |
| FRI | 3 | 11 | 8 |
| COM AGN | 84 | 132 | 146 |

Notes. Cross-correlation of the FR and COM AGN samples with Darvish et al. (2015) in respect to different environments (cluster, filament, field).

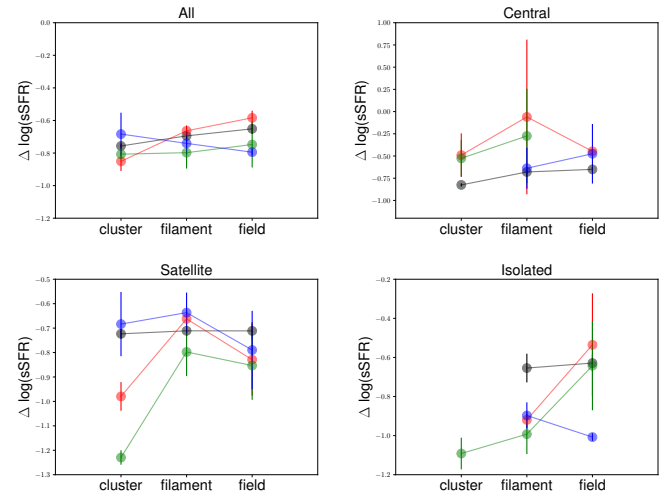


Fig. 16: ΔsSFR , the difference between specific SFR and the specific SFR of objects in the MS, for FRIIs (red), FRI/FRIIs (green), FRI (blue) and COM AGN (black) in respect to environment (cluster, filament, field) depending on galaxy type, in respect to environment as defined in Darvish et al. (2015).

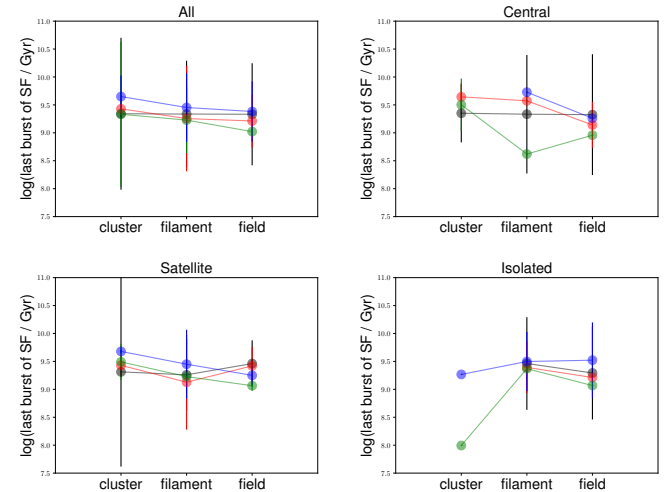


Fig. 17: Last burst of star formation for FRIIs (red), FRI/FRIIs (green), FRI (blue) and COM AGN (black) in respect to environment (cluster, filament, field) depending on galaxy type, as defined in Darvish et al. (2015).

4. Discussion: Relating FR structure to physical properties and the large-scale environment

In the previous sections we have presented an analysis on the properties of radio AGN from the 3 GHz VLA-COSMOS sample and related them to radio structure. In Table 5 we give the median derived properties, as well as the 16th and 84th percentiles, for the radio luminosity at 3 GHz, redshift, Eddington ratio (radiative and kinetic), and number density of

galaxies per Mpc². Below we discuss our results and compare them to literature, and to the semi-empirical simulation S³-SEX (Wilman et al., 2008), in order to understand what affects the FR structure and what physical mechanisms drive the traditional FR dichotomy.

4.1. Radio luminosity and size

In our study of 3 GHz VLA-COSMOS radio AGN we find that FRIIs are on average larger in size than FRIs and FRI/FRII by ~ 69% and ~ 56%, respectively, while there is an overlap in the distributions as mentioned earlier. This is expected according to the classic FR scheme wherein FRIIs are larger and brighter than FRIs (e.g. Ledlow & Owen, 1996). Still recent studies, which address the FR dichotomy do not find a clear-cut difference in size between FRIs and FRIIs (e.g. Mingo et al., 2019). Several models of jet expansion approach the issue of how far an FR-type jet advances given a set of conditions (e.g. Turner & Shabala, 2015, and references within). Recently, Shen et al. (2020) have shown that the radio power is the responsible driver for how extended the radio jet is. Still there is no clear picture on what affects the FR radio structure and when we should expect for an FRI- or and FRII-type source to form.

The COM AGN at 3 GHz VLA-COSMOS have the smallest sizes, lacking jets or their jets are not detectable. This is related to the resolution and sensitivity capabilities our survey of 0".75 and 2.3 μ Jy/beam, respectively. With the 3 GHz VLA-COSMOS we find FRI sources as small as 8 kpc (object 3065) and possible FRII sources of 13 kpc up to redshifts of ~ 0.4 (object 739), or confirmed FRII sources of ~ 24 kpc (object 10937 at $z = 1.128$).

When studying samples of radio AGN selected from radio surveys one should take into account the biases introduced by the survey capabilities in detecting these objects. As we mentioned, our ability to detect FR-type radio AGN in surveys is limited by their surface brightness and redshift. We are only able to detect the brightest sources and youngest with increasing redshift, also known as redshift-youth degeneracy (Blundell & Rawlings, 1999). Another possibility on why it is hard to detect high-redshift radio AGN can be related to their radio lobes being quenched by the cosmic-microwave-background radiation (CMB) (Ghisellini et al., 2015). These authors claim that the parent population of high-redshift blazars, being extended radio AGN, cannot be detected in current surveys due to the interaction of their lobes with the CMB, quenching radio emission. These studies indicate that any trends with redshift are biased by our observing capabilities. Furthermore, the frequency of observation, although important in determining the actual size of the sources, is not so important for FRII sources that have bright hot-spots with an intermediate spectral index (~ 0.5). On the contrary, it is very important for FRI which have diffuse steep spectrum emission at their edges. This may explain the differences with samples of sources selected at low frequency, such as Mingo et al. (2019).

When it comes to their radio power, FRs cover a wide range of values at 3 GHz of 10^{21-26} W Hz sr⁻¹, while COM AGN go to fainter values reaching radio powers of 10^{19} W Hz sr⁻¹. This could be a surface brightness effect, as we discussed earlier, meaning we can only detect the lower-luminosity radio emission if it is concentrated; if it is extended, its surface brightness might be too low. Furthermore, there is a large overlap in the distributions of FR regarding their radio luminosity. The traditional FR scheme (e.g. Gopal-Krishna & Witta, 2001) in the local Universe ($z < 0.1$) describes as FRIIs being brighter than FRIs with

a clear dichotomy in radio power. Our results do not show a clear dichotomy. Vardoulaki et al. (2010) have verified the FR dichotomy at redshifts $z_{\text{med}} \sim 1.25$ for an area of ~ 5 deg² with depth 100mJy at 151 MHz, but with a small sample of 47 objects probing the FRI/FRII break at $L_{151\text{MHz}} \sim 10^{25}$ W Hz⁻¹ sr⁻¹; this translates to $L_{3\text{GHz}} \sim 10^{24}$ W Hz⁻¹ sr⁻¹ for $\alpha = 0.8$, which is the high end of the radio powers we are probing at 3 GHz VLA-COSMOS (see Figs 3 & 4). This suggests that the traditional FR dichotomy is based on populations which are much brighter and disappears when we probe much fainter populations of radio sources. Still, slight differences in radio power between FR classes remain, and further support the scenario where the difference could be due to accretion rate. We discuss this below.

4.2. Accretion indicators - Eddington ratios

From Table 5 we see that there is no clear dichotomy between FRIs and FRIIs and that the median values of Eddington ratios show a trend: FRIIs, which are slightly more radio bright on average, have lower λ_r values than FRIs, while FRI/FRIIs are the lowest. This trend is linked to how X-ray bright these sources are on average, since the X-ray flux is used to calculate their radiative Eddington ratio. The median values suggest that FRIIs accrete matter onto their SMBHs less efficiently than FRIs, but the difference is not statistically significant. With the addition of the kinetic energy on the Eddington ratio this picture changes. FRIIs and FRI/FRIIs get a boost (factor of 12 and 15, respectively) much more pronounced than FRIs (factor of 2). This boost can be explained by FRIIs and FRI/FRIIs being brighter than FRIs. The average radio luminosities of FRIIs and FRI/FRIIs are not significantly different from those of FRIs, but there is a wide distribution of radio luminosities which would explain the boost in the kinetic Eddington ratio (Fig. 3). COM AGN get only a slight boost at λ_{rk} (factor of 1.6), having the lowest Eddington ratios on average amongst the radio AGN in our sample.

Lusso et al. (2012) have calculated Eddington ratios from the X-rays for the COSMOS Type 1 and Type 2 AGN, and find that these populations are sub-Eddington, but still lower values than what is expected for highly accreting black holes. Our study verifies that the radio AGN population in COSMOS at 3 GHz is sub-Eddington. Lusso et al. (2012) further show that the average Eddington ratio increases with redshift for all types of AGN and black hole masses. In our sample we suffer from small number statistics in FRs and we do not see an increasing trend with redshift. We only find a mild increase with redshift, more evident in the COM AGN sample as seen in Figs 6 & 7.

For objects not detected at X-rays, we use stacking to obtain median values of their Eddington ratios. These objects, although not detected at X-rays, are radio bright but have on-average very low Eddington ratios, of the order of 10^{-4} . We investigate whether the Eddington ratios we are probing with X-ray using the bolometric corrections of Lusso et al. (2012) make physical sense. For Eddington ratio of the order of 0.0001 assuming $L_X = 10^{42}$ (41) erg s⁻¹ for $z \sim 1$ (i.e. below the detection limit at X-rays 2-10 keV Marchesi et al., 2016, see their Fig. 7), bolometric correction of 2.2 and $L_{\text{Edd}} = 10^{39.1}$ ($M_{\text{BH}}/10^8 M_{\odot}$) W (e.g. Vardoulaki et al., 2008), one would expect to have $M_{\text{BH}} \sim 10^{10}$ (9) M_{\odot} . This is not surprising for radio-loud AGN jet-mode population which are radiatively inefficient, and where an advection dominated accretion flow (ADAF) is present. One would expect very high mass SMBHs to be associated with these objects (see Fig. 4 in Heckman & Best, 2014).

Based on literature, FRIIs typically fall in the high-excitation class, with efficient accretion onto their SMBHs, and FRIs ex-

Vardoulaki et al.: FR-type radio sources at 3 GHz VLA-COSMOS
 Table 5: Median derived properties of the FR & COM AGN objects

| radio class | N total | N with z | $\text{Log}(L_{3\text{GHz}} / \text{WHz}^{-1}\text{sr}^{-1})$ | median _{16%} z | median _{84%} D (kpc) | λ_r | λ_{rk} | density/Mpc ² |
|-------------|---------|------------|---|--------------------------------------|--|---|---|--------------------------------------|
| FRII | 59 | 56 | 23.30 ^{24.14} _{22.26} | 0.97 ^{1.69} _{0.42} | 106.6 ^{238.2} _{36.9} | 0.006 ^{0.007} _{0.005} | 0.074 ^{0.078} _{0.069} | 0.90 ^{3.73} _{0.05} |
| FRI/FRII | 32 | 27 | 22.81 ^{23.51} _{22.35} | 0.96 ^{1.65} _{0.73} | 47.8 ^{255.8} _{23.9} | 0.003 ^{0.005} _{0.002} | 0.046 ^{0.052} _{0.039} | 0.95 ^{3.49} _{0.39} |
| FRI | 39 | 36 | 22.59 ^{23.32} _{22.15} | 0.80 ^{1.54} _{0.35} | 33.7 ^{73.9} _{23.8} | 0.015 ^{0.017} _{0.012} | 0.031 ^{0.078} _{0.027} | 0.59 ^{2.25} _{0.27} |
| COM AGN | 1818 | 1818 | 22.46 ^{23.03} _{21.79} | 1.34 ^{2.31} _{0.68} | 1.74 ⁷ _{1.5} | 0.010 ^{0.011} _{0.010} | 0.016 ^{0.016} _{0.015} | 0.72 ^{1.88} _{0.08} |

Notes. Median properties, with the 16th & 84th percentiles, of the FR and COM AGN at 3 GHz VLA-COSMOS. We note that λ_{rk} values are consistent with face-on radio jets (low inclination with respect to the observer's line of sight), while the kinetic component could drop by > 100 times at higher inclinations, converging to the λ_r values. Note: We have also calculated the median D using the LAS from the semi-automatic ML method (for the secure measurements) presented in Appendix C, in combination with the by-hand measurements for non-secure measurements. The results are similar to the median D derived with the by-hand only measured LAS: $D_{\text{FRII}} = 105.6^{212.9}_{30.4}$ kpc; $D_{\text{FRI/FRII}} = 37.5^{118.1}_{23.0}$ kpc; $D_{\text{FRI}} = 29.0^{60.4}_{16.6}$ kpc. The median D values derived by using the combination of the ML and by-hand methods are up to ~ 1 kpc smaller than the values calculated with the by-hand LAS measurements alone. This is related to the semi-automatic method underestimating the sizes in cases of diffuse radio emission.

hibit inefficient accretion with sub-Eddington values (Heckman & Best, 2014). Still, Kauffmann et al. (2008) study emission line radio AGN from the SDSS and find there is no dependence of radio power and accretion rate to black hole mass. This is also shown by the study of Gendre et al. (2013) of 206 radio galaxies below $z \leq 0.3$ ($S_{1.4\text{ GHz}} \geq 1.5$), with no dependence between extended radio structure and accretion mode. Since we are calculating Eddington ratios using X-ray empirical relations and a different methodology, we cannot directly compare these studies to ours. We do find though that all radio AGN objects in our sample have sub-Eddington ratios, with on average values $< 1\%$ for λ_r , and that on average FRIIs accrete at similar rates to FRIs. We are probing fainter populations of radio AGN than studied before, which are found to produce large (up to 1 Mpc) jets/lobes and are bright (up to $10^{25} \text{ W Hz}^{-1} \text{ sr}^{-1}$ at 3 GHz) FR objects.

If we keep radio power fixed, then we see that Eddington ratio is not dependent on radio structure in the radiative case (Fig. 10). In the radiative plus kinetic case, there is a slight dependence on radio power and radio structure, with a large overlap. Our results suggest there is no direct dependence of FR radio structure and FR radio power to how efficient matter is accreted onto the SMBH, and for sub-Eddington accreters found in our sample there is a mixture of populations; the latter is as also shown in Gendre et al. (2013).

Regarding the FR dichotomy, Fernandes et al. (2015) have shown, in a sample of $z \sim 1$ radio sources (at the average redshift of the FR population in our sample), that the FR dichotomy is evident with the inclusion of kinetic energy in the calculation of the Eddington ratio; without the kinetic component there is no dichotomy. Their sample is composed of much brighter samples of radio sources than ours, from the 3C, 6C, 7C, TOOT00 radio surveys with the faintest objects at $L_{151\text{ MHz}} \sim 10^{25.4} \text{ W Hz}^{-1} \text{ sr}^{-1}$; this translates to $L_{3\text{ GHz}} \sim 10^{24} \text{ W Hz}^{-1} \text{ sr}^{-1}$ for $\alpha = 0.7$, again the region probing the brightest objects of our sample. We do not see such dichotomy in our sample related to accretion rate, but rather an overlap in their distributions. We conclude that the populations we are probing do not present a clear dichotomy in

FR radio structure and accretion mode is not dependent on radio structure nor radio luminosity.

4.3. Large-scale environment

We have explored several probes of the large-scale environment the FRs and COM AGN at 3 GHz VLA-COSMOS lie within, from X-ray groups, density fields, as well as the type of large-scale environment and host. We have seen that FRs lie on average at similar density Mpc-scale environments but the average values presented in Table 5 show that FRIs within COSMOS lie in less dense environments than FRIIs and FRI/FRIIs. This is in contrast to the study of Castignani et al. (2014) of 32 FRIs at 1.4 GHz for $1 < z < 2$ at COSMOS. For comparison we inspect the panel of Fig. 15 covering the same redshift range. We see that FRIs lie on average in less dense environments than FRIIs. We investigate further to understand the difference between the Castignani et al. (2014) and our results. In our study we find discrepancies in the FR classification between 1.4 and 3 GHz, with 16 objects having different classification. In Castignani et al. (2014) they deem FRIs all objects below the FRI/FRII radio luminosity divide of $4 \times 10^{32} \text{ erg s}^{-1} \text{ Hz}^{-1}$. The classification method between Castignani et al. (2014) and our study is different, as we do not adopt a luminosity divide between the classes but rather follow the classic definition by Fanaroff & Riley (1974); this is the reason behind the discrepancy in our results.

Another important point is to explore whether excitation mode is linked to the environment. Gendre et al. (2013) find a correlation, with high-excitation galaxies lying almost exclusively in low-density environments, while low-excitation galaxies are found in a wide range of environments. As we mentioned above, we cannot do a one-to-one comparison to literature results due to the different methods applied in the calculation of the Eddington ratios. Nevertheless, we do not see this in our study (see Table 5), unless we only take into account the radiative Eddington ratios. The objects, FRIs in this case, with high on-average Eddington ratios, live in less dense environments, but not exclusively; there is a wide range of environments. With the

addition of kinetic energy, objects with high Eddington ratios, the FRIIs in our sample, lie on-average in dense environments, but are also found in a wide range of environments.

Regarding the location of the FR host within a group, our results show that there is no preferred location within a group (~ 400 kpc - 1 Mpc; see Fig. 13) with FR type. They can be associated with either the central or a satellite galaxy (see Fig. 16). Similarly, for the jet-less COM AGN, there is no preference for group environment nor a host.

4.4. AGN quenching star formation

Our results on the FR and COM AGN hosts, as presented in Fig. 11, show that the AGN fraction is high in SFGs below the MS. This becomes more obvious when we compare the FR objects to the sample of SFGs at 3 GHz VLA-COSMOS in Fig. 18. The latter include all radio sources at 3 GHz with confirmed hosts (Smolčić et al., 2017b) excluding radio AGN, i.e. the FRs and COM AGN. SFGs dominate the MS in Fig. 18–Left, while FRs are mainly found at the green valley and red-and-dead region of the $\Delta sSFR-M_*$ diagram. In particular we have 72 FRs below the MS compared to 751 SFGs, and 28 FRs within the MS compared to 4024 SFGs. We interpret the high fraction of FR objects below the MS as radio-mode feedback on the massive hosts ($> 10^{10.5} M_\odot$). We also see a continuation from the SFG cloud to the FR cloud below the MS for SFGs, hinting on radio-mode feedback quenching SF. Radio-mode feedback, contrary to radiative-mode feedback, is considered the maintenance mode of quenching in galaxies (Fabian, 2012), regulating star formation in massive galaxies by heating the galaxy halo and halting future rejuvenation of star formation caused by a fountain effect. We note that there is no dependence on the linear-projected size of the FR objects and its location on the $\Delta sSFR-M_*$ diagram.

COM AGN occupy the same region as FRs in the $\Delta sSFR-M_*$ diagram, but can be found also on less massive hosts ($\sim 10^{9.5-11.5} M_\odot$) below the MS when compared to FRs (see Fig. 11). We note that the majority of COM AGN cluster around $\sim 10^{10.8} M_\odot$, while FRs have more massive quenched hosts on average ($\sim 10^{11.3} M_\odot$). These results suggest that both FRs and COM AGN quench their hosts. As we mentioned before, in the COM AGN sample there might be jetted sources which cannot be revealed with the current survey. Our findings are in line with the study of Smolčić et al. (2017c) who find radio-mode AGN feedback is present in the hosts of the 3 GHz VLA-COSMOS AGN at each cosmic epoch since $z \sim 5$.

In Fig. 11 we have marked sources observed at X-rays with Chandra (Marchesi et al., 2016) with an 'x'. The idea was to investigate the presence of X-ray emission and the relation to galaxy quenching. Around half of the FRs below the spread of the MS have X-ray identifications. This can suggest the presence of both mechanisms in order to quench star formation in their host, but to pinpoint which mechanism is the responsible for permanently quenching star-formation we would need to know the duty cycle of these radio AGN and their lifetimes, an information which we do not currently have.

We find that the radio AGN within X-ray groups that occupy massive hosts below the MS for SFGs (see Fig. 14), reside in progressively cooler groups the older their episode of SF is. In other words, the objects leaving the MS for SFGs are the ones found in warmer X-ray groups indicating heating of the IGM from the AGN. When hosts have moved to the red-and-dead region of the $\Delta sSFR-M_*$ diagram, their group temperatures are cooler, suggesting a termination of the heating of the IGM through mechanical feedback.

Darvish et al. (2017), from their study of COSMOS large-scale environments, argue that the role of the cosmic web environment is very important in controlling star-formation in galaxy hosts, with satellite galaxies controlling the SF fraction in galaxies and with centrals controlling the overall SFR. Their sample includes SFGs as well as quiescent galaxies up to $z \sim 1.2$. They find rapid quenching in most satellites as they transit through filaments from the field to clusters. As we have shown in Figs 16 & 17, we see indications for SF quenching in satellites of specific types of radio AGN, namely for FRIIs and FRI/FRIIs. The latter classes seem to quench their host much more efficiently than FRIIs and COM AGN, for the similar time period from the last burst of star formation. FRIIs and hybrids in our sample are on-average slight more powerful at radio than FRIIs at 3 GHz VLA-COSMOS. This could justify that the energy they release into their environment in the form of mechanical energy is higher than in FRIIs, providing the necessary heating to the gas within the circum-galactic medium (CGM) to quench efficiently star formation in the host.

4.5. Comparison to S^3 -SEX semi-empirical simulation

We compare our sample to the S^3 -SEX semi-empirical simulation¹² of Wilman et al. (2008), a simulation of extragalactic radio continuum sources in a sky area of $20 \times 20 \text{ deg}^2$ out to redshift of 20. The sources are drawn from empirical data, and for the purposes of the simulation, extrapolated beyond the observational limits of the surveys. The simulation offers a radio AGN classification relevant to our study: FRI, FRII and gigahertz-peaked (GPS) sources, which are jet-less sources with their radio spectral energy distribution peaking at GHz frequencies. The 151-MHz luminosity function from Willott et al. (2001) is used to simulate these populations. We run the online query for 1.4 GHz sources above flux densities¹³ of $17 \mu\text{Jy}$ up to redshift of 6. To avoid cosmic variance we chose an area much larger than COSMOS and select the full area covered by the simulation, which yields 2,285,085 sources. Within this volume, the FRIIs are 330,694, the FRIIs 2,080, while GPS sources are 16,650. The result of the simulation is presented in Fig. 19, with FRIIs dominating the luminosity-redshift parameter space reaching the flux-density limit we selected. FRII radio sources are found above luminosities of $\sim 10^{24} \text{ W Hz}^{-1} \text{ sr}^{-1}$ at 1.4 GHz and at redshifts above ~ 0.3 . GPS sources are also widely distributed reaching down to the flux-density limit we chose.

To compare the 3 GHz FRs and COM AGN to the simulation we scale the S^3 -SEX simulation down to the 2.3 deg^2 of the 3 GHz VLA-COSMOS survey and get in total ~ 13139 sources with ~ 1901 FRIIs (8%), ~ 12 FRIIs (0.01%) and ~ 96 GPS (0.7%) sources in the simulation. Note: the radio spectral index $\alpha = 0.7$ used to convert the flux-density limit of 3 GHz VLA-COSMOS to 1.4 GHz might affect the number of sources drawn by the simulation. From the 10830 sources within 3 GHz VLA-COSMOS we have 39 FRIIs (0.3%), 32 FRI/FRII (0.2%), 59 FRIIs (0.5%) and 1818 COM AGN ($\sim 17\%$). Despite the results of cosmic variance, as with COSMOS we only observe a small patch of the sky, there is a clear difference between the simulation and data, which is the number of FRII and FRI sources recovered. At 3 GHz VLA-COSMOS we recover 5 times more FRIIs than the S^3 -SEX simulation, for the same sky area and

¹² http://s-cubed.physics.ox.ac.uk/s3_sex

¹³ We convert the $10 \mu\text{Jy}$ flux-density limit of the 3 GHz VLA-COSMOS survey to 1.4 GHz using a standard steep radio spectral index of 0.7.

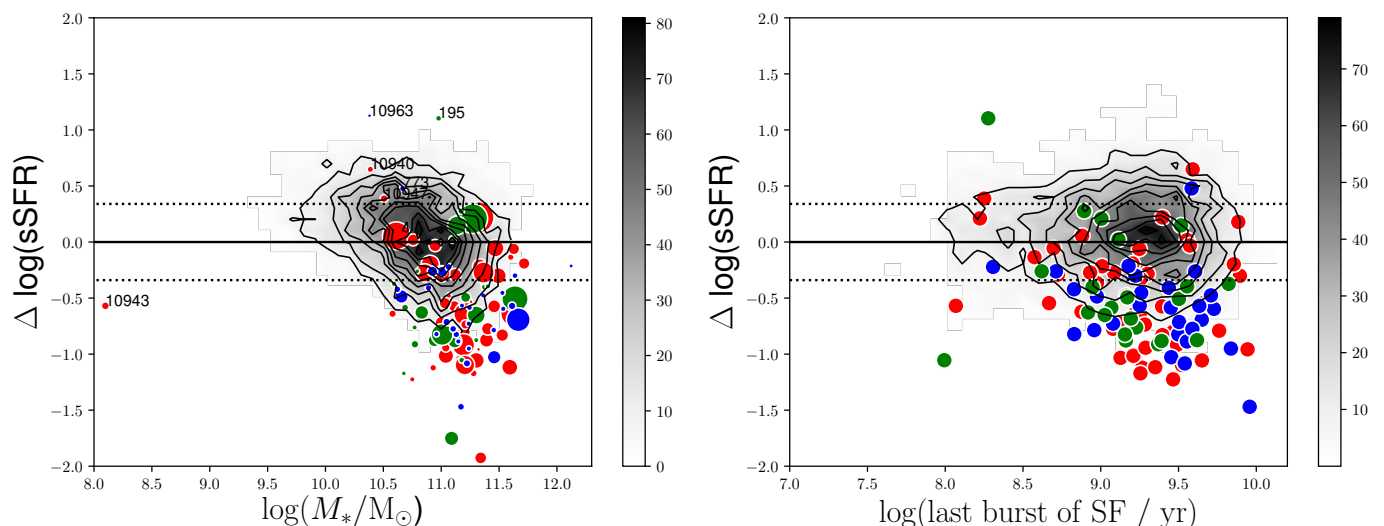


Fig. 18: **Left:** $\Delta \log(\text{sSFR})$, the difference between specific SFR and the specific SFR of objects in the MS, as a function of stellar mass for the FR objects, shown in colour, compared to the pure SFGs at 3 GHz (Smolčić et al., 2017b), shown in black as density plot. For FR objects, symbols are scaled based on their linear-projected size, with larger symbols corresponding to larger objects. FRIIs are shown in red, FRI/FRIIs in green and FRIs in blue. The solid and dotted lines show the main sequence for star forming galaxies and spread, based on Whitaker et al. (2012). **Right:** $\Delta \log(\text{sSFR})$, as on the left, versus the star-formation history (SFH) of each object. SFH are estimated from the fit to the SED as described in Sec. 3.3.1. We exclude COM AGN objects from these plots for clarity. COM AGN are shown in Fig. 11.

depth. This is mainly attributed to the combination of high resolution and sensitivity of 3 GHz VLA-COSMOS being able to recover FRII-type radio sources at lower flux densities than probed before, and with lower surface brightness. This demonstrates that the traditional FR classification scheme of Fanaroff & Riley (1974) is surface brightness biased towards brighter and larger FRIIs. On the other hand the simulation predicts a factor of 50 more FRI sources than what we observe at 3 GHz VLA-COSMOS. These are either not resolved by our survey and lie within the COM AGN population, or are not observed due to them being too faint to be detected at higher redshifts.

In Fig. 20 we present a normalised histogram of the redshift distribution for the S^3 -SEX simulation where we over-plot the 3 GHz VLA-COSMOS FR and COM AGN objects. The difference in the redshift distribution of FRII sources is evident, with our survey revealing an FRII population at lower redshifts, peaking around redshift of one; the simulation is peaking above redshift of two for FRIIs. Furthermore, FRIIs in our sample are fainter on average at 3 GHz than the FRIIs from the simulation¹⁴, as can be seen in Fig. 21. In conclusion, the advantage of the 3 GHz VLA-COSMOS survey over past surveys and extrapolated data is that it recovers FRII-type radio AGN at lower redshifts and at lower flux densities than before. Still, as we already mentioned, this is related to the surface-brightness bias linked to the FR classification scheme, but it can also be due to the resolution. At higher redshifts is hard to disentangle the FRII radio structure. The smallest confirmed FRII at 3 GHz VLA-COSMOS is object 10937 ($D = 24.3$ kpc, $z = 1.128$; $LAS = 2.96$ arcsec). This is due to the capabilities of our survey: at $z = 1$ (2) with a resolution of 0.75 arcsec we can disentangle sources with sizes of 6 (6.2) kpc. Object 10937 is a double radio source with lobes ~ 2 arcsec long separated by ~ 1 arcsec, which at the redshift of the source would be ~ 8 kpc (see Fig. C.5).

¹⁴ We convert the 1.4 GHz flux densities from the simulation to 3 GHz flux densities using $\alpha = 0.7$.

When it comes to FRIIs, our sample and the simulation have similar redshift distributions up to $z \sim 2.5$ where we do not detect any FRIIs above that redshift. The radio powers of FRIIs in our sample fall within the predicted values given by the simulation. For the COM AGN and the GPS sources of the simulation we cannot make a one-to-one comparison, since in our sample we do not further classify COM AGN as GPS or not. We present the plots and we caution the reader on the interpretation.

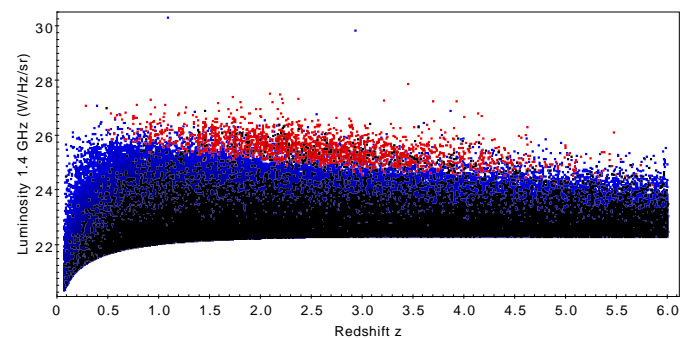


Fig. 19: Radio luminosity at 1.4 GHz versus redshift from the S^3 -SEX semi-empirical simulation (Wilman et al., 2008) for a sky area of $20 \times 20 \text{ deg}^2$ centred at the central coordinates of the simulation, and for a flux-density limit of $17 \mu\text{Jy}$. Blue crosses are FRIIs and red crosses FRIIs, while GPS sources are in black.

4.6. What affects the FR structure?

Classifying radio AGN based on the surface-brightness distribution along their radio structure is a very practical tool and this is why it is widely adopted (e.g. Vardoulaki et al., 2008; Mingo et al., 2019). But as we find it is not fully representative of what we see in nature. The classification depends on viewing angle, resolution and sensitivity. Although using the FR scheme helps in understanding the AGN energy output (e.g. Croston et al., 2018), it is not yet clear what affects the FR structure. In this study of

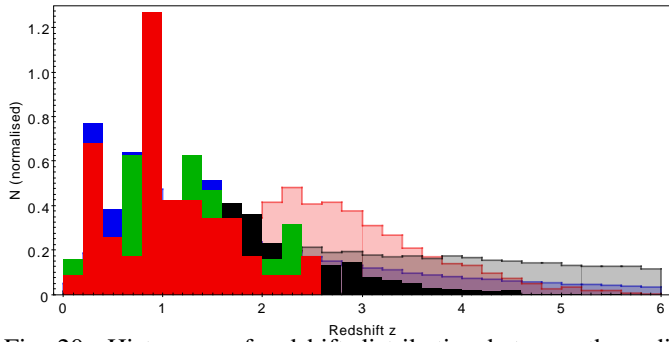


Fig. 20: Histogram of redshift distribution between the radio AGN at the 3 GHz VLA-COSMOS sample and the S^3 -SEX semi-empirical simulation (Wilman et al., 2008) for a sky area of $20 \times 20 \text{ deg}^2$ centred at the central coordinates of the simulation, and for a flux-density limit of $17 \mu\text{Jy}$. The total area of the histogram bars is normalised to unity. Solid histograms correspond to 3 GHz data and semi-filled to the simulation. Bin size is 0.2. Colours: red for FRII, green for FRI/FRII, blue for FRI, black for COM AGN or GPS.

radio AGN at 3 GHz VLA-COSMOS we adopted a parametric approach to classify sources in order not to introduce biases on the classification. Our results on the 3 GHz VLA-COSMOS radio AGN population show there is no strong dependence of radio structure on physical properties (radio luminosity, size, accretion rate) or large-scale environment. Furthermore, there is a mix of populations and overlap of their distributions. We do not see a clear dichotomy in FR type, as first reported by Fanaroff & Riley (1974), rather a wide distribution of values. Comparison of jetted FR objects to jet-less COM AGN within the 3 GHz sample suggests they are drawn from the same population (see Fig. 11) when it comes to their host properties. They also lie in similar density environments. But there are differences: COM AGN are more numerous, and on average fainter, they lie at higher redshifts, they have smaller sizes ($\sim 2 \text{ kpc}$), and they have similar accretion rates only to FRIs when the kinetic energy is not taken into account. We note that this study does not take into account projection effects, nor redshift dependence, which could potentially change the FR classification since the surface brightness decreases with redshift as $(1+z)^{-4}$.

At 3 GHz VLA-COSMOS we probe radio AGN, extended or not, down to flux-densities of tens of μJy . The lowest flux density we probe for an extended FR-type sources is object 3065 at $70 \mu\text{Jy}$. This is achieved thanks to the combination of high resolution ($0''.75$) and sensitivity ($2.3 \mu\text{Jy}/\text{beam}$) of the survey, which allows us to detect small FR sources down to low flux-density limits, but it also affects the way they are classified based on the FR-type classification. When comparing, for the same object, the 3 GHz to the 1.4 GHz VLA-COSMOS classifications we find that 16% (21 out of 130) sources have different classification, making the FR classification-scheme resolution and sensitivity dependent. In other words, there is a surface-brightness bias related to the FR classification scheme. Additionally, the classification could depend on frequency and the effect of synchrotron ageing/losses. Thus trying to understand the relation between physical properties and environment with the FR radio structure is not trivial.

Our results suggest that the FRI radio structure is not a result of the large-scale environment, but might be due to the effects of the environment within the host, i.e. on smaller scales. It has been long speculated that the ISM of the host can play a role in affecting the FR structure, causing the FR dichotomy. For

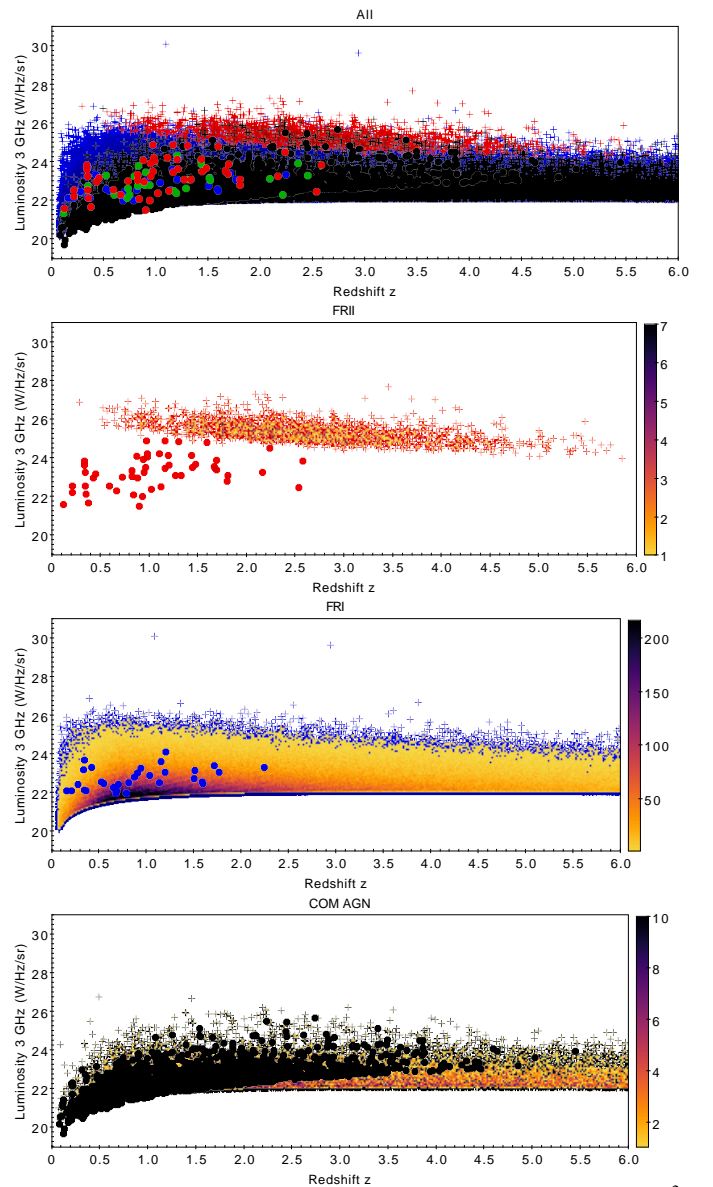


Fig. 21: Radio luminosity at 3 GHz versus redshift from the S^3 -SEX semi-empirical simulation (Wilman et al., 2008) for a sky area of $20 \times 20 \text{ deg}^2$ centred at the central coordinates of the simulation, and for a flux-density limit of $17 \mu\text{Jy}$. We use a typically steep radio spectral index for converting the 1.4 GHz radio fluxes provided by the simulation to 3 GHz. Blue crosses are FRIs and red crosses FRIIs, while GPS sources are in black. We over-plot the 3 GHz VLA-COSMOS as solid circles with red (FRII), green (FRI/FRII), blue (FRI) and black (COM AGN). We also show panels for each class, for clarity. The bar on right gives then number density of sources in the simulation. Note: the bottom panel shows GPS sources from the simulation and COM AGN from 3 GHz VLA-COSMOS, but a one-to-one comparison cannot be made as COM AGN are not further classified as GPS or not.

example, Bicknell (1995) attribute this difference to the different speeds the FR jets propagate through the ISM, being supersonic for FRIIs or transonic and eventually subsonic for FRIs. Meier (2013) explain why the FR dichotomy cannot originate very close to the black hole, on sub-pc scales, where the jets are being produced, due to the existence of hybrid FR structures.

Any asymmetries in the jet production would disappear within timescales of months for $M_{\text{BH}} \sim 10^9$, while the differences are seen on timescales of tens of Myrs. Thus they attribute the FR dichotomy to kpc-scale or less, and they present a model where the recollimation shock is responsible for the difference in FR structures, with the jets being reborn in the post-recollimation shock depending on the strength of the recollimation shock. If the recollimation shock, occurring at pc scales, is strong enough we get a supersonic/magnetosonic flow resulting in an FRII jet, while if it is not strong enough to dissipate much of the internal magnetic field an FRI subsonic jet is being produced. Another possibility is the type of ISM the jet encounters, being more or less dense. Recently, [Perucho \(2020\)](#) computed a model where FRI jets are disrupted as they encounter stars in the ISM of the host galaxy. Based on this model, turbulence is one of the reasons for the jet losing energy and not developing to an FRII-type jet. Given the current available data for our sample we cannot verify this observationally, but it is a very interesting topic for future studies with high-resolution observations (e.g. ALMA) to probe the ISM of FR-type radio sources within COSMOS. With our current data on the FR radio AGN in COSMOS we cannot verify these studies.

As we probe deeper and deeper the radio universe we will discover more of these discrepancies regarding the classic FR classification of [Fanaroff & Riley \(1974\)](#). As we said, the FR classification scheme is a very practical tool, but future surveys which will have to classify millions of sources will run into the same issues we have demonstrated with our small sample. We believe that if we want to continue using the FR classification we should apply additional parameters to it, such as a radio power cut. Otherwise, we should start classifying extended radio AGN with a scheme more related to their physical properties.

5. Conclusions

In this study we have investigated the connection of the radio structure in radio-selected AGN from the 3 GHz VLA-COSMOS survey ([Smolčić et al., 2017a](#)) to their physical properties (radio power, size, accretion rate) and large-scale environment (hosts, galaxy groups, density fields). The purpose of this study is to address the complexity of connecting the radio structure to physical properties and to find what drives the FR-type radio structure. We adopt a parametric classification and classify our sample in FRIIs, FRIs and FRI/FRIIs. We also include the jet-less COM AGN in our analysis. In summary, our results are:

1. Within the 2.6 deg² of the COSMOS field at 3 GHz we find 130 FR-type radio AGN (59 FRIIs, 32 FRI/FRIIs, 39 FRIs) and 1818 COM AGN.
2. We push the detection limit of FR-type radio sources to tens of μJy at 3 GHz, deeper than past surveys. This is related to the combination of high resolution ($0''.75$) and sensitivity (2.3 mJy/beam) of 3 GHz VLA-COSMOS survey. The smallest FRII we detect is object 10937, with $D = 24.3 \text{ kpc}$ at $z = 1.128$, and the faintest FR object is 3065 at $70 \mu\text{Jy}$.
3. FR objects can be detected up to redshifts of $z \sim 2.5$, with a peak in their distribution around $z \sim 1$, while COM AGN are detected up to $z \sim 6$ with a peak around $z \sim 1.8$.
4. There is no clear dichotomy in the FR radio structure. The traditional FR dichotomy is based on populations which are much brighter and disappears when we probe much fainter populations of radio sources ($L_{3 \text{ GHz}} < 10^{25} \text{ W Hz}^{-1} \text{ sr}^{-1}$).
5. The FR-type radio classification scheme is surface-brightness biased. We find 21 out of 130 sources at 3 GHz

having different FR classification from their analogues at 1.4 GHz.

6. FRII objects are on average larger than FRI/FRII and FRI objects by a factor of 2 and 3, respectively, but there is an overlap in their distributions. On average, FR objects have similar radio luminosities at 3 GHz. COM AGN are smaller in size than FRs and are located at larger on average distances, but have similar radio luminosity at 3 GHz as FRs.
7. Kinetic energy or jet power boosts the Eddington ratio and thus the accretion power, as expected, but does not explain the classic FR dichotomy. There is an overlap in the distributions of FRII, FRI/FRII and FRI objects.
8. The radio AGN at 3 GHz VLA-COSMOS have sub-Eddington ratios, with FRIIs accreting matter onto their BHs at similar rates to FRIs, and they produce large FRII objects with jets extending up to $\sim 1 \text{ Mpc}$.
9. FRs and COM AGN are distributed randomly within the virial radius of their X-ray galaxy group, and their distributions peak around $r/r_{200} \sim 0.3 \pm 0.2$. Brighter COM AGN tend to lie closer to the X-ray group centre.
10. FR objects occupy in their majority massive hosts ($> 10^{10.5} M_{\odot}$). At the same time there is an indication for radio-mode quenching of star-formation in the hosts, with FRIs in satellite hosts being less efficient in quenching SF than FRI/FRIIs and FRIIs. We also find five radio AGN with jets lying in the starburst region above the MS for SFGs.
11. Objects below the MS for SFGs, related to massive hosts, lie in cool X-ray groups with average IGM temperatures of $\sim 1 \text{ keV}$. Additionally, the older the episode of star formation the cooler the X-ray group FRs lie within, suggesting quenching of SF within X-ray groups due to kinetic feedback.
12. Contrary to findings reported in literature, we do not find a connection between the density of the environment and the FR object type.
13. The advantage of the 3 GHz VLA-COSMOS survey when compared to the S³-SEX semi-empirical simulation is that it recovers FRII-type radio AGN at lower redshifts and at lower flux densities than expected.

The results of this study show that adopting the classic FR-type classification to categorise radio AGN should be used with care when comparing different samples, selected at different depths and sensitivities. Care should also be taken when the classic FR classification is used on future radio surveys which will probe the radio universe with higher sensitivity and resolution. We have shown that the FR-type classification is surface-brightness biased, which makes it extremely difficult to investigate the reason for the FR dichotomy reported in [Fanaroff & Riley \(1974\)](#). Although the FR-type classification is a useful tool to characterise extended radio sources associated with AGN, it can lead to inconsistent results when the caveats are not taken into account. A work-around the caveats we mentioned is to expand the classic FR classification to be more representative of the bright and faint radio sky, given the current and future discoveries. An improved classification could include a stronger link to physical properties rather than the surface-brightness distribution, i.e. a radio power cut or/and an Eddington ratio cut, and orientation information which can come from modelling the sources. Follow-up of our study should investigate the sub-kpc scale environments of radio AGN (e.g. with ALMA) to study the interaction of jet-ISM and understand the role of small-scale environment to the radio structure.

Acknowledgements. EV acknowledges funding from the DFG grant BE 1837/13-1 and from the VLBI group in MPIfR. ID is supported by the European Union's Horizon 2020 research and innovation program under the Marie

Skłodowska-Curie grant agreement No 788679. Support for BM was provided by the DFG priority program 1573 "The physics of the interstellar medium". EV, EFJA, AK, BM and FB acknowledge support of the Collaborative Research Center 956, subproject A1 and C4, funded by the Deutsche Forschungsgemeinschaft (DFG). EV and EFJA would like to thank Nils Linz, Vishnu Balakrishnan for their assistance during the first phase of radio classification.

References

- Baldi, R. D.; Capetti, A.; Massaro, F., 2018, *A&A*, 609A, 1
 Baldi, R. D., Capetti, A., Giovannini, G., 2015, *A&A*, 576, 38
 Berta, S., Lutz, D., Santini, P., et al. 2013, *A&A*, 551, A100
 Best, P. N.; Heckman, T. M., 2012, *MNRAS*, 421, 1569
 Bicknell, G.V., 1995, *Astroph. J. Supp. Ser.*, 101, 29:39
 Blundell, Katherine M.; Rawlings, Steve; Willott, Chris J., 1999, *AJ*, 117, 677
 Blundell, K. M.; Rawlings, S., 1999, *ASPC*, 193, 75
 Bondi, M., Ciliegi, P., Schinnerer, E., et al. 2008, *ApJ*, 681, 1129
 Castignani, G., Chiaberge, M., Celotti, A., et al. 2014,
 Cavagnolo, K. W., McNamara, B. R., Nulsen, P. E. J., et al., 2010, *ApJ*, 720, 1066
 Cheng, 1995, Mean shift, mode seeking, and clustering. *Pattern Analysis and Machine Intelligence, IEEE Transactions on*, 17(8):790-799
 Chiaberge, M., Tremblay, G., Capetti, A., et al. 2009, *ApJ*, 696, 1103
 Civano, F., Elvis, M., Brusa, M., et al. 2012, *ApJS*, 201, 30
 Civano, F., Marchesi, S., Comastri, A., et al. 2016, *ApJ*, 819, 62
 Croston, J. H.; Ineson, J.; Hardcastle, M. J., 2018, *MNRAS*, 476, 1614
 Dabhade, P.; Röttgering, H. J. A.; Bagchi, J.; Shimwell, T. W.; Hardcastle, M. J.; Sankhyayan, S.; Morganti, R.; Jamroz, M.; Shulevski, A.; Duncan, K. J., 2020, *A&A*, 635A, 5
 Daly, Ruth A.; Sprinkle, Trevor B.; O’Dea, Christopher P., et al. 2012, *MNRAS*, 423, 2498
 Darvish, B.; Mobasher, B.; Martin, D.C; et al., 2017, *ApJ*, 837, 16
 Darvish, B., Mobasher, B., Sobral, D., et al. 2015, *ApJ*, 805, 121
 Davidzon, I.; Ilbert, O.; Laigle, C., et al., 2017, *A&A*, 605A, 70
 Delvecchio, I., Smolčić, V., Zamorani, G., et al., 2017, *A&A*, A3
 da Cunha, E., Charlot, S., & Elbaz, D. 2008, *MNRAS*, 388, 1595
 Yohan Dubois, Julien Devriendt, Romain Teyssier, Adrienne Slyz, 2011, *MNRAS*, 417, 3
 Elvis, M., Civano, F., Vignali, C., et al. 2009, *ApJS*, 184, 158
 Fabian 2012, *ARA&A*, 50, 455
 2003, *RMxAC*, 17, 303
 Falcke, Heino; Biermann, Peter L., 1999, *A&A*, 342, 49
 Fanaroff, B. L., Riley, J. M., 1974, *MNRAS*, 167, 31
 Fernandes, C. A. C., Jarvis, M. J., Martínez-Sansigre, A., et al. 2015, *MNRAS*, 447, 1184
 Fukunaga and Hostetler, L. D., 1975 The estimation of the gradient of a density function, with applications in pattern recognition. *IEEE Transactions on Information Theory*, 21:32-40
 Gaspari, M.; Tombesi, F.; Cappi, M., 2020, *NatAs*, 4, 10
 Gendre, M. A., Best, P. N., Wall, J. V., et al. 2013, *MNRAS*, 430, 3086
 George, M. R., Leauthaud, A., Bundy, K., et al. 2011, *ApJ*, 742, 125
 Ghisellini, G.; Haardt, F.; Ciardi, B.; Sbarrato, T.; Gallo, E.; Tavecchio, F.; Celotti, A., 2015, *MNRAS*, 452, 3457
 Gopal-Krishna; Wiita, P. J., 2001, 2001, *A&A*, 373, 100
 Gopal-Krishna; Wiita, Paul J., 1988, *Nature*, 333, 49
 Gozaliasl, G., Finoguenov, A., Khosroshahi, H. G., et al. 2020, *A&A*, 635, A36
 Gozaliasl, G., Finoguenov, A., Tanaka, M., et al. 2019, *MNRAS*, 483, 3545
 Hales, C. A., Murphy, T., Curran, J. R., et al. 2012, *MNRAS*, 425, 979
 Heckman, T. M., Best, P. N., 2014, *ARA&A*, 52, 589
 Ilbert, O., McCracken, H. J., Le Fevre, O., et al. 2013, *A&A* 556, A55
 Jiménez-Andrade, E. F.; Magnelli, B.; Karim, A., et al., 2019, *A&A*, 625A, 114
 Kaiser, Christian R.; Dennett-Thorpe, Jane; Alexander, Paul, 1997, *MNRAS*, 292, 723
 Kaiser, Christian R.; Best, Philip N., 2007, *MNRAS*, 381, 1548
 Kauffmann, G.; Heckman, T. M.; Best, P. N., 2008, *MNRAS*, 384, 953
 Kunert-Bajraszewska, M; Gawronski, M. P.; Labiano, A., Siemiginowska, A., 2010, *MNRAS*, 408, 2261
 Lacerda, Eduardo A. D.; Sanchez, Sebastian F.; Cid Fernandes, R. et al., 2020, *MNRAS*, 492, 3073
 Laigle, C., McCracken, H. J., Ilbert, O., et al. 2016, *ApJS*, 224, 24
 Laing, R. A., 1994, *ASPC*, 54, 227
 Ledlow, M. J. & Owen, F. N., 1996, *Astron. J.*, 112, 9
 Lee, Nicholas; Sanders, D. B.; Casey, Caitlin M., et al. 2015, *ApJ*, 801, 80
 Leslie, Sarah K.; Schinnerer, Eva; Liu, Daizhong, et al. 2020, *ApJ*, 899, 58
 Lusso, E., Comastri, A., Simmons, B. D., et al., 2012, *MNRAS*, 425, 623
 Lutz, D., Poglitsch, A., Altieri, B., et al. 2011, *A&A*, 532, A90
 Magliocchetti, M.; Popesso, P.; Brusa, M.; Salvato, M., 2018, *MNRAS*, 478, 3848
 Marchesi, S., Lanzuisi, G., Civano, F., et al., 2016, *ApJ*, 830, 100
 Marconi, A., Hunt, L. K., 2003, *ApJ*, 589L, 21
 Meier, D. L., 2013, *EPJWC*, 61, 01001
 Meier, David L., 2001, *AIPC*, 586, 420
 Merloni, Andrea; Heinz, Sebastian, 2007, *MNRAS*, 381, 589
 Mingo, B.; Croston, J. H.; Hardcastle, M. J.; Best, P. N.; et al. 2019, *MNRAS*, 488, 2701
 Mingo, B.; Hardcastle, M. J.; Croston, J. H.; Dicken, D.; Evans, D. A.; Morganti, R.; Tadhunter, C., 2014, *MNRAS*, 440, 269
 Mohan & Rafferty, 2015, *ASCL*, 1502.007
 Oliver, S. J., Bock, J., Altieri, B., et al. 2012, *MNRAS*, 424, 1614
 O’Sullivan, E.; Giacintucci, S.; David, L. P., et al. 2011, *ApJ*, 735, 11
 Owen, F. N.; Ledlow, M. J., 1994, 1994, *ASPC*, 54, 319
 Perucho, M., 2020, *MNRAS*, 494L, 22
 Sadler, E. M., 2016, *AN*, 337, 105
 Sadler, E. M., Ekers, R. D., Mahony, E. K., Mauch, T., Murphy, T., 2014, *MNRAS*, 438, 796
 Schreiber, C., Pannella, M., Elbaz, D., et al. 2015, *A&A*, 575, A74
 Schinnerer, E., Sargent, M. T., Bondi, M., et al. 2010, *ApJS*, 188, 384
 Scoville, N.; Lee, N.; Vanden Bout, P., et al. 2017, *ApJ*, 837, 150
 Scoville, N., Arnouts, S., Aussel, H., et al., 2013, *ApJS*, 206, 3
 Shen, Lu; Liu, Guilin; Zhang, Mengfei et al, 2020, arXiv:200903343
 Smolčić, V., Novak, M., Bondi, M., et al. 2017, *A&A*, A1
 Smolčić, V., Delvecchio, I., Zamorani, G., et al. 2017, *A&A*, A2
 Smolčić, V., Novak, M., Delvecchio, I., et al. *A&A*, 602, A6
 Smolčić, V.; Finoguenov, A.; Zamorani, G.; Schinnerer, E.; Tanaka, M.; Giodini, S.; Scoville, N., 2011, *MNRAS*, 416L, 31
 Smolčić, V., 2009, *ApJ*, 699L, 43
 Speagle, J. S., Steinhardt, C. L., Capak, P. L., & Silverman, J. D. 2014, *ApJS*, 214, 15
 Symeonidis, M., Georgakakis, A., Page, M. J., et al., 2014, *MNRAS*, 443, 3728
 Taniguchi, Y., Kajisawa, M., Kobayashi, M. A. R., et al. 2015, *PASJ*, 67, 104
 Taniguchi, Y., Scoville, N., Murayama, T., et al. 2007, *ApJS*, 172, 9
 Tozzi, P., Gilli, R., Mainieri, V., et al., 2006, *A&A*, 451, 457
 Turner, R. J. and Shabala, S. S., *ApJ*, 806, 59
 Vardoulaki, E., Jimenez Andrade, E. F., Karim, A., et al. 2019, *A&A*, 627A, 142
 Vardoulaki, Eleni; Rawlings, Steve; Simpson, Chris, et al. 2008, *MNRAS*, 387, 505
 Vardoulaki, E., 2013, 10th Hellenic Astronomical Conference, Proceedings of the conference held at Ioannina, Greece, 5-8 September 2011. Edited by Iossif Papadakis and Anastasios Anastasiadis
 Vardoulaki, E.; Rawlings, S.; Hill, G. J.; Mauch, T.; Inskip, K. J.; Riley, J.; Brand, K.; Croft, S.; Willott, C. J., 2010, *MNRAS*, 401, 1709
 Vardoulaki, E., 2009, "Understanding the nature of the faint radio-source population", Oxford University, UK
 Weinberger, Rainer; Springel, Volker; et al., 2018, *MNRAS*, 479, 4056
 Willott, Chris J.; Rawlings, Steve; Jarvis, Matt J.; Blundell, Katherine M., 2003, *MNRAS*, 339, 173
 Willott C.J., Rawlings S.G., Blundell K.M., Lacy M., Eales S.A., 2001, *MNRAS*, 322, 536
 Willott, Chris J.; Rawlings, Steve; Blundell, Katherine M.; Lacy, Mark, 1999, *MNRAS*, 309, 1017
 Wilman, R. J.; Miller, L.; Jarvis, M. J.; Mauch, T.; Levrier, F.; Abdalla, F. B.; Rawlings, S.; et al. 2008, *MNRAS*, 388, 1335
 Whitaker, K. E., van Dokkum, P. G., Brammer, G., Franx, M., 2012, *ApJ*, 754L, 29
 Xue, Y. Q.; Brandt, W. N.; Luo, B., et al., 2010, *ApJ*, 720, 368
 Zirbel, E. L., 1997, *ApJ*, 476, 489

Appendix A: A parametric approach to FR classification

In this Section we describe the method we used to classify radio sources based on the FR classification scheme (edge-brightened or edge-darkened radio sources, Fanaroff & Riley, 1974). We followed a three-stage method, which involved visual inspection from non-experts (stage 1), visual inspection from experts (stage 2), and determination of FR type (stage 3).

Appendix A.1: Stage 1: sample of 350 sources inspected by a team of non-experts on FR objects

The sample of 350 objects within the envelope in Fig. 1 was given to 7 investigators, non-experts in FR-type radio AGN in their majority, to classify the objects based on the following guidelines:

1. FR II: if objects are edge-brightened and exhibit lobes.
2. FR I: if objects are edge-darkened and exhibit jets.
3. FR I/FR II: if objects are FR I on one side and FR II on the other.
4. radio source (RS): none of the above.

This classification was then taken to stage 2, to be inspected by experts on FR-type objects, in order to avoid creating a sample of FR objects that is not representative of their nature.

Appendix A.2: Stages 2 & 3: determination of FR class

At Stage 2 of the parametric approach, the 350 sources with preliminary classification were inspected by 2 experts on FR objects, and a subsample of 130 objects was taken to stage 3.

Stage 3 involves manually determining which sources are edge-brightened and which edge-darkened. The reason we did not expand on our machine learning technique presented in Sec. C is the very peculiar nature of the majority of the objects, exhibiting bents, as well as the fact some of them are multi-component (composed of several radio blobs). And we leave the development of this machine learning code for FR classification as a future exercise.

In particular, we measure the length to the 3σ contour, which is the maximum projected size of the jet/lobe, at both sides. We call the longer side DL and the shorter SL. We also measure the length to the brightest hotspot at each side of the core, where for the longer side we name it DL_{hs} and for the shorter DS_{hs}. We also measure the bent angle (BA in degrees), which is the angle that the two jets/lobes form in respect to each other. A fully symmetrical source will have BA = 180°, and if the jets/lobes are bent this angle will be smaller.

In case of one-sided jet/lobe we only measure the length to the brightest hotspot and compare it to the length of the 3σ contour. In case there are no obvious hotspots we report only the length to the 3σ contour. The measured values are listed in Table A.1, along with a note if the source is one-sided or not, and the resulting FR classification.

FR II is a edge-brightened source, i.e. the distance to the hotspot is more than 0.5× the distance to the maximum length of the source. If this is less than 0.5, then the source is edge-darkened or FR I.

To account for hybrid FR I/FR II objects, we measure both sides of the source i.e. those that have a lobe on one side and a jet on the other. Thus if DL_{hs} > 0.5×DL then the larger side is FR II, otherwise it is FR I. Similarly with the shorter side, it's classified as FR II if DL_{hs} > 0.5×DL, otherwise as FR I.

In Fig. A.1 we give a visual example of stage 3 of the classification, where we classify objects in FR II, FR I/FR II or FR I based on the surface-brightness distribution along their radio structure.

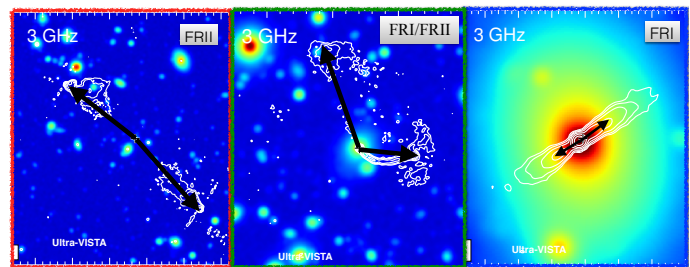


Fig. A.1: Examples of FR II (left), FR I/FR II (middle), and FR I (right) radio sources. The arrows mark the point of high intensity along the radio structure. Contours are the 3 GHz data and the colourscale background is the Ultra-VISTA mosaic (see Fig. 2).

Appendix B: Notes on the FR-type objects

26: This is classified as one-sided FR I source.

33: Classified as a FR I/FR II radio source.

38: A possible FR I/FR II radio source. This object lies in a masked region in the COSMOS2015 catalog because of the presence of saturated or bright source in the optical-to-NIR bands, as shown in Fig. 1 of Smolčić et al. (2017b). As a result it has not been matched with a host.

44: A one-sided diffuse jet which is more evident at the VLA map. We classify it as one-sided FR I. This objects is a NAT and is in the same X-ray group as 10913.

64: A possible FR I/FR II due to the elongated shape. Might be a young source and we might not be resolving the jets not even at our high resolution.

80: A small very symmetric FR I source, with similar structure in both 1.4 and 3 GHz maps. It can also be classified as a twin-jet radio source.

83: A small FR II source with a prominent bent in the structure on the south suggesting interaction with the intergalactic medium.

89: A double source classified as FR II.

112: The VLA-COSMOS map reveals a bent FR I source, or a wide-angle-tail in particular, which is not evident in the lower resolution VLA map. This structure reveals strong interaction with the environment.

115: This source is outside the coverage of the VLA-COSMOS survey and only observed at 3 GHz. It has clear core with joint jet/lobe-like structures, almost symmetric, and is classified as FR I.

123: FR I radio source with particular structure, being more prominent on the south suggesting either diffuse emission or projection effect.

137: FR I source which looks like a fat double radio source, i.e. diffuse lobes not separated from the rest of the source.

138: FR II radio source since the lobes are prominent and the surface-brightness distribution along the structure is closer to the edges, i.e. the source is edge-brightened.

145: FR II radio source, which suggests projections effects as it shows one jet-lobe structure on the south and a lobed structure on the north.

Table A.1: Results of parametric FR classification

Table A.1: Results of parametric FR classification (continued)

| 3 GHz | DL | DS | DL_hs | DS_hs | BA | FR | 3 GHz | DL | DS | DL_hs | DS_hs | BA | FR |
|-------|----------|------|-------|-------|-----|------------------------|-------|----------|------|-------|-------|-----|------------------------|
| ID | (arcsec) | | | (deg) | | class | ID | (arcsec) | | | (deg) | | class |
| (1) | (2) | (3) | (4) | (5) | (6) | (7) | (1) | (2) | (3) | (4) | (5) | (6) | (7) |
| 26 | 5.2 | – | 2.3 | – | – | FRI ^{OS} | 629 | 6.9 | 6.9 | 1.5 | 3.7 | 169 | FRI/FRII |
| 33 | 4.6 | 3.2 | 1.7 | 1.7 | 172 | FRI/FRII | 739 | 2.1 | 2.1 | 1.3 | 1.3 | 180 | FRII? |
| 38 | 3.4 | 1.9 | 1.1 | 1.4 | 132 | FRI/FRII? | 743 | 3.9 | 3.1 | 2.5 | 2.1 | 157 | FRII |
| 44 | 20.5 | 2.0 | 11.4 | 1.3 | 170 | FRII | 746 | 6.9 | 4.3 | 2.5 | 2.5 | 141 | FRI/FRII |
| 64 | 2.2 | 1.2 | 1.2 | – | 180 | FRI/FRII? | 773 | 4.1 | 3.5 | 1.6 | 1.6 | 171 | FRI |
| 80 | 8.6 | 7.6 | 1.5 | 2.1 | 176 | FRI | 798 | 2.2 | 2.0 | 0.7 | 0.8 | 180 | FRI |
| 83 | 8.7 | 6.4 | 5.9 | 6.4 | 113 | FRII | 840 | 8.5 | 8.3 | 1.9 | 7.3 | 164 | FRI/FRII |
| 89 | 2.5 | 2.2 | 1.5 | 1.3 | 174 | FRII | 936 | 3.2 | 3.1 | 1.8 | 1.9 | 174 | FRII |
| 112 | 5.7 | 4.5 | 1.5 | 1.8 | 104 | FRI | 942 | 4.8 | 4.5 | 2.1 | 2.7 | 104 | FRI/FRII |
| 115 | 5.2 | 4.6 | 2.7 | 2.2 | 164 | FRI/FRII | 976 | 4.9 | – | – | – | – | FRI ^{OS} |
| 123 | 5.8 | 3.5 | 1.6 | 1.4 | 89 | FRI | 1031 | 2.9 | 2.4 | 1.3 | 1.3 | 108 | FRI/FRII |
| 137 | 4.8 | 4.3 | 2.6 | 3.1 | 170 | FRII | 1290 | 2.3 | 2.0 | – | – | 180 | FRI |
| 138 | 8.7 | 7.3 | 6.2 | 5.1 | 180 | FRII | 1411 | 1.9 | 1.5 | 0.9 | 0.8 | 169 | FRI/FRII? |
| 145 | 10.4 | 10.2 | 6.8 | 7.6 | 111 | FRII | 2251 | 4.8 | – | – | – | – | FRI ^{OS} |
| 153 | 3.1 | 0.9 | 2.6 | – | – | FRI/FRII | 2399 | 2.4 | 2.2 | 1.2 | 1.4 | 180 | FRII |
| 160 | 3.5 | 3.5 | 2.3 | 2.0 | 180 | FRII | 2516 | 3.2 | 3.0 | 0.7 | 1.6 | 170 | FRI/FRII? |
| 164 | 2.6 | 2.0 | – | – | 109 | FRI? | 2660 | 2.4 | 2.0 | 1.4 | 1.2 | 175 | FRII |
| 166 | 2.6 | 1.8 | 1.7 | 1.0 | 130 | FRII | 3065 | 3.9 | 1.6 | – | – | – | FRI |
| 177 | 11.8 | 11.6 | 8.4 | 5.4 | 133 | FRI/FRII | 3112 | 1.7 | 0.9 | 1.3 | 0.7 | 165 | FRII? |
| 187 | 6.4 | 6.2 | 1.1 | 1.2 | 156 | FRI | 3528 | 2.0 | 1.4 | 1.4 | 0.7 | 166 | FRI/FRII |
| 195 | 2.5 | 1.2 | 1.7 | – | – | FRI/FRII | 3866 | 2.3 | 1.4 | 1.7 | 1.4 | 176 | FRII? |
| 208 | 3.2 | 2.7 | 1.8 | 0.8 | 174 | FRI/FRII | 7087 | 1.9 | 1.4 | 1.8 | 1.2 | 143 | FRII? |
| 213 | 2.0 | 1.9 | 0.8 | 0.9 | 180 | FRI? | 10900 | 17.5 | 13.0 | 17.3 | 16.0 | 96 | FRII |
| 233 | 4.5 | 3.4 | 1.8 | 1.9 | 180 | FRI/FRII? | 10901 | 53.6 | 51.9 | 43.2 | 39.0 | 176 | FRII |
| 236 | 2.6 | 1.2 | – | – | – | FRI? | 10902 | 40.0 | 38.5 | 36.9 | 35.3 | 170 | FRII |
| 237 | 5.9 | – | 3.2 | – | – | FRI/FRII ^{OS} | 10903 | 9.0 | 8.1 | 3.6 | 2.2 | 123 | FRI |
| 247 | 14.2 | 5.8 | 3.8 | 2.7 | 160 | FRI | 10904 | 27.9 | 21.7 | 19.4 | 10.0 | 177 | FRI/FRII |
| 248 | 4.3 | 4.1 | 3.2 | 2.3 | 178 | FRII | 10905 | 25.5 | 24.0 | 17.4 | 16.8 | 175 | FRII |
| 280 | 2.0 | 1.7 | – | – | 180 | FRI? | 10906 | 9.9 | 9.0 | 6.0 | 4.7 | 94 | FRII |
| 299 | 8.1 | 6.5 | 7.1 | 4.3 | 139 | FRII | 10907 | 6.6 | 4.2 | 5.6 | 3.9 | 148 | FRII |
| 307 | 1.9 | 0.8 | 1.2 | – | – | FRI/FRII? | 10908 | 5.9 | 4.9 | 5.4 | 3.8 | 179 | FRII |
| 311 | 2.4 | 2.2 | 1.7 | 1.0 | 175 | FRI/FRII | 10909 | 8.2 | 7.3 | 6.7 | 5.5 | 167 | FRII |
| 319 | 1.7 | 1.5 | 0.6 | 0.6 | 180 | FRI | 10910 | 26.6 | 24.0 | 17.2 | 2.0 | 113 | FRI/FRII |
| 327 | 4.7 | 3.6 | 3.8 | 2.0 | 160 | FRII | 10911 | 22.2 | 9.7 | 16.9 | 15.1 | 176 | FRII |
| 347 | 3.1 | 2.7 | – | – | 170 | FRI? | 10912 | 12.8 | 11.7 | – | – | – | FRI |
| 360 | 6.6 | 6.5 | 2.9 | 3.0 | 37 | FRI | 10913 | 66.5 | 62.6 | 30.8 | 23.3 | 109 | FRI |
| 386 | 3.8 | 1.2 | 1.3 | – | 140 | FRI | 10914 | 13.3 | 12.4 | 10.0 | 1.5 | 163 | FRI/FRII |
| 404 | 4.2 | 2.2 | 2.3 | – | 165 | FRI/FRII | 10915 | 5.5 | 4.0 | 3.9 | 2.0 | 158 | FRI/FRII |
| 433 | 8.3 | 6.4 | 2.6 | 2.6 | 180 | FRI | 10916 | 29.5 | 25.5 | 20.5 | 19.0 | 175 | FRII |
| 437 | 5.0 | 4.6 | 2.2 | 2.0 | 173 | FRI | 10917 | 4.5 | 1.6 | 4.0 | 3.5 | 166 | FRII |
| 503 | 3.4 | 0.8 | 2.3 | – | – | FRI/FRII | 10918 | 42.8 | 14.4 | 29.5 | 10.1 | 139 | FRII |
| 516 | 2.6 | 1.8 | – | – | 173 | FRI? | 10919 | 15.7 | 14.7 | 12.1 | 10.5 | 179 | FRII |
| 560 | 2.8 | 1.5 | 1.8 | – | 130 | FRI/FRII | 10920 | 9.4 | 8.4 | 9.1 | 4.8 | 169 | FRII |
| 566 | 3.0 | 0.9 | 2.3 | – | – | FRI/FRII? | 10921 | 13.1 | 11.0 | 9.6 | 2.2 | 168 | FRI/FRII |
| 584 | 4.1 | 2.3 | 1.5 | – | 167 | FRI | 10922 | 14.3 | 9.5 | 11.3 | 8.8 | 179 | FRII |
| 613 | 3.2 | 2.8 | 2.5 | 2.3 | 161 | FRII | 10923 | 42.2 | 40.8 | 28.8 | 23.2 | 166 | FRII |
| 619 | 3.1 | 1.0 | 1.5 | – | – | FRI | 10924 | 20.9 | – | 14.7 | – | – | FRI/FRII ^{OS} |
| | | | | | | | 10925 | 31.1 | 28.4 | 27.5 | 25.6 | 173 | FRII |
| | | | | | | | 10926 | 4.4 | 3.0 | 2.2 | 1.0 | 152 | FRI |
| | | | | | | | 10927 | 20.1 | 19.0 | – | – | – | FRI |
| | | | | | | | 10928 | 24.5 | 20.5 | 14.5 | 11.2 | 179 | FRII |
| | | | | | | | 10929 | 10.9 | 10.1 | – | – | – | FRI |
| | | | | | | | 10930 | 6.3 | 2.7 | 4.8 | 3.3 | 169 | FRII |
| | | | | | | | 10931 | 13.0 | 7.1 | 11.3 | 8.1 | 111 | FRII |
| | | | | | | | 10932 | 4.8 | 3.8 | 2.4 | 1.8 | 164 | FRI |
| | | | | | | | 10933 | 20.8 | 2.1 | 16.7 | 5.3 | 162 | FRII |
| | | | | | | | 10934 | 6.8 | 1.7 | 5.3 | 2.5 | 175 | FRII |
| | | | | | | | 10935 | 16.9 | 13.0 | 12.2 | 8.8 | 167 | FRII |

Notes. Results from by-hand measurements of jet/lobe sizes to classify objects based on the FR classification scheme. **Column 1:** 3 GHz ID; **Column 2:** DL is the length of the larger side from the core to the 3σ contour, or the maximum length of the jet/lobe. **Column 3:** DS is the length of the shorter side from the core to the 3σ contour, or the minimum length of the jet/lobe. **Column 4:** DL_{hs} is the length of the larger side from the core to the brightest hot-spot of the jet/lobe. **Column 5:** DS_{hs} is the length of the shorter side from the core to the brightest hot-spot of the jet/lobe. **Column 6:** BA is the bent angle in degrees, which is the angle the jets/lobes form in respect to each other (180° for symmetrical objects). **Column 7:** FR class based on the previous measurements: FRI if $DL_{hs} < 0.5 \times DL$ and $DS_{hs} < 0.5 \times DS$ (edge-darkened); FRII if $DL_{hs} > 0.5 \times DL$ and $DS_{hs} > 0.5 \times DS$ (edge-brightened); FRI/FRII if one side is FRI-type and the other FRII-type; 'OS' denotes one-sided object; a '?' denotes uncertainty in the visual inspection.

Table A.1: Results of parametric FR classification (continued)

| 3 GHz | DL | DS | DL_hs | DS_hs | BA | FR |
|-------|----------|------|-------|-------|-----|-------------------|
| ID | (arcsec) | | | (deg) | | class |
| (1) | (2) | (3) | (4) | (5) | (6) | (7) |
| 10936 | 35.7 | 32.0 | 21.8 | 1.4 | 177 | FRI/FRII |
| 10937 | 2.4 | 1.5 | 2.2 | 1.3 | 170 | FRII |
| 10938 | 3.1 | 2.4 | 1.9 | 1.4 | 163 | FRII |
| 10939 | 4.8 | 3.6 | – | – | – | FRI |
| 10940 | 3.1 | 1.9 | 2.1 | 1.1 | 180 | FRII |
| 10941 | 3.9 | 2.8 | 1.7 | 0.7 | 167 | FRI |
| 10942 | 10.1 | 4.6 | 10.1 | 5.5 | 179 | FRII |
| 10943 | 4.3 | 3.6 | 3.4 | 2.4 | 171 | FRII |
| 10945 | 6.2 | – | 2.4 | – | – | FRI ^{OS} |
| 10947 | 3.9 | 3.2 | 3.2 | 2.5 | 165 | FRII |
| 10948 | 24.6 | 0.7 | 24.3 | 0.7 | 179 | FRII |
| 10949 | 15.7 | 1.1 | 9.3 | 0.7 | 153 | FRII |
| 10950 | 7.0 | 0.7 | 5.6 | 3.1 | 102 | FRII |
| 10951 | 10.7 | 2.5 | 6.2 | 5.0 | 175 | FRII |
| 10952 | 10.5 | 8.5 | 9.9 | 4.4 | 167 | FRII |
| 10953 | 17.6 | 2.0 | 12.6 | 3.5 | 166 | FRII |
| 10955 | 7.7 | 0.8 | – | – | – | FRI |
| 10956 | 55.7 | 1.4 | 39.5 | 1.9 | 57 | FRII |
| 10957 | 16.3 | – | 6.3 | – | – | FRI ^{OS} |
| 10958 | 15.0 | 1.4 | 4.9 | 1.0 | 101 | FRI/FRII |
| 10959 | 25.8 | 22.8 | 23.9 | 21.1 | 173 | FRII |
| 10962 | 8.8 | 7.5 | 8.6 | 6.2 | 175 | FRII |
| 10963 | 3.0 | 1.6 | – | – | – | FRI? |
| 10964 | 3.3 | 1.7 | – | – | – | FRI? |
| 10966 | 7.3 | 5.4 | 7.3 | 4.6 | 155 | FRII |

153: Possible one-sided FRI source. The north radio blob might be associated with the underlying galaxy. The VLA radio classification (Eva Schinnerer priv. comm.) give a FRII, which we believe is a mis-classification.

160: A double radio source, and in particular a fat-double which is thus classified as a FRI.

164: Although the 1.4 GHz map shows a shapeless radio source, the 3 GHz map reveals a small bent radio source, which we classify as an FRI.

166: We classify it as FRI cause of the twin-jet appearance at 3 GHz perpendicular to the host galaxy.

177: A twin-jet FRI source with a bent at the south suggesting interaction with the environment.

187: A fat-double FRI radio source with a slightly refined radio structure at 3 GHz than at 1.4 GHz.

195: A possible FRI due to the jet-like feature on the north-west.

208: A fat-double FRI from the 3 GHz map.

213: The 3 GHz map reveals a fat-double structure thus we classify it as FRI.

233: Elongated radio structure, possible FRI.

236: We classify this object as FRI cause at 3 GHz the structure resembles a fat-double radio source.

237: One-sided jet-like feature extending from the core. We classify it as FRI.

247: A clear twin-jet FRI, where one jet appears longer than the other probably due to orientation effect.

248: This radio source is outside the coverage of the VLA-COSMOS survey and the Ultra-VISTA coverage, thus we have no information on the host galaxy. It resembles a fat double and we classify it as FRI.

280: Elongated radio structure at 3 GHz, classified as an FRI.

299: A WAT source.

307: A double radio source, with one of the components centred

on the host galaxy. Classified as possible FRI.

311: This object resembles a twin-jet FRI radio source.

319: Looks like a young fat double FRI in the 3 GHz map.

327: A fat double FRI radio source revealed in detail at 3 GHz.
347: This source is not observed at 1.4 GHz nor with Ultra-VISTA, thus we don't have information on the host. We classify it as a possible FRII due to the double structure.

360: This fat double FRI source shown interaction with the environment at the end of it's jets, which is particularly highlighted in the 3 GHz map.

386: A hint of one-sided jet to the east. We classify it as possible FRI.

404: This source displays a one-sided jet at the 3 GHz map, although there is no equivalent structure at the 1.4 GHz map. We classify it as FRI.

433: A beautiful twin-jet FRI with very symmetric jets at 3 GHz. The 1.4 GHz map shows diffuse emission around the jets.

437: A fat double radio source. We classify it as FRI.

503: The 3 GHz map reveals a one-sided jet to the south-east. We classify it as FRI.

516: This source shows small jets perpendicular to the host galaxy. We classify it as FRI.

560: Classified as a possible FRI/FRII.

566: Both the 1.4 and 3 GHz maps show a jet-like structure towards the south-west. We classify it as a possible FRI, unless it is related to star formation in the near-by galaxy. With our current resolution is hard to distinguish.

584: A small twin-jet FRI with evident the orientation effects, as the south-east jet is more elongated. The 1.4 GHz map show not signs of jet.

613: **619:** One-sided jet towards the south-east. We classify it as FRI. The blob on the north-west might not be associated with it, and it's too diffuse to be certain, plus it is not seen at the lowest resolution 1.4 GHz map.

629: A very clear twin-jet FRI.

739: A small and diffuse twin-jet FRI.

743: A fat-double FRI with prominent core at 3 GHz. The core is not revealed at 1.4 GHz.

746: A bent twin-jet FRI (WAT) with orientation effects evident, as the south-east jet is larger than the north-west. The bent radio structure suggests interaction with the environment.

773: A small bent S-shaped FRI.

798: The 3 GHz map reveals a fat-double FRI, not evident at 1.4 GHz.

840: A twin-jet FRI with slightly bent radio structure suggesting interaction with the environment.

936: A twin-jet FRI is revealed in the 3 GHz map.

942: The 3 GHz map with it's high detail reveals a fat-double FRI radio source. If the galaxy at the north of the host emits synchrotron, this can contribute to the emission from the north lobe-like structure of the AGN and alter it's observed shape. Alternatively, the structure we are seeing might be due to orientation effects. A higher resolution map could help clear this situation and disentangle the emission from the AGN and the near-by galaxy.

976: This object has no host. We classify it as one-sided FRI.

1031: A possible FRII due to the prominent lobes, observed only at 3 GHz as it lies outside the 1.4 GHz survey coverage.

1290: The 3 GHz map reveals a twin-jet FRI.

1411: The 3 GHz map shows a double structure that resembles a fat-double FRI.

2251: We classify it as one-sided FRI.

2399: Small bent twin jets are seen in the 3 GHz map. We classify it as FRI. The object is not observed at 1.4 GHz as it

falls outside the survey coverage.

2516: 3 GHz map shows 2 radio components associated with the same optical/infrared counterpart; the core plus jet that are not detached and a detached lobe. The VLA structure differs in the sense the source is larger and resembles an FRI/FRII source with the SW lobe still attached.

2660: The 1.4 and 3 GHz radio shapes are significantly different, with the latter revealing a fat-double FRI which is not seen at 1.4 GHz.

JLVA 3065: The 3 GHz map reveals a one-sided radio jet. We classify it as FRI.

3112: In the 3 GHz map we see a fat-double radio structure. We classify the object as FRI.

3528: We classify this object as FRI due to the fat-double radio structure.

3866: We classify it as FRI at 3 GHz due to the fat-double radio structure.

7087: This object is not observed at 1.4 GHz as it lies outside the survey coverage. At 3 GHz it resembles a fat-double FRI with a slight bent.

10900: A bent FRII-type radio source, suggesting interaction with the environment. Emission at the east radio lobe is diffuse which is more pronounced at 3 GHz.

10901: A symmetric FRII radio source with a prominent core.

10902: A symmetric FRII radio source, where we can also see the core.

10903: Possible FRII radio source.

10904: FRII radio source with projection effect on the south lobe.

10905: Core and one-sided radio lobe.

10906: At 1.4 GHz this is a fat-double FRI. At 3 GHz we classify it as FRII due to the separation of the components, and we also note the projection effect on the east lobe.

10907: Possible FRII radio source due to the separation of the east lobe.

10908: This object lies outside the VLA-COSMOS coverage and was not observed at 1.4 GHz. Furthermore there is no Ultra-VISTA coverage. The 3 GHz map reveals a FRII radio source.

10909: A bent FRII radio source, probably a restarted source with a rotation in the projection of the lobes. The old AGN episode possibly gave the north-south lobes, and the new episode gives the north-west/south-east jet-like structures.

10910: This is probably a relic FRII radio source with the south jet-lobe structure being stretched and bent due to interaction with the environment. The 1.4 GHz map reveals intense diffuse emission within the area covered by the source.

10911: FRII radio source with the south lobe being rather diffuse.

10912: One-sided lobe to the west of the core. We classify it as FRII. There is no other lobe evident in either of the maps. The small radio source at south-west is associated to a nearby galaxy.

10913: The largest radio source in the sample in angular projected size, showing strong interaction with the environment. At 3 GHz the high resolution reveals the jet structure which is bent and the lobes dragged in the inter-galactic medium. We classify it as FRII. The one-sided radio source on the north-east, a NAT, is associated with another host, object 44 in our sample.

10914: We classify this source as FRII. The peculiar radio structure is due to either projection effect or interaction with the environment.

10915: A FRII radio source with peculiar lobes. No core is revealed at 3 GHz.

10916: A symmetric FRII radio where we also see the core.

10917: This object, although it is one-sided it resembles a fat-double. Thus we classify this as FRI.

10918: A FRII with bent radio lobes, in particular in the south where the lobe is bent perpendicular to the jet suggesting strong interaction with the environment.

10919: A symmetric FRII radio source where we also see the core.

10920: A symmetric FRII radio source where the east radio lobe is fainter than the west one. The core can also be seen in both maps.

10921: A possible FRII due to the diffuse lobe-like structures at the east and west of the core.

10922: This object is not observed at 1.4 GHz cause it lies outside the coverage. It also lacks a Ultra-VISTA detection. From the 3 GHz map we classify it as FRII, where we also see the core emission.

10923: A symmetric FRII radio source with possible projection effect. The south-west lobe is joint with the jet from the core.

10924: This object is not observed at 1.4 GHz as it lies outside the survey coverage, not with the Ultra-VISTA. At 3 GHz we observe an arched one-sided structure composed of 3 radio components, with a jet/lobe-like structure being the largest one. The radio position is marked at the brightest of the components. We classify it as possible FRII.

10925: A symmetric FRII radio source with core emission observed at both maps.

10926: The 1.4 GHz map shows a fat-double FRI, while the 3 GHz map reveals a FRII radio source.

10927: We classify this as FRI.

10928: FRII radio source with projection effect causing the lobes to have different structures.

10929: At both maps we see a one-sided lobe north-east of the core. We thus classify it as FRII. There is no sign for another lobe on either of the maps.

10930: A fat-double radio source classified as FRI.

10931: Diffuse radio source and interaction with the environment in this WAT radio source. We classify it as FRI.

10932: This source has not been observed at 1.4 GHz as it lies outside the coverage of the survey, and there is no Ultra-VISTA map either. It shows a possible FRII structure with core and two lobes on opposite directions.

10933: We classify this source as FRI as it resembles a fat-double object and the lobe-like structures are closer to the core than the edges of the source. Furthermore we note that the 3 GHz map reveals some type of rotation in the emission that could be a projection effect, or a restarted AGN.

10934: This object was classified as FRII by Schinnerer et al., but we believe it resembles a fat-double radio structure more so we classify it as FRI at 1.4 GHz. At 3 GHz the outer lobe-like structures get disattached from the rest of the body of the radio source forcing us to classify it as FRII.

10935: FRII radio source at both 1.4 and 3 GHz, where the core is also observed.

10936: FRII radio source with projection effect causing the different shape of the lobes.

10937: This source is classified as FRI at 1.4 GHz cause it resembles a fat-double. At 3 GHz due to the higher resolution the lobes are separated, thus we classify it as FRII. The core is not observed. This is the smallest FRII in our sample.

10938: This object has not been observed at 1.4 GHz as it lies outside the coverage of the survey, and there is no Ultra-VISTA map either. The 3 GHz map shows a FRII structure. We classify it as possible FRII due to lack of information regarding the host.

10939: A peculiar one-sided radio structure, detached at 3 GHz from the core. We classify it as possible FR II.

10940: We classify it as FR II.

10941: We classify this as FRI.

10942: We classify it as FR II.

10943: We classify it as one-sided FRI. The source at north-east is probably associated with the nearby galaxy.

10945: One-sided jet-like structure at 1.4 GHz, being refined as one-sided lobe structure at 3 GHz east of the core. There is no evidence for another lobe. We classify it as FR II.

10947: At 1.4 GHz we have a FRI source, while at 3 GHz the source is composed of two radio components. We classify it as a possible FR II.

10948: Diffuse radio jets. We classify it as FR II.

10949: A bent WAT FRI radio source suggesting interaction with the environment.

10950: The object is not observed at 1.4 GHz as it lies outside the survey coverage. It is a bent FRI radio source, otherwise a WAT. A small source with evident the effects of interaction with the environment.

10951: Jet-like structures on opposite sides of the core, nevertheless they are very diffuse. We classify it as FRI at 3 GHz.

10952: A bent twin-jet FRI, or a WAT radio source. The north jet looks more diffuse at 3 GHz. The bent radio structure suggests interaction with the environment.

10953: A twin-jet FRI with slight bent at the jet pointing towards the south-east.

10955: One-sided lobe-like structure at 3 GHz with a bent towards the south. We classify it as possible FR II.

10956: A most pronounced WAT FRI radio source of the sample, suggesting strong interaction with the environment. The 3 GHz map shows in detail the substructure along the jet.

10957: One-sided jet-like structure at 3 GHz, while the 1.4 GHz map reveals diffuse emission around the jet. We classify it as FRI.

10958: A bent twin-jet radio source, with diffuse emission towards the north-east jet. We classify it as FRI.

10959: FR II radio source with visible core.

10962: This source resembles a fat-double radio source with rather peculiar structure at 3 GHz. We classify it as FRI.

10963: We classify it as possible FRI.

10964: A double-like source at 3 GHz. The 1.4 GHz map it very different. We classify it as FRI.

10966: We classify this as FR II since it is edge-brightened. There seems to be some interaction with the environment towards the end of the jet-lobe structure. Alternatively we would classify this source as a hybrid FRI/FR II source as the north-west jet-lobe resembles an FR II while the south-east structure resembles a bent FRI-type jet. It is a jet-bent source like 360.

Appendix C: An approach for automatically measuring the Largest Angular Size (LAS) in VLA-COSMOS extended radio sources

In the following lines we describe a Python script¹⁵ for automatically measuring the Largest Angular Size (LAS) of extended radio sources identified in the VLA-COSMOS map at 3 GHz in the COSMOS field. Thus, it aims to overcome very time consuming routines to determine the LAS “by hand”. There are two main issues when trying to do so; first, a large diversity

¹⁵ Script developed by Eric F. Jiménez-Andrade.

of complex morphologies together with large contamination of point like sources – both real and spurious. Second, extended sources which split up into multi-components which are difficult to associate. To overcome those issues we propose to use advance image analysis algorithms in Python, namely: “scikit-image skeleton”¹⁶ and “scikit-learn mean shift cluster”¹⁷. In brief, the code works as follows.

I) Input, VLA-COSMOS cutout

We feed the script with a 160×160 arcsec² cutout from the VLA-COSMOS COSMOS 3 GHz map centred at the position of the radio source (as reported in the VLA-COSMOS COSMOS 3 GHz catalog). The cutout size is chosen according to the largest source in the sample, previously identified by eye

II) Binary image

We set up a threshold (N_{σ}) to identify “islands” of radio emission in the 160×160 arcsec² cutout. We are using a conservative value of 5σ . The result is a binary image with pixel values equal 1 if the rms $> 5\sigma$ and 0 if rms $< 5\sigma$

III) Skeletonization

The “natural” step would be to associate these islands into sources, i.e. to explore clustering algorithms. Nevertheless, since we aim to associate extended radio emission into single sources we should first get rid of contaminant compact/point-like sources in the field. Also, it should be noted that the main goal of the script is to determine the LAS of extended radio sources and, eventually, determine their FR class¹⁸ – in the case of radio galaxies. Therefore, we also need to disentangle the pixels which belong to each lobe and, subsequently, determine the distance from the centre to the brightest (d_b) and farthest pixel (d_f); which will allow to apply the original FR classification scheme (FR II if $d_b/d_f > 0.5$ and FRI if $d_b/d_f < 0.5$?)⁷⁴. The later task might be relatively simple for symmetric radio galaxies, however, the vast majority are asymmetric and complex extended radio galaxies. Thus, we need a comprehensive but simplistic representation of the source’s shape.

We propose to use “Skeletonization algorithms” to reduce binary objects to 1 pixel wide representations. Skeletonization is a process for reducing foreground regions in a binary image to a skeletal remnant, i.e. skeleton, that largely preserves the extent and connectivity of the original region while throwing away most of the original foreground pixels. This procedure allow us to measure the length length of a shape by considering just the end points of the skeleton and finding the maximally separated pair of end points on the skeleton.

Scikit-image, an image processing toolbox for SciPy, offers a module on “Skeletonization algorithms” which is suitable for our particular purpose. We are using the module “Medial axis skeletonization” to derive the skeleton/medial-axis of islands of emission above the 5σ level (see Fig. C.1). The result is an array of vectors containing information only on the pixels from the skeleton. Each vector is of the form: $skel = [rad, dec, r_{skel}, flux]$; where ra and dec are the coordinates, r_{skel} is the distance from the skeleton to the boundaries (i.e. the local half-width of the island) and $flux$ is the flux density corresponding to the each pixel in the skeleton (see Fig. C.1, bottom panel).

¹⁶ <http://scikit-image.org/docs/dev/api/skimage.morphology.html>

¹⁷ <http://scikit-learn.org/stable/modules/generated/sklearn.cluster.MeanShift.html>

¹⁸ Not presented here.

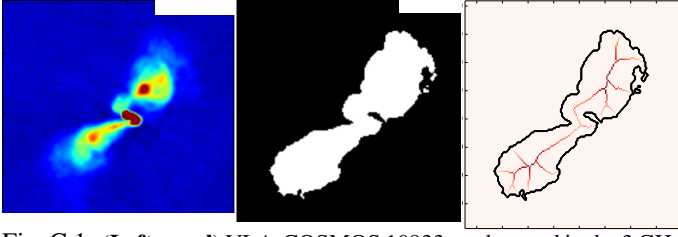


Fig. C.1: **(Left panel)** VLA-COSMOS 10933 as observed in the 3 GHz VLA-COSMOS radio map. **(Middle panel)** Binary image obtained after setting a threshold of 5σ . **(Right panel)** Its skeleton (given by the distance transform) is shown in red.

IV) Removing compact sources

Based on the parameter r_{skel} we can identify those islands of emission which are resolved, i.e. islands for which its width is larger than the synthesised beam of 0.75 arcsec; given the pixel scale of 0.2 arcsec/pixel this translates into 3.75 pixels. In order to do so, we leave r_{skel} as an input parameter, as it depends on the synthesised beam and pixel scale. In the case of the 3 GHz VLA-COSMOS map we set $r_{skel} = 2$, which yields a local width of 4 pixels given that resolved sources will have a local width above 3.75 pixels.

This allows to get rid of all the unresolved sources, however, we still have to deal with point-like sources which are resolved, i.e. for which $r_{skel} > 2$. At this stage, we are taking the position of all the 3 GHz VLA-COSMOS sources (as specified in the public catalog) as a prior. We identify all these sources within the original cutout of 160×160 arcsec and discard all the pixels in their skeleton – within a given aperture – for further analyses (e.g. clustering). We leave the radius for this aperture ($r_{resolved}$) as an input parameter. In this case, to assure that all the pixels from the skeleton of resolved point-like sources are removed from the field, we chose a radius of 10 pixels, or ~ 2.5 arcsec (~ 3 times the synthesised beam).

V) Clustering, mean-shift algorithm The next question is which islands within the cutout belong to the same radio source. This is particularly important when dealing with crowded fields and multiple sources, which can also be extended. Nowadays there are different clustering algorithms on 2D datasets, however, most of them rely on the number of clusters to find as an input. On the other hand, the so-called mean shift algorithm (Fukunaga & Hostetler, 1975; Cheng, 1995) is a nonparametric clustering technique which does not require prior knowledge of the number of clusters, and does not constrain the shape of the clusters, which is very convenient for our goal.

Mean shift clustering is a centroid based algorithm, which works by updating candidates for centroids to be the mean of the points within a given region. These candidates are then filtered in a post-processing stage to eliminate near-duplicates to form the final set of centroids. The algorithm automatically sets the number of clusters. However, it relies on a parameter bandwidth, which dictates the size of the region to search through. Depending on the used bandwidth the clustering will be different. Then, large values for the bandwidth tend to find a small amount of cluster and vice versa (see a nice description of the physical meaning of the kernel bandwidth in [Matt Nedrich's blog](https://spin.atomicobject.com/2015/05/26/mean-shift-clustering/)¹⁹). In other words, very extended radio sources (e.g. $LAS \sim 1$ arcmin) would need high values in order to pack all the emission into

only one single source; on the contrary, small values for the bandwidth will suffice to group relatively compact emission (e.g. $LAS \sim 3$ arcsec) into one source (see Fig. C.2).

For simplicity reasons we are using a small sample to optimise the bandwidth, which allows to recover the highest percentage of successful fits. We select a representative sub-sample (~ 10 sources) which comprises sources with different angular size. It should be noted that varying the bandwidth value (which goes from 0 to 1) does not strongly affect the final results as the unsuccessful fits usually occur with extreme sources (very extended or compact, see Fig. C.2) which represents less than 20% of the sample. We found that a bandwidth of 0.9 yields a 90% of successful fits (this was verified by eye). We leave the bandwidth as an input parameter, in principle we should have a prior based on analytical/statistical predictions (see the “issues” paragraph below).

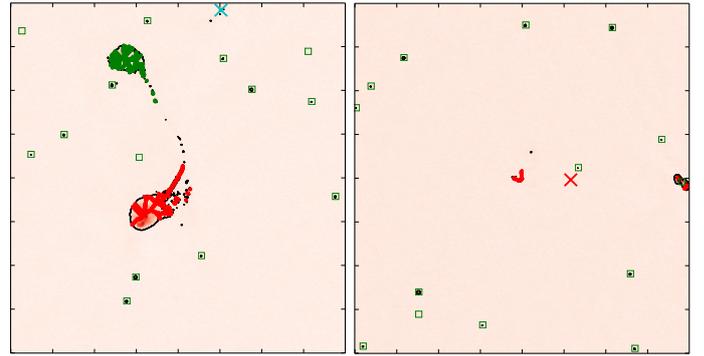


Fig. C.2: **(Left panel)** VLA-COSMOS 10913, with a $LAS \sim 1.5$ arcmin is one of the largest source in the sample. Consequently, the bandwidth should be large to recover a proper fit. When using an intermediate value of 0.5, the algorithm splits the source into two clusters (see red and green coloured pixels in the skeleton). **(Right panel)** On the contrary, in the case of VLA-COSMOS 10958 with $LAS \sim 5$ arcsec the bandwidth should be small. When using a high value of 0.9, the algorithm associate this source with another nearby extended (but unrelated) source in the field. Different colours represent the different groups/clusters identified by the algorithm. Squares show the position of the compact radio sources identified with BLOBCAT (Hales et al., 2012).

The result from the clustering algorithm is an array containing the coordinates of those pixel-members of the skeletons, of all the emission islands within the cutout, along with a label to identify the different clusters found in this step. To select those pixels associated with the source of interest we match the label from the nearest pixel to the central position of the cutout, which correspond to the position of the host galaxy given in the 3 GHz VLA-COSMOS source catalog.

VI) Maximising the angular size

After all the latter steps pixels in the skeletons of all the islands of emission, across the whole cutout, would have been grouped into single sources. Next, we find what is the maximum euclidean distance between two points which belong to the same source. We have to make a small correction to this distance, given that the end points of the skeleton are not the end points of the real source (at the 5σ level, see section III). We only need to add the width in pixels of the end points of the skeleton to get the final distance. We convert the LAS in pixels to arcsec and given the redshift and an assumed cosmology we can convert this to the Largest-projected Linear Size (LLS) of the source.

The information containing the LAS for all the sources is stored in an ASC II file, while the fits performed in the script (skelotonization, clustering, maximizing the distance between

¹⁹ <https://spin.atomicobject.com/2015/05/26/mean-shift-clustering/>

two points) are displayed in the interactive plotting interface of Python.

In Fig. C.3 we compare the LAS measured from the semi-automatic ML method (LAS_{ML}) and the parametrised method described in Appendix A (LAS_{visual}). The ML method overestimates LAS sizes for objects with nearby sources or at the edges of the 3 GHz mosaic where the noise level is higher, and underestimates LAS sizes for diffuse radio sources. Examples where the code is failing to provide an accurate LAS are marked with their name in Fig. C.3 and shown in Fig. C.4.

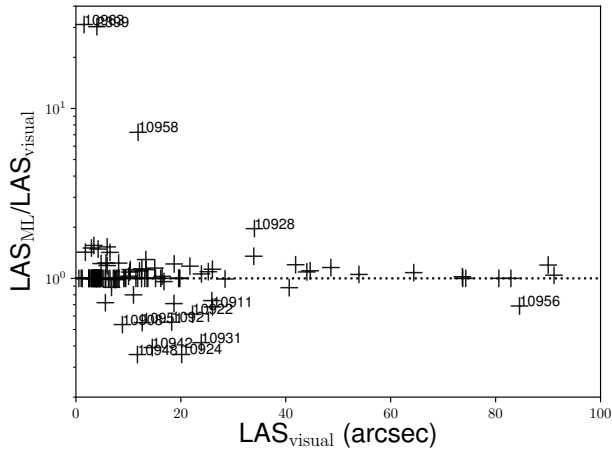


Fig. C.3: Comparison between LAS measured with the semi-automatic ML method described in Appendix C and the parametrised visual method described in Appendix A. The dotted horizontal line shows the one-to-one relation.

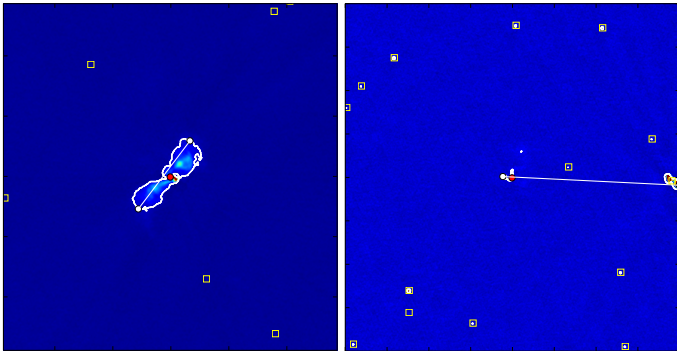


Fig. C.4: Examples of 3 GHz sources (10933 left, 10958 right) where the semi-automatic machine learning code is not providing a correct measurement of the largest angular size. The line indicates the LAS measurement.

Table C.1: Radio Properties

| 3 GHz ID | COSMOSVLA3 | R.A. (deg) | Dec. (deg) | $S_{3\text{GHz}}$ (mJy) | S_{err} (mJy) | z | radio class | radio excess | X-ray group ID | LAS (arcsec) | D (kpc) | 1.4GHz ID | |
|----------|---------------------|------------|------------|-------------------------|------------------------|--------------------|-------------|--------------|----------------|--------------|---------|-----------------|------|
| (1) | (2) | (3) | (4) | (5) | (6) | (7) | (8) | (9) | (10) | (11) | (12) | (13) | (14) |
| 26 | J100153.45+021152.5 | 150.47275 | 2.1979 | 2.769 | 0.139 | – | FRI | – | – | 4.43 | 0.0 | J100153+021152 | |
| 33 | J100131.14+022924.7 | 150.37978 | 2.4902 | 2.970 | 0.148 | 0.349 ^s | FRI/FRII | T | – | 4.68 | 23.1 | J100131+022924 | |
| 38 | J100326.62+020455.4 | 150.86095 | 2.0821 | 4.924 | 0.250 | – | FRI/FRII? | – | – | 4.34 | –0 | – | |
| 44 | J100026.49+024229.7 | 150.11040 | 2.7083 | 2.250 | 0.113 | 0.351 ^s | FRII | T | 237 | 13.54 | 67.0 | J100026+024229T | |
| 64 | J100159.82+023904.8 | 150.49928 | 2.6513 | 2.245 | 0.112 | 0.800 ^p | FRI/FRII? | T | – | 3.18 | 23.9 | J100159+023904 | |
| 80 | J095959.61+024608.9 | 149.99838 | 2.7691 | 3.021 | 0.151 | 0.166 ^s | FRI | T | – | 13.11 | 37.3 | J095959+024608T | |
| 83 | J095957.98+021809.7 | 149.99159 | 2.3027 | 3.554 | 0.178 | 1.698 ^p | FRII | T | – | 12.51 | 105.9 | J095957+021809T | |
| 89 | J100109.28+021721.7 | 150.28871 | 2.2894 | 1.988 | 0.099 | 2.582 ^p | FRI | T | 264 | 4.61 | 36.9 | J100109+021721T | |
| 112 | J100304.56+024917.4 | 150.76901 | 2.8215 | 1.678 | 0.084 | 0.218 ^s | FRI | F | – | 4.62 | 16.3 | J100304+024917 | |
| 115 | J100329.18+025300.6 | 150.87160 | 2.8835 | 6.876 | 0.344 | – | FRI/FRII | – | – | 8.04 | 0.0 | – | |
| 123 | J100122.38+020111.8 | 150.34329 | 2.0200 | 8.009 | 0.400 | 0.425 ^s | FRI | F | – | 7.84 | 43.7 | – | |
| 137 | J100131.36+022639.1 | 150.38069 | 2.4442 | 9.024 | 0.451 | 0.348 ^s | FRII | T | – | 80.61 | 396.5 | J100131+022639T | |
| 138 | J095908.93+024813.0 | 149.78723 | 2.8036 | 13.975 | 0.699 | 1.114 ^s | FRII | T | – | 15.18 | 124.3 | J095908+024813T | |
| 145 | J100047.59+015911.5 | 150.19832 | 1.9865 | 10.064 | 0.503 | 0.438 ^s | FRII | – | – | 19.68 | 111.6 | – | |
| 153 | J100057.45+024216.9 | 150.23938 | 2.7047 | 0.627 | 0.031 | 1.514 ^p | FRI/FRII | T | – | 3.71 | 31.4 | J100057+024217T | |
| 160 | J100007.31+024049.8 | 150.03046 | 2.6805 | 2.211 | 0.111 | 1.169 ^p | FRI | T | – | 5.58 | 46.1 | J100007+024049T | |
| 164 | J100003.39+020723.0 | 150.01416 | 2.1231 | 1.085 | 0.054 | 0.675 ^s | FRI? | – | – | 4.00 | 28.2 | J100003+020723 | |
| 166 | J100124.08+021706.3 | 150.35036 | 2.2851 | 1.048 | 0.052 | 1.677 ^p | FRII | T | – | 4.36 | 36.9 | J100124+021706 | |
| 177 | J100058.05+015133.3 | 150.24190 | 1.8593 | 5.294 | 0.265 | 1.687 ^s | FRI/FRII | – | – | 19.81 | 167.7 | – | |
| 187 | J095946.30+023602.1 | 149.94295 | 2.6006 | 9.294 | 0.465 | 0.344 ^s | FRI | T | – | 9.50 | 46.4 | J095946+023602T | |
| 195 | J100002.88+013907.8 | 150.01204 | 1.6522 | 0.662 | 0.033 | 1.518 ^s | FRI/FRII | T | – | 3.49 | 29.6 | J100002+013907 | |
| 208 | J095846.38+021602.4 | 149.69327 | 2.2673 | 2.898 | 0.145 | 0.905 ^s | FRI/FRII | T | – | 5.19 | 40.5 | J095846+021602 | |
| 213 | J100112.28+014123.7 | 150.30116 | 1.6899 | 0.886 | 0.044 | 0.530 ^p | FRI? | T | 311 | 3.93 | 24.7 | J100112+014123 | |
| 233 | J100328.30+020650.4 | 150.86795 | 2.1140 | 3.392 | 0.170 | – | FRI/FRII? | – | – | 5.69 | 0.0 | – | |
| 236 | J095829.07+020531.1 | 149.62114 | 2.0920 | 0.805 | 0.040 | 1.203 ^p | FRI | T | – | 3.40 | 28.2 | J095829+020530 | |
| 237 | J100151.52+022532.3 | 150.46469 | 2.4256 | 0.620 | 0.031 | 0.827 ^s | FRI/FRII | F | – | 4.94 | 37.5 | – | |
| 247 | J095901.42+024742.4 | 149.75592 | 2.7951 | 3.516 | 0.176 | 0.490 ^s | FRI | – | 24 | 19.58 | 118.2 | – | |
| 248 | J100338.97+022622.9 | 150.91241 | 2.4397 | 13.837 | 0.692 | – | FRII | – | – | 7.34 | 0.0 | – | |
| 280 | J100218.31+022804.0 | 150.57631 | 2.4678 | 0.678 | 0.034 | 0.559 ^s | FRI? | T | – | 3.86 | 24.9 | J100218+022804 | |
| 299 | J095807.61+025501.5 | 149.53174 | 2.9171 | 7.043 | 0.352 | 2.15 ^p | FRII | – | – | 13.72 | 113.7 | – | |
| 307 | J100004.93+024628.6 | 150.02057 | 2.7746 | 0.593 | 0.030 | 2.091 ^s | FRI/FRII? | T | – | 82.91 | 690.4 | J100004+024628 | |
| 311 | J095818.40+013514.2 | 149.57671 | 1.5873 | 0.512 | 0.026 | 2.451 ^p | FRI/FRII | T | – | 4.44 | 36.0 | J095818+013514 | |
| 319 | J100015.46+025231.3 | 150.06445 | 2.8754 | 0.909 | 0.045 | 1.041 ^p | FRI | T | – | 3.20 | 25.8 | J100015+025231 | |
| 327 | J095958.79+013756.5 | 149.99496 | 1.6324 | 1.092 | 0.055 | 1.278 ^p | FRII | T | – | 7.64 | 63.9 | J095958+013756T | |
| 347 | J095751.96+024255.0 | 149.46651 | 2.7153 | 0.571 | 0.029 | 0.880 ^s | FRI? | T | – | 3.09 | 23.9 | J095751+024255 | |
| 360 | J100201.19+021327.1 | 150.50499 | 2.2242 | 2.959 | 0.148 | 0.836 ^s | FRI | – | – | 8.24 | 62.7 | J100201+021327T | |
| 386 | J100141.01+015903.6 | 150.42090 | 1.9843 | 0.412 | 0.021 | 0.322 ^s | FRI | – | – | 3.57 | 16.7 | – | |
| 404 | J095856.37+024546.7 | 149.73488 | 2.7630 | 0.336 | 0.017 | 0.754 ^p | FRI/FRII | T | – | 4.01 | 29.5 | J095856+024546 | |

Notes. Basic radio properties and radio classification for the FR objects in our sample. **Column 1 & 2:** The 3 GHz VLA-COSMOS ID (Smolčić et al., 2017a) and IAU name respectively. **Columns 3 & 4:** Right Ascension and Declination, respectively, of radio position. **Columns 5 & 6:** Integrated flux density at 3 GHz, and corresponding error; for the multi-component sources the error corresponds to the 5% of the calibration error, while for the rest is the error given by blobcat . **Column 7:** Redshift and type ('s' for spectroscopic, 'p' for photometric) from Laigle et al. (2016). **Columns 8 & 9** Radio classification performed by visual inspection of the VLA-COSMOS at 3 GHz, as described in Sec. A, and VLA radio classification at 1.4 GHz given by Schinnerer et al. (2010). **Column 10** gives the radio excess as in Delvecchio et al. (2017): 'T' for radio excess object, i.e. radio AGN, 'F' for non-radio excess. **Column 11** X-ray group ID (groups from George et al., 2011). **Column 12:** Largest angular size, projected, in arcsec, measured by a semi-automatic technique and verified by eye (see Sec. C). **Column 13:** linear-projected size in kpc, calculated using z and LAS. **Column 14:** VLA 1.4 GHz ID from Schinnerer et al. (2010).

Table C.1: Radio Properties (Continued)

| 3 GHz ID | COSMOSVLA3 (2) | R.A. (deg) (3) | Dec. (deg) (4) | $S_{3\text{GHz}}$ (mJy) (5) | S_{err} (mJy) (6) | z (7) | radio class 3GHz (8) | radio class 1.4GHz (9) | radio excess (10) | X-ray group ID (11) | LAS (arcsec) (12) | D (kpc) (13) | 1.4GHz ID COSMOSVLA3 (14) |
|----------|---------------------|----------------|----------------|-----------------------------|----------------------------|--------------------|----------------------|------------------------|-------------------|---------------------|-------------------|--------------|---------------------------|
| 433 | J095901.79+025336.2 | 149.75746 | 2.8934 | 1.146 | 0.057 | 0.351 ^s | FRI | – | F | – | 11.77 | 58.3 | – |
| 437 | J095823.24+020859.5 | 149.59685 | 2.1499 | 2.403 | 0.120 | 0.283 ^s | FRI | FRI | T | – | 9.34 | 40.0 | J095823+020859T |
| 503 | J100243.23+015511.2 | 150.68015 | 1.9198 | 0.242 | 0.012 | 1.292 ^s | FRI/FRII | FRII | T | – | 3.75 | 31.4 | J100243+015511T |
| 516 | J100144.47+021346.0 | 150.43533 | 2.2295 | 0.249 | 0.013 | 1.142 ^s | FRI? | – | T | – | 2.96 | 24.4 | J100144+021346 |
| 560 | J100256.09+021552.6 | 150.73375 | 2.2646 | 0.198 | 0.010 | 1.176 ^p | FRI/FRII? | – | T | – | 2.49 | 20.6 | J100256+021552 |
| 566 | J100025.21+024328.4 | 150.10507 | 2.7246 | 0.237 | 0.012 | 0.729 ^s | FRI/FRII? | – | T | – | 74.30 | 539.5 | J100025+024328 |
| 584 | J095835.90+024954.7 | 149.64963 | 2.8319 | 0.307 | 0.016 | 0.705 ^s | FRI | – | T | – | 3.52 | 25.2 | J095835+024955 |
| 613 | J100101.33+022159.3 | 150.25557 | 2.3665 | 0.344 | 0.017 | 2.910 ^s | FRII | – | – | – | 4.80 | 37.3 | – |
| 619 | J095951.42+023126.3 | 149.96426 | 2.5240 | 0.184 | 0.009 | 0.687 ^s | FRI | – | T | – | 3.37 | 23.9 | J095951+023126 |
| 629 | J095929.23+022844.9 | 149.87181 | 2.4791 | 0.580 | 0.029 | 0.735 ^s | FRI/FRII | FRII | T | – | 11.43 | 83.3 | J095929+022844T |
| 739 | J095914.66+021509.0 | 149.81111 | 2.2525 | 0.167 | 0.009 | 0.380 ^s | FRII? | – | T | 246 | 2.57 | 13.4 | J095914+021509 |
| 743 | J095932.82+013753.5 | 149.88676 | 1.6315 | 0.672 | 0.034 | 1.335 ^p | FRII | FRI | T | – | 6.49 | 54.5 | J095932+013753T |
| 746 | J095847.45+023408.9 | 149.69771 | 2.5691 | 0.528 | 0.026 | 0.941 ^s | FRI/FRII | – | F | – | 9.12 | 72.0 | – |
| 773 | J095815.49+014923.1 | 149.56454 | 1.8231 | 0.282 | 0.014 | 1.507 ^s | FRI | – | T | – | 3.99 | 33.8 | J095815+014923T |
| 798 | J100128.99+025243.7 | 150.37082 | 2.8788 | 0.469 | 0.024 | 0.821 ^p | FRI | – | T | – | 3.84 | 29.1 | J100128+025243 |
| 840 | J100147.49+015101.1 | 150.44791 | 1.8503 | 0.704 | 0.035 | 0.894 ^s | FRI/FRII | WAT | T | – | 16.16 | 125.7 | J100147+015101T |
| 936 | J095929.97+020345.3 | 149.87489 | 2.0626 | 0.252 | 0.013 | 0.847 ^s | FRII | FRII | T | – | 4.18 | 31.9 | J095929+020345T |
| 942 | J095947.05+024806.7 | 149.94608 | 2.8019 | 0.523 | 0.026 | 0.605 ^s | FRI/FRII | FRII | T | – | 7.13 | 47.9 | J095947+024806 |
| 976 | J095958.77+020715.0 | 149.99490 | 2.1208 | 0.523 | 0.026 | – | FRI | – | – | – | 73.73 | 0.0 | J095958+020714 |
| 1031 | J100245.96+025647.4 | 150.69151 | 2.9465 | 0.406 | 0.021 | – | FRI/FRII | – | – | – | 3.83 | 0.0 | – |
| 1290 | J095836.17+013919.0 | 149.65074 | 1.6553 | 0.152 | 0.008 | 0.790 ^p | FRI | – | T | – | 3.54 | 26.5 | J095836+013918 |
| 1411 | J100115.51+021720.0 | 150.31467 | 2.2889 | 0.225 | 0.012 | 1.200 ^p | FRI/FRII? | – | T | – | 2.92 | 24.2 | J100115+021719 |
| 2251 | J100304.62+020713.1 | 150.76927 | 2.1203 | 0.413 | 0.021 | – | FRI | – | – | 239 | 4.41 | – | 100103+023806 |
| 2399 | J095945.76+012806.4 | 149.94069 | 1.4684 | 0.472 | 0.027 | 1.805 ^p | FRII | – | F | – | 4.00 | 33.8 | – |
| 2516 | J100306.82+014518.6 | 150.77846 | 1.7552 | 0.160 | 0.009 | 0.966 ^p | FRI/FRII | – | – | 259 | 2.46 | 19.5 | J100306+014518 |
| 2660 | J095905.54+025144.7 | 149.77310 | 2.8624 | 0.142 | 0.008 | 0.901 ^p | FRII | – | T | – | 3.90 | 30.4 | – |
| 3065 | J095941.38+024504.7 | 149.92244 | 2.7513 | 0.075 | 0.005 | 2.467 ^p | FRI | – | – | – | 1.00 | 8.1 | J095941+024504 |
| 3112 | J100331.36+014605.2 | 150.88069 | 1.7681 | 0.217 | 0.012 | – | FRII? | – | – | – | 1.21 | 0.0 | – |
| 3528 | J100108.67+023022.6 | 150.28615 | 2.5063 | 0.080 | 0.005 | 2.217 ^p | FRI/FRII | – | F | – | 2.91 | 24.0 | J100108+023022 |
| 3866 | J095950.74+022058.2 | 149.96143 | 2.3495 | 0.107 | 0.006 | 0.940 ^s | FRII? | FRI | T | 145 | 2.50 | 19.7 | J095950+022058 |
| 7087 | J095718.98+021255.1 | 149.32912 | 2.2153 | 0.383 | 0.022 | – | FRII? | – | – | – | 0.57 | 0.0 | – |
| 10900 | J095908.31+024309.6 | 149.78467 | 2.7193 | 35.170 | 1.758 | 1.308 ^s | FRII | WAT | T | – | 28.42 | 238.3 | J095908+024309T |
| 10901 | J095758.04+015825.1 | 149.49184 | 1.9737 | 18.160 | 0.908 | 2.239 ^s | FRII | – | T | 37 | 91.13 | 751.2 | J095758+015825 |
| 10902 | J095823.31+022628.4 | 149.59712 | 2.4412 | 46.160 | 2.308 | 1.168 ^s | FRII | – | T | – | 73.67 | 608.4 | – |
| 10903 | J100208.75+024103.2 | 150.53647 | 2.6842 | 6.950 | 0.347 | 1.213 ^s | FRI | – | T | – | 10.35 | 86.0 | J100208+024103 |
| 10904 | J100243.20+015943.4 | 150.68028 | 1.9958 | 28.420 | 1.421 | 1.206 ^p | FRI/FRII | – | T | – | 33.90 | 281.3 | – |
| 10905 | J100229.89+023225.0 | 150.62456 | 2.5403 | 3.170 | 0.159 | 0.432 ^s | FRII | FRII | T | 379 | 23.92 | 134.6 | J100229+023225T |
| 10906 | J100212.06+023135.0 | 150.55051 | 2.5264 | 8.651 | 0.433 | 0.948 ^p | FRII | FRI | T | – | 13.37 | 105.7 | J100212+023134T |
| 10907 | J100309.43+022714.1 | 150.78931 | 2.4539 | 2.814 | 0.141 | 1.211 ^p | FRII | FRII | T | – | 8.14 | 67.6 | J100309+022714T |
| 10908 | J100339.13+015546.6 | 150.91350 | 1.9296 | 26.230 | 1.311 | 0.922 ^p | FRII | – | F | – | 8.86 | 69.5 | – |

Table C.1: Radio Properties (Continued)

| 3 GHz ID | COSMOSVLA3 (2) | R.A. (deg) (3) | Dec. (deg) (4) | $S_{3\text{GHz}}$ (mJy) (5) | S_{err} (mJy) (6) | z (7) | radio class 3GHz (8) | radio class 1.4GHz (9) | radio excess (10) | X-ray group ID (11) | LAS (arcsec) (12) | D (kpc) (13) | 1.4GHz ID COSMOSVLAADP (14) |
|----------|---------------------|----------------|----------------|-----------------------------|----------------------------|--------------------|----------------------|------------------------|-------------------|---------------------|-------------------|--------------|-----------------------------|
| 10909 | J100007.91+024315.3 | 150.03293 | 2.7209 | 6.828 | 0.341 | 1.438 ^p | FRII | FRI | T | — | 12.57 | 106.2 | J100007+024315T |
| 10910 | J100049.59+014923.7 | 150.20662 | 1.8233 | 5.867 | 0.293 | 0.530 ^s | FRI/FRII | WAT | T | — | 40.66 | 255.9 | J100049+014923T |
| 10911 | J100114.85+020208.6 | 150.31190 | 2.0357 | 3.425 | 0.171 | 0.971 ^s | FRII | FRII | T | — | 26.03 | 207.0 | J100114+020208T |
| 10912 | J095802.10+021540.8 | 149.50874 | 2.2613 | 1.220 | 0.061 | 0.943 ^s | FRI | — | T | — | 18.69 | 147.5 | J095802+021540 |
| 10913 | J100028.28+024103.3 | 150.11786 | 2.6843 | 32.090 | 1.605 | 0.349 ^s | FRI | FRI | T | — | 90.02 | 443.9 | J100028+024103T |
| 10914 | J100230.19+020913.2 | 150.62582 | 2.1537 | 3.327 | 0.166 | 1.437 ^p | FRI/FRII | — | T | — | 18.73 | 158.2 | — |
| 10915 | J095959.15+014837.7 | 149.99655 | 1.8105 | 3.692 | 0.185 | 2.357 ^p | FRI/FRII | FRII | T | — | 5.95 | 48.6 | J095959+014837T |
| 10916 | J100140.13+015129.6 | 150.41718 | 1.8583 | 5.438 | 0.272 | 0.459 ^s | FRII | FRI | T | — | 44.65 | 260.2 | J100140+015129T |
| 10917 | J100152.22+024535.3 | 150.46756 | 2.7598 | 1.523 | 0.076 | 1.446 ^p | FRII | — | T | — | 6.79 | 57.3 | J100152+024535 |
| 10918 | J095824.01+024916.1 | 149.60008 | 2.8212 | 25.220 | 1.261 | 0.345 ^s | FRII | FRI | T | — | 41.88 | 204.8 | J095824+024916T |
| 10919 | J100114.13+015444.1 | 150.30887 | 1.9123 | 3.157 | 0.158 | 1.483 ^p | FRII | FRI | T | — | 25.24 | 213.5 | J100114+015444T |
| 10920 | J095839.24+013557.7 | 149.66354 | 1.5994 | 1.975 | 0.099 | 1.668 ^p | FRII | FRI | T | — | 13.33 | 112.9 | J095839+013557T |
| 10921 | J095834.09+022703.3 | 149.64206 | 2.4509 | 0.981 | 0.049 | 1.319 ^p | FRI/FRII | FRII | T | — | 18.26 | 153.2 | J095834+022703T |
| 10922 | J100343.12+023700.2 | 150.92970 | 2.6168 | 24.150 | 1.208 | 1.597 ^p | FRII | — | T | — | 22.23 | 188.3 | — |
| 10923 | J100303.67+014735.9 | 150.76530 | 1.7933 | 13.170 | 0.659 | 1.203 ^p | FRII | FRI | T | — | 64.40 | 534.3 | J100303+014736T |
| 10924 | J095925.79+030100.5 | 149.85750 | 3.0168 | 9.353 | 0.468 | — | FRI/FRII | — | F | — | 20.16 | 0.0 | — |
| 10925 | J095741.10+015122.4 | 149.42126 | 1.8562 | 18.540 | 0.927 | 0.985 ^p | FRII | FRI | T | — | 53.95 | 430.5 | J095741+015122T |
| 10926 | J095949.83+015650.3 | 149.95770 | 1.9473 | 0.744 | 0.037 | 1.769 ^p | FRI | FRI | T | — | 4.23 | 35.7 | J095949+015650T |
| 10927 | J100101.98+020511.4 | 150.25827 | 2.0865 | 1.055 | 0.053 | 0.915 ^p | FRI | — | T | — | 18.81 | 147.2 | — |
| 10928 | J095822.49+024722.1 | 149.59373 | 2.7895 | 11.640 | 0.582 | 0.878 ^s | FRII | — | T | — | 34.03 | 263.2 | — |
| 10929 | J100211.45+015458.0 | 150.54771 | 1.9161 | 0.298 | 0.015 | 1.716 ^p | FRI | — | T | — | 10.25 | 86.8 | J100211+015458 |
| 10930 | J100231.43+015138.1 | 150.63098 | 1.8606 | 0.578 | 0.029 | 2.165 ^s | FRII | — | T | — | 6.50 | 53.9 | J100231+015138T |
| 10931 | J095828.65+014407.6 | 149.61937 | 1.7355 | 0.867 | 0.043 | 0.595 ^s | FRII | WAT | T | — | 23.90 | 159.1 | J095828+014407T |
| 10932 | J095945.81+025924.3 | 149.94090 | 2.9901 | 0.816 | 0.041 | 1.162 ^p | FRI | — | T | — | 5.74 | 47.4 | — |
| 10933 | J100043.19+014607.8 | 150.17995 | 1.7689 | 39.300 | 1.965 | 0.346 ^s | FRII | FRII | T | — | 26.02 | 127.6 | J100043+014607T |
| 10934 | J100047.58+020958.5 | 150.19827 | 2.1663 | 0.380 | 0.019 | 0.669 ^s | FRII | FRII | T | — | 10.04 | 70.4 | J100047+020958T |
| 10935 | J095927.25+023729.3 | 149.86354 | 2.6248 | 2.382 | 0.119 | 0.954 ^s | FRII | FRI | T | — | 21.73 | 172.0 | J095927+023729T |
| 10936 | J100028.23+013508.5 | 150.11766 | 1.5857 | 10.050 | 0.502 | 0.839 ^s | FRI/FRII | — | T | 347 | 48.59 | 370.6 | — |
| 10937 | J095947.83+021023.9 | 149.94931 | 2.1733 | 0.230 | 0.012 | 1.128 ^p | FRII | FRI | T | — | 2.96 | 24.3 | J095947+021024T |
| 10938 | J100138.54+030105.7 | 150.41100 | 3.0327 | 0.849 | 0.042 | 0.913 ^p | FRII | — | F | — | 3.96 | 30.9 | — |
| 10939 | J100242.23+013432.1 | 150.67598 | 1.5756 | 0.367 | 0.018 | 1.519 ^s | FRI | — | T | 161 | 3.42 | 29.0 | J100242+013432 |
| 10940 | J095857.37+021315.5 | 149.73907 | 2.2210 | 0.204 | 0.010 | 1.024 ^s | FRII | — | T | — | 4.11 | 33.1 | 095857+021315 |
| 10941 | J100102.80+012925.9 | 150.26169 | 1.4905 | 0.549 | 0.027 | 2.244 ^p | FRI | — | T | — | 4.88 | 40.2 | — |
| 10942 | J100034.76+014635.7 | 150.14484 | 1.7766 | 0.374 | 0.019 | 0.734 ^s | FRII | — | F | — | 14.56 | 105.9 | J100034+014635 |
| 10943 | J100104.98+013154.6 | 150.27080 | 1.5318 | 0.406 | 0.020 | 1.809 ^p | FRII | — | T | — | 5.96 | 50.3 | — |
| 10945 | J100142.19+023049.9 | 150.35081 | 2.5139 | 0.205 | 0.010 | 0.689 ^s | FRI | — | T | — | 6.2 | 44.0 | — |
| 10947 | J095918.98+014035.9 | 149.82909 | 1.6767 | 0.120 | 0.006 | 2.538 ^p | FRII | FRI | T | — | 6.20 | 49.9 | J095919+014036T |
| 10948 | J100021.78+015959.9 | 150.09076 | 2.0000 | 1.943 | 0.097 | 0.219 ^s | FRII | — | T | 73 | 11.72 | 41.5 | J100021+020000 |
| 10949 | J100124.06+024936.7 | 150.35030 | 2.8269 | 2.718 | 0.136 | 0.826 ^s | FRII | WAT | T | — | 16.78 | 127.4 | J100124+024936T |
| 10950 | J095949.01+025516.4 | 149.95424 | 2.9212 | 1.439 | 0.072 | 0.126 ^s | FRII | — | T | 198 | 10.97 | 24.7 | — |

Table C.1: Radio Properties (Continued)

| 3 GHz ID | COSMOSVLA3 (2) | R.A. (deg) | Dec. (deg) | $S_{3\text{GHz}}$ (mJy) | S_{err} (mJy) | z | 3GHz (8) | radio class 1.4GHz (9) | radio excess (10) | X-ray group ID (11) | LAS (arcsec) (12) | D (kpc) (13) | 1.4GHz ID COSMOSVLA3 (14) |
|-------------|---------------------|---------------|---------------|----------------------------|---------------------------|--------------------|-------------|------------------------------|-------------------------|---------------------------|-------------------------|--------------------|---------------------------------|
| 10951 | J095917.74+020927.8 | 149.82391 | 2.1577 | 0.890 | 0.045 | 1.693 ^p | FR II | – | T | – | 12.65 | 107.1 | J095917+020927 |
| 10952 | J100238.68+022152.2 | 150.66118 | 2.3645 | 1.687 | 0.084 | 0.827 ^s | FR II | WAT | T | – | 16.44 | 124.8 | J100238+022152T |
| 10953 | J100018.50+023256.2 | 150.07710 | 2.5490 | 1.254 | 0.063 | 0.890 ^s | FR II | WAT | T | – | 25.91 | 201.2 | J100018+023256T |
| 10955 | J100307.46+023655.8 | 150.78116 | 2.6155 | 1.058 | 0.053 | 0.370 ^p | FRI | WAT | T | – | 7.53 | 38.5 | J100307+023655 |
| 10956 | J100027.43+022123.3 | 150.11432 | 2.3565 | 4.379 | 0.219 | 0.220 ^s | FR II | – | T | – | 84.56 | 300.6 | – |
| 10957 | J100015.55+020731.4 | 150.06483 | 2.1254 | 0.514 | 0.026 | 0.661 ^s | FRI | – | T | – | 5.62 | 39.2 | J100015+020731 |
| 10958 | J100136.46+022640.7 | 150.40193 | 2.4450 | 0.889 | 0.044 | 0.123 ^s | FRI/FR II | – | T | 149 | 11.85 | 26.2 | – |
| 10959 | J100245.40+024516.1 | 150.68919 | 2.7545 | 8.576 | 0.429 | 0.986 ^p | FR II | – | T | – | 44.02 | 351.4 | – |
| 10962 | J100251.18+024248.0 | 150.71330 | 2.7134 | 80.250 | 4.013 | 0.974 ^p | FR II | – | T | – | 15.03 | 119.6 | – |
| 10963 | J100008.92+024010.4 | 150.03725 | 2.6697 | 0.152 | 0.008 | 1.599 ^s | FRI? | – | F | – | 1.56 | 13.2 | J100008+024010 |
| 10964 | J100211.28+013706.8 | 150.54750 | 1.6186 | 0.092 | 0.005 | 1.592 ^s | FRI? | – | F | – | 1.80 | 15.3 | J100211+013706 |
| 10966 | J100106.73+013320.3 | 150.27806 | 1.5557 | 0.861 | 0.043 | 0.361 ^p | FR II | – | T | – | 12.12 | 61.1 | J100106+013320T |

Table C.2: Host properties of FR objects

| 3 GHz ID | SFR _{IR} (M _⊙ /yr) | log ₁₀ (M*/M _⊙) | SED AGN | counterpart ID | Optical class |
|----------|--|--|---------|------------------------|----------------|
| (1) | (2) | (3) | (4) | (5) | (6) |
| 26 | – | – | – | – | D ^B |
| 33 | 2.54 | 11.30 | F | 786830 ^{C15} | D ^B |
| 38 | – | – | – | – | – |
| 44 | 2.63 | 11.21 | F | 923481 ^{C15} | E |
| 64 | 3.71 | 10.77 | F | 890793 ^{C15} | E |
| 80 | 1.47 | 11.13 | F | 1688919 ^I | – |
| 83 | 37.18 | 11.22 | F | 660985 ^{C15} | – |
| 89 | 12.36 | 10.93 | F | 651098 ^{C15} | – |
| 112 | 29.88 | – | F | 307378 ^{IR} | – |
| 115 | – | – | – | – | – |
| 123 | 430.55 | – | F | 126603 ^{IR} | E |
| 137 | 1.95 | 11.19 | F | 1198880 ^I | E |
| 138 | 29.39 | 11.12 | F | 987678 ^{C15} | D ^B |
| 145 | – | – | – | – | E |
| 153 | 50.98 | 11.37 | F | 925744 ^{C15} | – |
| 160 | 7.20 | 10.58 | F | 909080 ^{C15} | D |
| 164 | – | – | – | – | D ^B |
| 166 | 142.30 | 11.60 | F | 650786 ^{C15} | D |
| 177 | 1.97 | 11.09 | – | 374455 ^{C15} | – |
| 187 | 2.48 | 11.05 | F | 858706 ^{C15} | D ^B |
| 195 | 1038.50 | 10.98 | F | 244448 ^{C15} | IRR |
| 208 | 6.02 | 10.69 | F | 639085 ^{C15} | D ^B |
| 213 | 2.80 | 11.24 | F | 268559 ^{C15} | E |
| 233 | – | – | – | – | – |
| 236 | 16.18 | 11.45 | F | 522790 ^{C15} | D |
| 237 | 16.18 | – | F | 218129 ^{IR} | – |
| 247 | -0.41 | 11.75 | – | 975876 ^{C15} | – |
| 248 | – | – | – | – | – |
| 280 | 3.00 | 11.15 | F | 771790 ^{C15} | D ^B |
| 299 | 2.40 | 11.34 | – | 1066821 ^{C15} | – |
| 307 | 296.58 | 11.27 | F | 968549 ^{C15} | – |
| 311 | 367.53 | 11.17 | F | 202645 ^{C15} | – |
| 319 | 22.37 | 11.54 | F | 1037768 ^{C15} | D |
| 327 | 10.54 | 11.01 | F | 231725 ^{C15} | – |
| 347 | 11.66 | 11.18 | F | 933872 ^{C15} | – |
| 360 | – | – | – | – | E |
| 386 | – | – | – | – | E |
| 404 | 3.06 | 11.18 | T | 962971 ^{C15} | E |
| 433 | 13.56 | – | F | 323662 ^{IR} | – |
| 437 | 0.46 | 11.17 | F | 556464 ^{C15} | E |
| 503 | 10.50 | 10.82 | F | 412242 ^{C15} | – |
| 516 | 35.29 | 11.53 | F | 614988 ^{C15} | E |
| 560 | 22.75 | 10.79 | F | 635990 ^{C15} | D |
| 566 | 19.57 | 11.64 | F | 1671795 ^I | E |
| 584 | 6.45 | 11.24 | F | 1008200 ^{C15} | E |
| 613 | 139.02 | 10.11 | T | 703742 ^{C15} | – |
| 619 | 13.32 | 11.36 | T | 808541 ^{C15} | D |

Table C.2: Host properties of FR objects (continued)

| 3 GHz ID | SFR _{IR} (M _⊙ /yr) | log ₁₀ (M*/M _⊙) | SED AGN | counterpart ID | Optical class |
|----------|--|--|---------|------------------------|----------------|
| (1) | (2) | (3) | (4) | (5) | (6) |
| 629 | 11.26 | 11.21 | F | 779565 ^{C15} | E |
| 739 | 2.31 | 11.32 | F | 628153 ^{C15} | D ^B |
| 743 | 45.47 | 11.38 | F | 231975 ^{C15} | D |
| 746 | 12.80 | – | F | 250473 ^{IR} | – |
| 773 | 169.46 | 10.67 | T | 638834 ^I | – |
| 798 | 11.07 | 11.24 | F | 1039971 ^{C15} | – |
| 840 | 4.24 | 10.94 | F | 370210 ^{C15} | E |
| 936 | 8.63 | 11.38 | F | 503434 ^{C15} | D ^B |
| 942 | 1.81 | 10.77 | F | 987852 ^{C15} | E |
| 976 | – | – | – | – | – |
| 1031 | – | – | – | – | – |
| 1290 | 4.11 | 10.96 | F | 247648 ^{C15} | E |
| 1411 | 37.16 | 11.40 | F | 652572 ^{C15} | D |
| 2251 | – | – | – | – | – |
| 2399 | 224.84 | – | F | 7882 ^{IR} | – |
| 2516 | 1.71 | 10.68 | – | 307947 ^{C15} | – |
| 2660 | 68.45 | 11.14 | T | 1938693 ^I | – |
| 3065 | 1.51 | 10.98 | – | 953712 ^{C15} | – |
| 3112 | – | – | – | – | – |
| 3528 | 11.62 | – | F | 236344 ^{IR} | – |
| 3866 | 4.21 | 11.15 | F | 694093 ^{C15} | D ^B |
| 7087 | – | – | -99 | – | – |
| 10900 | 100.79 | 11.47 | T | 934339 ^{C15} | – |
| 10901 | 343.75 | 11.32 | F | 446143 ^{C15} | D |
| 10902 | 37.08 | 10.61 | T | 754369 ^{C15} | – |
| 10903 | 31.34 | 11.01 | T | 912632 ^{C15} | IRR |
| 10904 | 93.92 | 11.14 | T | 459835 ^{C15} | D |
| 10905 | 7.58 | 11.46 | F | 809167 ^{C15} | E |
| 10906 | 11.74 | 11.11 | F | 809443 ^{C15} | D |
| 10907 | 16.85 | 11.21 | F | 761486 ^{C15} | – |
| 10908 | 16.85 | – | F | 380833 ^{IR} | – |
| 10909 | 139.05 | 11.63 | F | 936454 ^{C15} | D |
| 10910 | 6.11 | 11.30 | F | 350495 ^{C15} | E |
| 10911 | 37.66 | 11.49 | T | 486067 ^{C15} | – |
| 10912 | 6.48 | 11.46 | F | 636013 ^{C15} | – |
| 10913 | 6.68 | 11.67 | F | 901584 ^{C15} | D ^B |
| 10914 | 11.48 | 11.12 | F | 561934 ^{C15} | – |
| 10915 | 186.19 | 11.10 | F | 343802 ^{C15} | – |
| 10916 | 8.40 | 10.90 | F | 374634 ^{C15} | D |
| 10917 | 27.46 | 11.34 | F | 960761 ^{C15} | – |
| 10918 | 2.23 | 11.59 | F | 996897 ^{C15} | E |
| 10919 | 42.03 | 11.00 | F | 407780 ^{C15} | – |
| 10920 | 78.69 | 10.76 | F | 210704 ^{C15} | – |
| 10921 | 12.60 | 10.83 | F | 759401 ^{C15} | D |
| 10922 | 9.27 | 11.04 | F | 1349607 ^I | – |
| 10923 | 28.32 | 11.63 | F | 333779 ^{C15} | E |
| 10924 | 28.32 | – | F | 351323 ^{IR} | – |
| 10925 | 12.09 | 11.21 | F | 372940 ^{C15} | – |
| 10926 | 37.76 | 10.89 | F | 429082 ^{C15} | – |
| 10927 | 7.40 | 10.66 | F | 517689 ^{C15} | – |
| 10928 | 14.78 | 10.86 | F | 978441 ^{C15} | D |
| 10929 | 52.21 | 10.92 | F | 410131 ^{C15} | – |
| 10930 | 102.60 | 11.41 | F | 374873 ^{C15} | – |
| 10931 | 4.68 | 11.39 | F | 292852 ^{C15} | D ^B |

Notes. Host-galaxy properties. **Column 1:** 3 GHz ID; **Columns 2 & 3:** SFR in M_⊙/yr and stellar mass M^* in M_⊙ from the fit to the infrared SED [Delvecchio et al. \(2017\)](#), respectively; **Column 4:** AGN based on the SED fit as in [Delvecchio et al. \(2017\)](#): "T" for AGN, "F" no AGN; **Column 5:** counterpart ID from [Smolčić et al. \(2017b\)](#); C15 stands for COSMOS2015; IR is for IRAC ID; I is for i-band ID; **Column 6:** Gives the optical morphology from [Schinnerer et al. \(2010\)](#): "E" for early-type elliptical, "D" for disk galaxy, "IRR" for irregular/peculiar galaxy, "B" for bulge dominated disk.

Table C.2: Host properties of FR objects (continued)

| 3 GHz ID (1) | SFR _{IR} (M _⊙ /yr) (2) | log ₁₀ (M*/M _⊙) (3) | SED AGN (4) | counterpart ID (5) | Optical class (6) |
|--------------------|--|--|-------------------|--------------------------|-------------------------|
| 10932 | 30.81 | 11.61 | F | 2011437 ^I | – |
| 10933 | 3.93 | 11.53 | F | 305535 ^{C15} | – |
| 10934 | 5.71 | 11.21 | F | 570506 ^{C15} | E |
| 10935 | 36.20 | 11.33 | F | 873867 ^{C15} | E |
| 10936 | 4.76 | 11.01 | F | 202465 ^{C15} | D ^B |
| 10937 | 18.09 | 11.07 | F | 575428 ^{C15} | – |
| 10938 | 18.09 | – | F | 351652 ^{IR} | – |
| 10939 | 88.10 | 11.64 | T | 195117 ^{C15} | – |
| 10940 | 85.65 | 10.39 | T | 609017 ^{C15} | – |
| 10941 | 97.54 | 11.06 | F | 134089 ^{C15} | – |
| 10942 | 7.77 | 11.03 | F | 323222 ^{C15} | D ^B |
| 10943 | 1.36 | 8.10 | F | 163557 ^{C15} | – |
| 10945 | 2.71 | 11.22 | T | 801950 ^{C15} | – |
| 10947 | 275.12 | 10.51 | F | 261526 ^{C15} | – |
| 10948 | 0.94 | 11.28 | F | 447542 ^{C15} | E |
| 10949 | 8.97 | 11.40 | F | 1003852 ^{C15} | E |
| 10950 | 0.29 | 10.75 | F | 1068567 ^{C15} | – |
| 10951 | 143.68 | 11.72 | F | 565211 ^{C15} | – |
| 10952 | 5.89 | 11.00 | F | 704802 ^{C15} | D ^B |
| 10953 | 4.54 | 11.30 | F | 826044 ^{C15} | E |
| 10955 | 2.71 | 10.62 | F | 869175 ^{C15} | – |
| 10956 | 0.99 | 11.20 | F | 689074 ^{C15} | E |
| 10957 | 4.43 | 11.10 | F | 544105 ^{C15} | E |
| 10958 | 1.61 | 10.59 | F | 1174670 ^I | E |
| 10959 | 34.87 | 11.37 | F | 957772 ^{C15} | E |
| 10962 | 34.30 | 10.95 | T | 931677 ^{C15} | E |
| 10963 | 610.07 | 10.38 | F | 902320 ^{C15} | – |
| 10964 | 199.48 | 12.12 | T | 223951 ^{C15} | – |
| 10966 | 1.50 | 11.04 | F | 182559 ^{C15} | – |

Table C.3: Eddington ratios for FRs and COM AGN

| ID | radio class | λ_r | λ_{rk} | log ₁₀ (L _{jet} / erg s ⁻¹) | L _X / L _{radio} | log ₁₀ (M _{BH} / M _⊙) |
|-----|----------------|-------------|----------------|--|--|--|
| 2 | COM AGN | -0.93 | -0.4 | 45.86 | 1.78 | 8.27 |
| 3 | COM AGN | -1.00 | -0.2 | 45.35 | 1.80 | 7.51 |
| 6 | COM AGN | -2.77 | -1.0 | 45.67 | 0.69 | 8.53 |
| 7 | COM AGN | -1.26 | -1.1 | 45.44 | 2.59 | 8.92 |
| 8 | COM AGN | -0.68 | -0.6 | 45.28 | 2.85 | 8.38 |
| 16 | COM AGN | -1.77 | -0.2 | 46.18 | 0.71 | 8.33 |
| 17 | COM AGN | -1.24 | -1.2 | 44.62 | 3.40 | 8.52 |
| 18 | COM AGN | -3.17 | -2.2 | 44.01 | 2.21 | 8.22 |
| 22 | COM AGN | 0.75 | 0.7 | 45.04 | 3.50 | 7.42 |
| 29 | COM AGN | -3.94 | -2.5 | 44.29 | 1.60 | 8.75 |
| 31 | COM AGN | -2.12 | -1.0 | 45.57 | 1.40 | 8.53 |
| 33 | FRI/FRII | -3.14 | -2.4 | 44.26 | 2.29 | 8.60 |
| 35 | COM AGN | -3.62 | -2.9 | 43.64 | 2.54 | 8.51 |
| 40 | COM AGN | -2.25 | -1.9 | 44.55 | 2.71 | 8.61 |
| 41 | COM AGN | -2.64 | -2.0 | 44.60 | 2.32 | 8.62 |
| 44 | FRII | -3.66 | -2.2 | 44.38 | 1.52 | 8.51 |
| 45 | COM AGN | -2.74 | -1.9 | 44.31 | 2.24 | 8.24 |
| 51 | COM AGN | -2.32 | -1.6 | 44.72 | 2.15 | 8.32 |
| 52 | COM AGN | -1.15 | -1.1 | 43.61 | 4.56 | 8.20 |
| 53 | COM AGN | -2.56 | -2.2 | 44.36 | 2.70 | 8.62 |
| 57 | COM AGN | -1.82 | -0.8 | 44.99 | 1.73 | 7.73 |
| 58 | COM AGN | -2.08 | -1.6 | 44.78 | 2.46 | 8.49 |
| 61 | COM AGN | -2.67 | -2.4 | 43.89 | 3.13 | 8.50 |
| 65 | COM AGN | -3.04 | -2.6 | 43.89 | 2.84 | 8.56 |
| 80 | FRI | -4.11 | -2.8 | 43.67 | 1.91 | 8.42 |
| 81 | COM AGN | -2.23 | -1.3 | 45.12 | 1.78 | 8.38 |
| 88 | COM AGN | -3.29 | -2.8 | 44.03 | 2.68 | 8.85 |
| 93 | COM AGN | -2.52 | -1.9 | 44.19 | 2.50 | 8.12 |
| 105 | COM AGN | -2.60 | -2.5 | 43.13 | 3.97 | 8.25 |
| 120 | COM AGN | -2.64 | -2.1 | 45.01 | 2.23 | 9.13 |
| 122 | COM AGN | -1.88 | -1.4 | 44.94 | 2.39 | 8.42 |
| 125 | COM AGN | -1.76 | -1.0 | 44.34 | 2.31 | 7.35 |
| 139 | COM AGN | -0.39 | -0.2 | 44.14 | 3.37 | 6.84 |
| 140 | COM AGN | -1.52 | -1.5 | 43.99 | 4.13 | 8.66 |
| 143 | COM AGN | -0.78 | -0.6 | 45.14 | 2.69 | 8.05 |
| 152 | COM AGN | -2.50 | -2.1 | 44.70 | 2.60 | 8.95 |
| 155 | COM AGN | -1.17 | -1.1 | 45.15 | 2.93 | 8.76 |
| 175 | COM AGN | -0.78 | -0.8 | 43.80 | 4.60 | 8.20 |
| 180 | COM AGN | -3.16 | -2.0 | 44.71 | 1.66 | 8.61 |
| 182 | COM AGN | -3.91 | -2.9 | 44.04 | 2.14 | 8.93 |
| 183 | COM AGN | -2.68 | -2.3 | 42.75 | 3.28 | 6.99 |
| 195 | FRI/FRII | -1.98 | -1.3 | 45.00 | 2.07 | 8.28 |
| 208 | FRI/FRII | -1.63 | -1.0 | 45.00 | 2.12 | 7.99 |
| 212 | COM AGN | -1.27 | -1.2 | 44.14 | 3.90 | 8.37 |
| 217 | COM AGN | -0.14 | -0.1 | 44.11 | 3.82 | 7.09 |
| 224 | COM AGN | -3.04 | -2.2 | 44.32 | 2.22 | 8.52 |
| 229 | COM AGN | -1.76 | -0.8 | 45.66 | 1.48 | 8.39 |
| 251 | COM AGN | -3.50 | -3.2 | 42.98 | 3.45 | 8.40 |
| 252 | COM AGN | -3.22 | -2.7 | 43.57 | 2.89 | 8.35 |
| 256 | COM AGN | -3.44 | -2.4 | 43.66 | 2.16 | 7.97 |
| 257 | COM AGN | -2.23 | -1.7 | 44.81 | 2.40 | 8.62 |
| 265 | COM AGN | -2.39 | -2.1 | 43.98 | 3.07 | 8.28 |
| 267 | COM AGN | -1.94 | -1.8 | 44.46 | 3.20 | 8.73 |
| 273 | COM AGN | -2.20 | -2.0 | 43.97 | 3.35 | 8.39 |
| 285 | COM AGN | -3.13 | -2.6 | 44.06 | 2.62 | 8.66 |
| 294 | COM AGN | -1.24 | -1.2 | 44.70 | 3.50 | 8.77 |
| 295 | COM AGN | -2.10 | -1.6 | 44.22 | 2.58 | 7.81 |
| 296 | COM AGN | -2.78 | -2.2 | 44.13 | 2.63 | 8.42 |
| 300 | COM AGN | -2.55 | -2.4 | 43.76 | 3.35 | 8.45 |
| 302 | COM AGN | -1.18 | -1.1 | 44.17 | 3.78 | 8.19 |

Table C.3: Eddington ratios for FRs and COM AGN (continued)

| ID | radio class | λ_r | λ_{rk} | $\log_{10}(L_{\text{jet}} / \text{erg s}^{-1})$ | L_X / L_{radio} | $\log_{10}(M_{\text{BH}} / M_{\odot})$ |
|------|-------------|-------------|----------------|---|--------------------------|--|
| 307 | FRI/FRII | -2.45 | -1.3 | 45.33 | 1.47 | 8.57 |
| 333 | COM AGN | -2.09 | -1.9 | 43.83 | 3.45 | 8.19 |
| 350 | COM AGN | -2.06 | -1.4 | 45.03 | 2.08 | 8.42 |
| 352 | COM AGN | -3.10 | -2.5 | 43.82 | 2.72 | 8.40 |
| 358 | COM AGN | -0.24 | -0.2 | 44.53 | 4.06 | 8.24 |
| 363 | COM AGN | -2.54 | -2.1 | 44.15 | 2.82 | 8.39 |
| 366 | COM AGN | -2.48 | -2.3 | 43.87 | 3.38 | 8.55 |
| 369 | COM AGN | -2.84 | -2.5 | 43.74 | 3.09 | 8.38 |
| 376 | COM AGN | -3.78 | -3.4 | 42.79 | 3.30 | 8.31 |
| 381 | COM AGN | -2.94 | -2.5 | 43.51 | 2.97 | 8.08 |
| 389 | COM AGN | -3.20 | -2.8 | 43.80 | 2.93 | 8.70 |
| 402 | COM AGN | -2.12 | -2.0 | 44.01 | 3.47 | 8.50 |
| 405 | COM AGN | -2.54 | -1.8 | 43.55 | 2.54 | 7.31 |
| 409 | COM AGN | -3.87 | -3.2 | 43.38 | 2.75 | 8.62 |
| 415 | COM AGN | -1.71 | -1.6 | 44.31 | 3.43 | 8.51 |
| 443 | COM AGN | -1.68 | -1.6 | 44.15 | 3.55 | 8.40 |
| 452 | COM AGN | -1.07 | -0.9 | 44.04 | 3.41 | 7.42 |
| 514 | COM AGN | -3.11 | -2.9 | 43.18 | 3.46 | 8.29 |
| 520 | COM AGN | -3.81 | -3.0 | 43.43 | 2.50 | 8.36 |
| 522 | COM AGN | -4.15 | -3.3 | 42.57 | 2.68 | 7.82 |
| 528 | COM AGN | -3.30 | -2.8 | 43.35 | 3.02 | 8.27 |
| 529 | COM AGN | -1.93 | -1.6 | 44.23 | 2.96 | 8.08 |
| 537 | COM AGN | -2.06 | -1.8 | 44.04 | 3.17 | 8.16 |
| 556 | COM AGN | -2.28 | -1.8 | 44.79 | 2.45 | 8.68 |
| 568 | COM AGN | -3.28 | -3.1 | 43.21 | 3.68 | 8.73 |
| 572 | COM AGN | -1.42 | -1.4 | 43.64 | 4.25 | 8.15 |
| 586 | COM AGN | -0.47 | -0.5 | 44.37 | 4.34 | 8.55 |
| 601 | COM AGN | -1.92 | -1.8 | 43.95 | 3.66 | 8.44 |
| 614 | COM AGN | -2.52 | -2.2 | 44.03 | 2.97 | 8.38 |
| 616 | COM AGN | -3.56 | -2.9 | 43.09 | 2.81 | 8.03 |
| 618 | COM AGN | -2.67 | -2.4 | 43.68 | 3.19 | 8.26 |
| 626 | COM AGN | -0.55 | -0.4 | 44.45 | 3.31 | 7.44 |
| 630 | COM AGN | -3.62 | -2.9 | 43.79 | 2.53 | 8.68 |
| 655 | COM AGN | -3.89 | -3.1 | 42.94 | 2.65 | 7.88 |
| 666 | COM AGN | -1.76 | -1.7 | 43.97 | 3.80 | 8.45 |
| 714 | COM AGN | -3.21 | -2.7 | 43.62 | 2.95 | 8.45 |
| 718 | COM AGN | -2.56 | -2.3 | 43.95 | 3.14 | 8.47 |
| 722 | COM AGN | -3.27 | -3.1 | 43.67 | 3.37 | 9.04 |
| 725 | COM AGN | -3.31 | -2.9 | 43.46 | 3.13 | 8.54 |
| 729 | COM AGN | -0.99 | -0.9 | 44.38 | 3.75 | 8.31 |
| 738 | COM AGN | -1.72 | -1.7 | 43.94 | 4.18 | 8.84 |
| 740 | COM AGN | -1.54 | -1.5 | 43.98 | 4.08 | 8.59 |
| 773 | FRI | 0.58 | 0.6 | 44.63 | 4.31 | 7.97 |
| 791 | COM AGN | -1.20 | -1.0 | 44.89 | 2.95 | 8.37 |
| 830 | COM AGN | -2.98 | -2.2 | 44.17 | 2.28 | 8.33 |
| 834 | COM AGN | -0.65 | -0.5 | 44.74 | 3.19 | 7.84 |
| 845 | COM AGN | -0.58 | -0.5 | 45.33 | 2.80 | 8.30 |
| 852 | COM AGN | -3.16 | -2.7 | 43.62 | 2.91 | 8.37 |
| 854 | COM AGN | -2.00 | -1.9 | 44.29 | 3.33 | 8.63 |
| 869 | COM AGN | -0.80 | -0.8 | 44.44 | 3.91 | 8.43 |
| 877 | COM AGN | -0.07 | -0.1 | 44.78 | 3.95 | 8.37 |
| 882 | COM AGN | -2.77 | -2.1 | 44.69 | 2.27 | 8.81 |
| 883 | COM AGN | -0.28 | -0.1 | 44.75 | 2.95 | 7.21 |
| 888 | COM AGN | -4.12 | -3.6 | 42.73 | 3.18 | 8.64 |
| 954 | COM AGN | -1.44 | -1.4 | 43.42 | 4.88 | 8.58 |
| 958 | COM AGN | -3.14 | -2.8 | 43.92 | 3.01 | 8.86 |
| 978 | COM AGN | -3.77 | -3.5 | 42.59 | 3.57 | 8.39 |
| 1012 | COM AGN | -2.04 | -1.9 | 43.06 | 3.94 | 7.56 |
| 1024 | COM AGN | -2.53 | -2.4 | 43.51 | 3.72 | 8.45 |
| 1049 | COM AGN | -1.97 | -1.8 | 44.19 | 3.23 | 8.37 |

Table C.3: Eddington ratios for FRs and COM AGN (continued)

| ID | radio class | λ_r | λ_{rk} | $\log_{10}(L_{\text{jet}} / \text{erg s}^{-1})$ | L_X / L_{radio} | $\log_{10}(M_{\text{BH}} / M_{\odot})$ |
|------|-------------|-------------|----------------|---|--------------------------|--|
| 1061 | COM AGN | -2.66 | -2.5 | 43.72 | 3.48 | 8.59 |
| 1076 | COM AGN | -1.21 | -1.0 | 44.30 | 3.16 | 7.69 |
| 1082 | COM AGN | -3.56 | -3.2 | 43.22 | 3.25 | 8.59 |
| 1136 | COM AGN | -2.88 | -2.4 | 43.85 | 2.79 | 8.29 |
| 1139 | COM AGN | -2.34 | -1.8 | 44.49 | 2.51 | 8.36 |
| 1151 | COM AGN | -3.72 | -3.3 | 42.97 | 3.29 | 8.46 |
| 1152 | COM AGN | -0.88 | -0.8 | 44.55 | 3.60 | 8.31 |
| 1175 | COM AGN | -1.47 | -1.3 | 44.38 | 3.07 | 7.97 |
| 1205 | COM AGN | -2.93 | -2.6 | 43.72 | 3.07 | 8.47 |
| 1225 | COM AGN | -1.73 | -1.7 | 44.27 | 3.59 | 8.66 |
| 1237 | COM AGN | -2.95 | -2.5 | 44.03 | 2.78 | 8.61 |
| 1283 | COM AGN | -1.90 | -1.7 | 43.95 | 3.30 | 8.01 |
| 1298 | COM AGN | -2.87 | -2.7 | 43.46 | 3.74 | 8.74 |
| 1306 | COM AGN | -0.34 | -0.3 | 44.51 | 3.91 | 8.07 |
| 1317 | COM AGN | -0.51 | -0.4 | 44.53 | 3.23 | 7.40 |
| 1332 | COM AGN | -0.71 | -0.6 | 44.23 | 3.50 | 7.47 |
| 1338 | COM AGN | -1.25 | -1.2 | 43.70 | 4.19 | 7.99 |
| 1363 | COM AGN | -1.29 | -1.3 | 43.74 | 4.30 | 8.24 |
| 1382 | COM AGN | -1.28 | -1.2 | 43.66 | 4.27 | 8.03 |
| 1393 | COM AGN | -3.39 | -3.0 | 42.85 | 3.24 | 7.90 |
| 1397 | COM AGN | -2.65 | -2.5 | 43.75 | 3.45 | 8.63 |
| 1446 | COM AGN | -2.43 | -2.3 | 43.88 | 3.69 | 8.87 |
| 1455 | COM AGN | -2.66 | -2.4 | 43.53 | 3.40 | 8.27 |
| 1466 | COM AGN | -0.40 | -0.4 | 44.32 | 4.26 | 8.29 |
| 1477 | COM AGN | -1.67 | -1.6 | 43.17 | 4.63 | 8.09 |
| 1482 | COM AGN | -2.20 | -2.1 | 44.04 | 3.60 | 8.77 |
| 1489 | COM AGN | -2.04 | -1.9 | 43.81 | 3.41 | 8.07 |
| 1496 | COM AGN | -0.87 | -0.9 | 44.09 | 4.08 | 8.11 |
| 1504 | COM AGN | -0.74 | -0.7 | 44.07 | 3.96 | 7.81 |
| 1508 | COM AGN | -1.35 | -1.3 | 43.93 | 4.15 | 8.40 |
| 1539 | COM AGN | -0.10 | -0.0 | 44.95 | 3.23 | 7.74 |
| 1545 | COM AGN | -2.68 | -2.1 | 44.60 | 2.44 | 8.77 |
| 1565 | COM AGN | -0.62 | -0.6 | 43.88 | 4.94 | 8.63 |
| 1572 | COM AGN | -1.80 | -1.7 | 43.99 | 3.56 | 8.22 |
| 1607 | COM AGN | -0.33 | -0.2 | 43.60 | 3.88 | 6.52 |
| 1608 | COM AGN | -2.23 | -2.2 | 43.53 | 4.03 | 8.55 |
| 1647 | COM AGN | -1.56 | -1.5 | 43.79 | 3.69 | 7.87 |
| 1669 | COM AGN | -0.65 | -0.7 | 43.95 | 4.89 | 8.72 |
| 1678 | COM AGN | -0.14 | -0.1 | 42.88 | 5.63 | 7.29 |
| 1698 | COM AGN | -1.54 | -1.5 | 44.41 | 3.47 | 8.54 |
| 1726 | COM AGN | -2.32 | -2.0 | 44.29 | 2.99 | 8.54 |
| 1743 | COM AGN | -1.96 | -1.8 | 44.00 | 3.48 | 8.33 |
| 1745 | COM AGN | -1.72 | -1.5 | 44.48 | 2.94 | 8.19 |
| 1757 | COM AGN | -0.13 | -0.1 | 44.30 | 4.49 | 8.30 |
| 1792 | COM AGN | -2.24 | -2.1 | 43.89 | 3.46 | 8.44 |
| 1803 | COM AGN | -2.65 | -2.4 | 43.76 | 3.25 | 8.42 |
| 1826 | COM AGN | -0.52 | -0.5 | 44.10 | 4.12 | 7.82 |
| 1871 | COM AGN | -1.02 | -0.8 | 45.28 | 2.61 | 8.41 |
| 1938 | COM AGN | -2.38 | -2.3 | 42.64 | 4.42 | 7.82 |
| 1989 | COM AGN | -1.87 | -1.8 | 43.31 | 3.87 | 7.66 |
| 1990 | COM AGN | -0.81 | -0.7 | 45.36 | 2.68 | 8.43 |
| 2029 | COM AGN | -2.36 | -2.1 | 43.54 | 3.32 | 7.90 |
| 2033 | COM AGN | -0.72 | -0.7 | 44.14 | 4.15 | 8.14 |
| 2046 | COM AGN | -1.30 | -1.2 | 43.95 | 3.68 | 7.83 |
| 2052 | COM AGN | -1.83 | -1.7 | 43.64 | 3.72 | 7.95 |
| 2114 | COM AGN | -2.59 | -2.4 | 43.49 | 3.63 | 8.38 |
| 2145 | COM AGN | -2.20 | -2.1 | 43.86 | 3.46 | 8.34 |
| 2178 | COM AGN | -1.85 | -1.7 | 44.17 | 3.37 | 8.35 |
| 2186 | COM AGN | -0.79 | -0.8 | 43.76 | 4.72 | 8.28 |
| 2187 | COM AGN | -1.18 | -1.1 | 44.37 | 3.60 | 8.29 |

Table C.3: Eddington ratios for FRs and COM AGN (continued)

| ID | radio class | λ_r | λ_{rk} | $\log_{10}(L_{\text{jet}} / \text{erg s}^{-1})$ | L_X / L_{radio} | $\log_{10}(M_{\text{BH}} / M_{\odot})$ |
|------|-------------|-------------|----------------|---|--------------------------|--|
| 2236 | COM AGN | -1.94 | -1.8 | 43.88 | 3.65 | 8.32 |
| 2244 | COM AGN | -0.51 | -0.5 | 44.31 | 4.07 | 8.14 |
| 2267 | COM AGN | -2.36 | -2.1 | 43.53 | 3.42 | 7.95 |
| 2287 | COM AGN | -2.80 | -2.6 | 42.68 | 3.74 | 7.59 |
| 2291 | COM AGN | -2.15 | -2.1 | 43.47 | 3.95 | 8.28 |
| 2321 | COM AGN | -1.92 | -1.8 | 44.15 | 3.34 | 8.37 |
| 2330 | COM AGN | -1.59 | -1.4 | 43.59 | 3.35 | 7.23 |
| 2391 | COM AGN | -0.76 | -0.6 | 44.07 | 3.21 | 6.94 |
| 2438 | COM AGN | -1.36 | -1.3 | 43.86 | 3.97 | 8.10 |
| 2479 | COM AGN | -3.15 | -2.8 | 43.57 | 3.19 | 8.59 |
| 2511 | COM AGN | -2.56 | -2.3 | 43.48 | 3.36 | 8.04 |
| 2550 | COM AGN | -3.22 | -3.0 | 43.04 | 3.55 | 8.31 |
| 2562 | COM AGN | -1.24 | -1.1 | 44.52 | 3.15 | 8.05 |
| 2569 | COM AGN | -3.13 | -2.7 | 43.22 | 3.09 | 8.00 |
| 2575 | COM AGN | -1.79 | -1.7 | 43.75 | 3.90 | 8.28 |
| 2576 | COM AGN | -1.94 | -1.9 | 44.02 | 3.74 | 8.64 |
| 2628 | COM AGN | -2.37 | -2.2 | 43.37 | 3.58 | 7.95 |
| 2659 | COM AGN | -0.87 | -0.9 | 43.93 | 4.32 | 8.15 |
| 2733 | COM AGN | -1.77 | -1.7 | 43.88 | 3.79 | 8.32 |
| 2754 | COM AGN | -2.48 | -2.2 | 44.16 | 2.97 | 8.52 |
| 2807 | COM AGN | -1.47 | -1.5 | 43.57 | 4.38 | 8.24 |
| 2811 | COM AGN | -2.84 | -2.5 | 43.32 | 3.21 | 7.94 |
| 2828 | COM AGN | -2.69 | -2.6 | 42.88 | 4.32 | 8.36 |
| 2922 | COM AGN | -2.31 | -2.1 | 43.87 | 3.32 | 8.32 |
| 2948 | COM AGN | -1.29 | -1.2 | 43.60 | 3.95 | 7.59 |
| 3126 | COM AGN | -2.34 | -1.9 | 44.86 | 2.46 | 8.87 |
| 3172 | COM AGN | -0.69 | -0.6 | 44.47 | 3.34 | 7.66 |
| 3255 | COM AGN | -2.37 | -2.2 | 43.65 | 3.38 | 8.11 |
| 3284 | COM AGN | -2.49 | -2.1 | 43.55 | 3.17 | 7.87 |
| 3318 | COM AGN | -0.52 | -0.5 | 44.17 | 4.18 | 8.03 |
| 3325 | COM AGN | -4.53 | -3.9 | 42.65 | 2.98 | 8.64 |
| 3335 | COM AGN | -2.34 | -2.2 | 43.67 | 3.66 | 8.43 |
| 3365 | COM AGN | -1.99 | -1.9 | 43.98 | 3.76 | 8.63 |
| 3367 | COM AGN | -3.55 | -3.1 | 42.98 | 3.17 | 8.17 |
| 3390 | COM AGN | -1.45 | -1.0 | 43.61 | 3.02 | 6.77 |
| 3391 | COM AGN | -1.29 | -1.2 | 43.86 | 3.89 | 7.91 |
| 3414 | COM AGN | -0.64 | -0.6 | 43.54 | 4.94 | 8.05 |
| 3449 | COM AGN | -2.12 | -2.0 | 43.91 | 3.58 | 8.46 |
| 3503 | COM AGN | -2.47 | -2.4 | 43.36 | 3.84 | 8.28 |
| 3561 | COM AGN | -1.56 | -1.5 | 44.26 | 3.43 | 8.29 |
| 3573 | COM AGN | -0.78 | -0.5 | 44.42 | 2.99 | 7.26 |
| 3581 | COM AGN | -2.61 | -2.4 | 43.51 | 3.45 | 8.25 |
| 3589 | COM AGN | -0.81 | -0.8 | 43.68 | 4.90 | 8.42 |
| 3660 | COM AGN | -1.34 | -1.0 | 42.97 | 3.30 | 6.08 |
| 3774 | COM AGN | -3.77 | -3.3 | 43.51 | 2.99 | 8.92 |
| 3829 | COM AGN | -2.98 | -2.7 | 43.89 | 3.10 | 8.75 |
| 3897 | COM AGN | -2.67 | -2.5 | 43.17 | 3.61 | 8.00 |
| 3905 | COM AGN | -0.92 | -0.9 | 44.24 | 3.76 | 8.00 |
| 3918 | COM AGN | -2.08 | -1.8 | 43.67 | 3.23 | 7.72 |
| 3987 | COM AGN | -1.09 | -1.0 | 44.00 | 3.94 | 8.00 |
| 3992 | COM AGN | -1.84 | -1.0 | 45.04 | 1.89 | 7.99 |
| 4076 | COM AGN | -3.22 | -3.0 | 43.09 | 3.50 | 8.30 |
| 4090 | COM AGN | -2.42 | -2.2 | 43.55 | 3.51 | 8.16 |
| 4142 | COM AGN | -1.56 | -1.5 | 43.95 | 4.22 | 8.74 |
| 4196 | COM AGN | -0.77 | -0.7 | 43.89 | 4.54 | 8.26 |
| 4241 | COM AGN | -2.73 | -2.6 | 42.81 | 3.84 | 7.80 |
| 4249 | COM AGN | -2.46 | -2.4 | 43.13 | 4.23 | 8.37 |
| 4277 | COM AGN | -0.24 | -0.2 | 44.00 | 4.51 | 7.88 |
| 4289 | COM AGN | -2.13 | -2.1 | 43.17 | 4.30 | 8.18 |
| 4358 | COM AGN | -2.43 | -2.3 | 43.38 | 3.75 | 8.16 |

Table C.3: Eddington ratios for FRs and COM AGN (continued)

| ID | radio class | λ_r | λ_{rk} | $\log_{10}(L_{\text{jet}} / \text{erg s}^{-1})$ | L_X / L_{radio} | $\log_{10}(M_{\text{BH}} / M_{\odot})$ |
|-------|-------------|-------------|----------------|---|--------------------------|--|
| 4417 | COM AGN | -2.13 | -2.0 | 43.49 | 3.75 | 8.02 |
| 4492 | COM AGN | -2.71 | -2.5 | 43.16 | 3.69 | 8.09 |
| 4599 | COM AGN | -1.67 | -1.6 | 43.90 | 3.85 | 8.34 |
| 4710 | COM AGN | -1.85 | -1.6 | 44.05 | 3.22 | 8.01 |
| 4761 | COM AGN | -2.47 | -2.2 | 44.38 | 3.03 | 8.90 |
| 4781 | COM AGN | -1.38 | -1.4 | 43.27 | 4.87 | 8.24 |
| 4838 | COM AGN | -1.88 | -1.4 | 44.35 | 2.66 | 7.87 |
| 4865 | COM AGN | -0.16 | -0.2 | 44.33 | 4.14 | 7.90 |
| 4939 | COM AGN | -1.50 | -1.4 | 43.89 | 3.74 | 8.02 |
| 5051 | COM AGN | -0.78 | -0.8 | 44.04 | 4.46 | 8.42 |
| 5116 | COM AGN | -2.28 | -2.1 | 44.11 | 3.25 | 8.58 |
| 5200 | COM AGN | -2.53 | -2.1 | 44.14 | 2.81 | 8.36 |
| 5359 | COM AGN | -1.34 | -1.3 | 43.70 | 3.86 | 7.68 |
| 5365 | COM AGN | 0.43 | 0.4 | 44.02 | 4.80 | 7.55 |
| 5446 | COM AGN | -1.46 | -1.4 | 44.09 | 3.69 | 8.21 |
| 5567 | COM AGN | -0.62 | -0.6 | 44.00 | 4.21 | 7.85 |
| 5614 | COM AGN | -0.43 | -0.4 | 44.19 | 3.95 | 7.68 |
| 5633 | COM AGN | -1.36 | -1.3 | 43.58 | 4.10 | 7.84 |
| 5654 | COM AGN | -2.61 | -2.4 | 44.02 | 3.28 | 8.79 |
| 5673 | COM AGN | -3.10 | -2.8 | 43.94 | 3.13 | 9.00 |
| 5686 | COM AGN | -2.59 | -2.4 | 43.32 | 3.61 | 8.10 |
| 5749 | COM AGN | -3.01 | -2.8 | 42.85 | 3.77 | 8.06 |
| 5779 | COM AGN | 0.12 | 0.2 | 43.70 | 4.58 | 7.02 |
| 5959 | COM AGN | -2.25 | -2.2 | 43.17 | 4.11 | 8.13 |
| 6050 | COM AGN | -1.16 | -1.1 | 44.62 | 3.31 | 8.33 |
| 6159 | COM AGN | -3.04 | -2.6 | 43.44 | 3.03 | 8.14 |
| 6482 | COM AGN | -1.50 | -1.5 | 43.80 | 4.36 | 8.60 |
| 6538 | COM AGN | -1.28 | -1.2 | 43.79 | 4.14 | 8.06 |
| 6623 | COM AGN | -1.91 | -1.8 | 43.70 | 3.99 | 8.40 |
| 6665 | COM AGN | -0.87 | -0.9 | 43.69 | 4.65 | 8.15 |
| 6674 | COM AGN | -1.58 | -1.6 | 43.57 | 4.65 | 8.64 |
| 6712 | COM AGN | -2.07 | -2.0 | 43.55 | 4.19 | 8.57 |
| 6732 | COM AGN | -2.39 | -2.3 | 43.26 | 3.85 | 8.09 |
| 6782 | COM AGN | -1.11 | -1.1 | 43.76 | 3.99 | 7.69 |
| 6961 | COM AGN | 0.63 | 0.6 | 44.09 | 4.85 | 7.66 |
| 7043 | COM AGN | -0.82 | -0.8 | 43.86 | 4.69 | 8.48 |
| 7450 | COM AGN | -0.61 | -0.6 | 43.73 | 4.36 | 7.60 |
| 7490 | COM AGN | -2.54 | -2.4 | 43.45 | 3.66 | 8.33 |
| 7632 | COM AGN | -1.78 | -1.7 | 43.17 | 4.07 | 7.60 |
| 7947 | COM AGN | -0.95 | -0.9 | 43.41 | 5.02 | 8.22 |
| 7977 | COM AGN | -1.56 | -1.5 | 44.09 | 3.58 | 8.18 |
| 8048 | COM AGN | -0.27 | -0.3 | 44.05 | 4.63 | 8.17 |
| 8144 | COM AGN | -1.99 | -1.8 | 44.19 | 3.30 | 8.43 |
| 8338 | COM AGN | -2.42 | -2.3 | 43.22 | 3.89 | 8.10 |
| 8355 | COM AGN | -1.08 | -1.1 | 43.36 | 5.04 | 8.30 |
| 8602 | COM AGN | -2.05 | -2.0 | 43.69 | 3.86 | 8.39 |
| 9123 | COM AGN | -1.66 | -1.6 | 43.93 | 3.60 | 8.07 |
| 9144 | COM AGN | -0.77 | -0.7 | 43.89 | 4.17 | 7.80 |
| 9201 | COM AGN | -2.97 | -2.8 | 43.38 | 3.56 | 8.49 |
| 9632 | COM AGN | -0.66 | -0.6 | 43.41 | 4.93 | 7.83 |
| 9660 | COM AGN | -1.39 | -1.4 | 43.11 | 4.57 | 7.66 |
| 9743 | COM AGN | -1.14 | -1.1 | 43.90 | 3.93 | 7.89 |
| 10149 | COM AGN | -2.67 | -2.3 | 44.70 | 2.61 | 9.10 |
| 10200 | COM AGN | -1.84 | -1.8 | 43.71 | 3.82 | 8.14 |
| 10388 | COM AGN | -1.48 | -1.4 | 43.60 | 4.01 | 7.83 |
| 10596 | COM AGN | -1.04 | -1.0 | 44.00 | 3.94 | 7.93 |
| 10748 | COM AGN | -1.34 | -1.3 | 44.01 | 3.84 | 8.15 |
| 10754 | COM AGN | -0.98 | -0.9 | 43.61 | 4.27 | 7.67 |
| 10900 | FRII | -0.32 | -0.2 | 46.03 | 2.37 | 8.77 |
| 10901 | FRII | -1.73 | -0.1 | 46.65 | 0.37 | 8.62 |

Table C.3: Eddington ratios for FRs and COM AGN (continued)

| ID | radio class | λ_r | λ_{rk} | $\log_{10}(L_{\text{jet}} / \text{erg s}^{-1})$ | L_X / L_{radio} | $\log_{10}(M_{\text{BH}} / M_{\odot})$ |
|-------|-------------|-------------|----------------|---|--------------------------|--|
| 10902 | FRII | -1.11 | 0.0 | 46.03 | 1.12 | 7.91 |
| 10903 | FRI | -1.82 | -1.0 | 45.35 | 1.75 | 8.31 |
| 10905 | FRII | -2.29 | -2.1 | 44.43 | 2.98 | 8.76 |
| 10906 | FRII | -2.18 | -1.0 | 45.49 | 1.35 | 8.41 |
| 10909 | FRII | -2.73 | -1.4 | 45.63 | 1.13 | 8.93 |
| 10910 | FRI/FRII | -3.57 | -1.7 | 44.97 | 0.91 | 8.60 |
| 10911 | FRII | -1.68 | -1.4 | 45.20 | 2.49 | 8.79 |
| 10912 | FRI | -2.64 | -2.2 | 44.44 | 2.65 | 8.76 |
| 10913 | FRI | -4.28 | -1.9 | 45.19 | 0.26 | 8.98 |
| 10914 | FRI/FRII | -2.52 | -1.2 | 45.33 | 1.27 | 8.42 |
| 10918 | FRII | -3.78 | -1.9 | 45.04 | 0.90 | 8.89 |
| 10919 | FRII | -0.73 | -0.4 | 45.63 | 2.27 | 8.30 |
| 10920 | FRII | -1.31 | -0.6 | 45.52 | 1.77 | 8.06 |
| 10923 | FRII | -2.31 | -1.0 | 45.98 | 1.04 | 8.93 |
| 10930 | FRII | -2.16 | -1.5 | 45.20 | 2.03 | 8.71 |
| 10933 | FRII | -3.73 | -1.7 | 45.19 | 0.68 | 8.83 |
| 10936 | FRI/FRII | -2.08 | -0.8 | 45.59 | 1.21 | 8.31 |
| 10940 | FRII | 0.64 | 0.6 | 44.25 | 4.66 | 7.69 |
| 10948 | FRII | -4.12 | -3.0 | 43.66 | 2.08 | 8.61 |
| 10949 | FRII | -2.45 | -1.8 | 44.94 | 2.11 | 8.70 |
| 10958 | FRI/FRII | -4.12 | -2.7 | 43.25 | 1.88 | 7.63 |
| 10962 | FRII | -2.40 | -0.1 | 46.23 | 0.03 | 8.25 |
| 10964 | FRI | -1.22 | -1.2 | 43.92 | 7.31 | 9.42 |

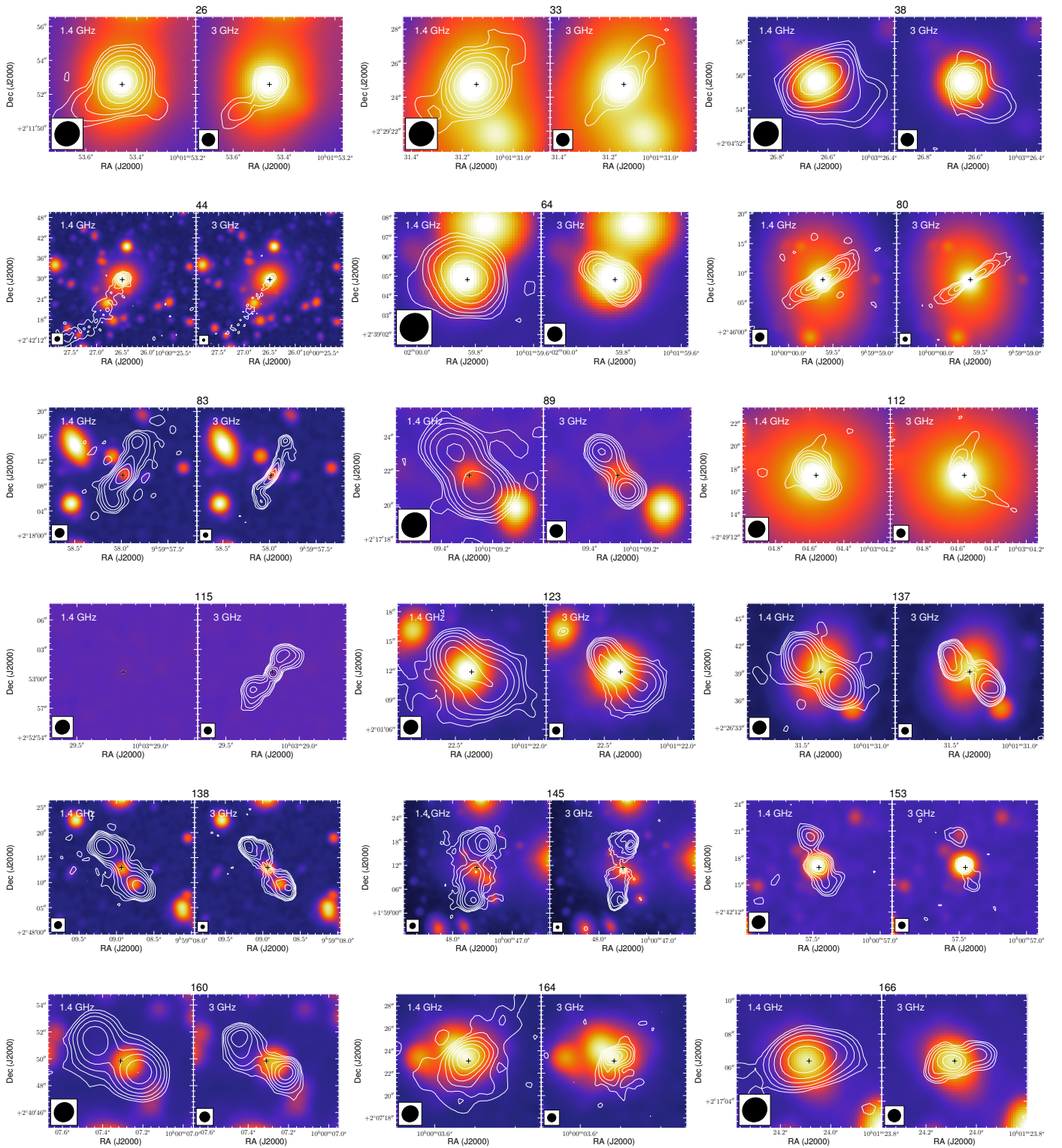


Fig. C.5: Set of overlays at 1.4 GHz (left) and 3 GHz (right) VLA-COSMOS for the FR objects in our sample, shown as white contours. The colourscale is the UltraVISTA stacked mosaic. Data for these sources are shown in Table C.1. Objects without 1.4 GHz or UltraVISTA maps lie in masked regions or outside the data coverage.

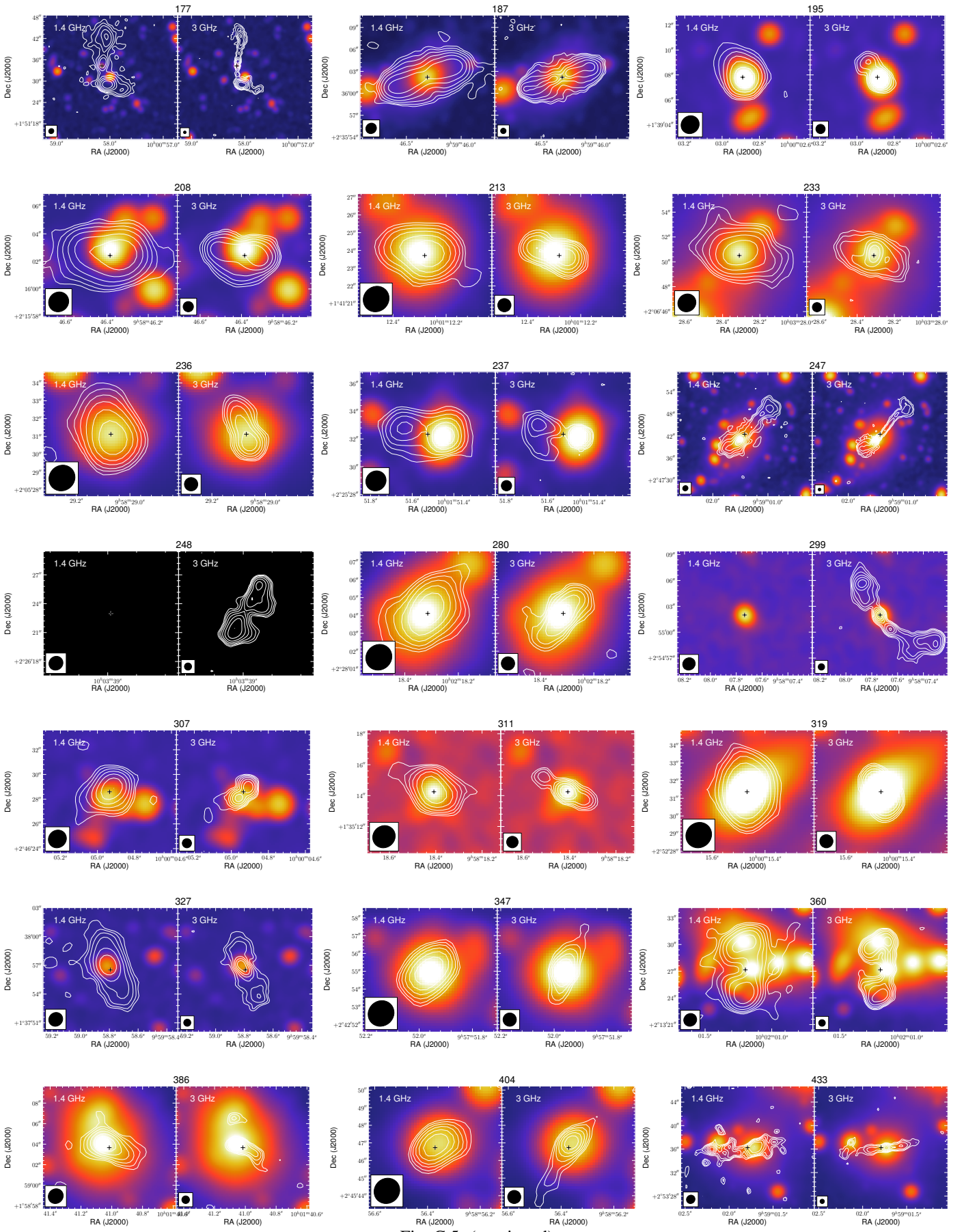


Fig. C.5: (continued)

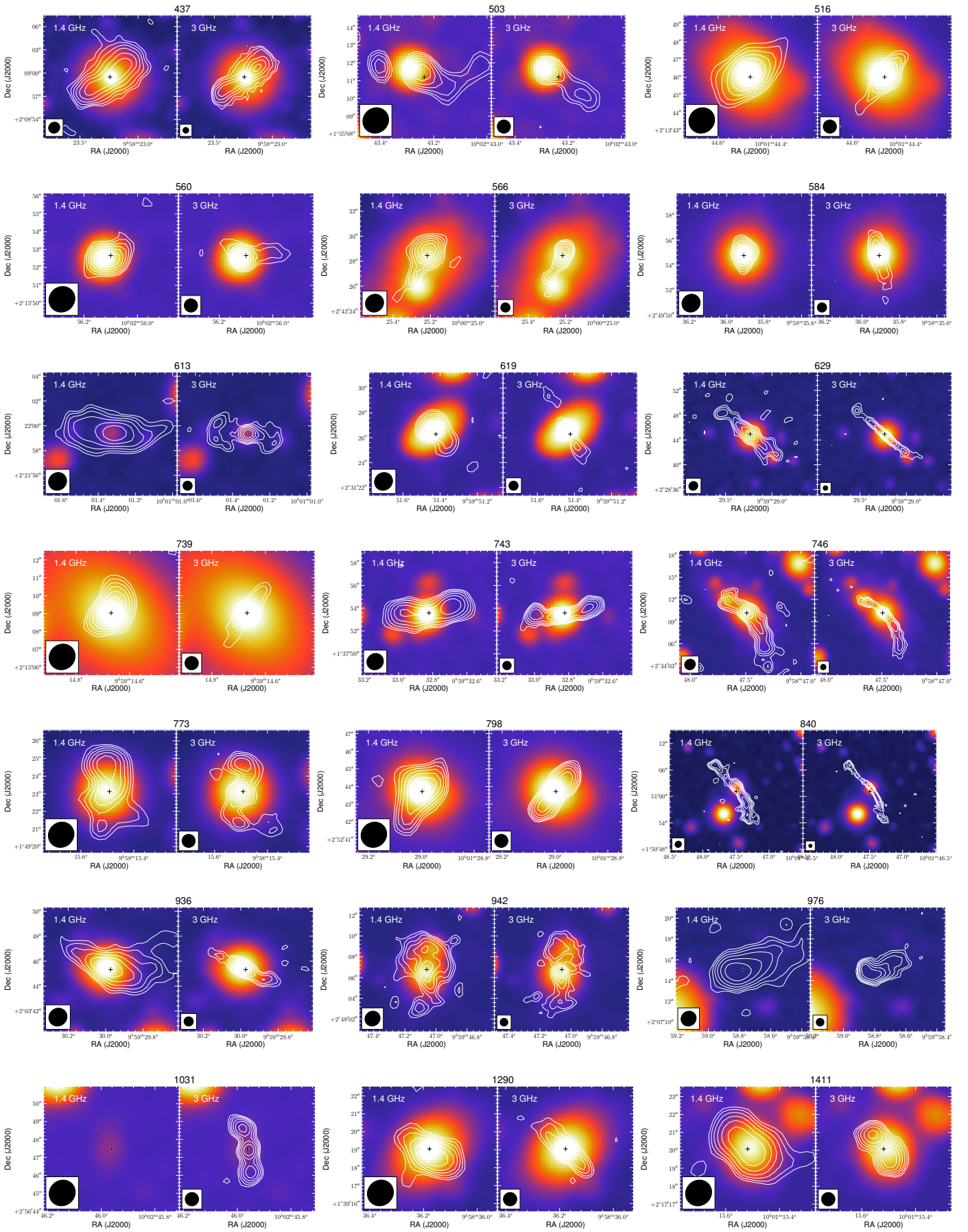
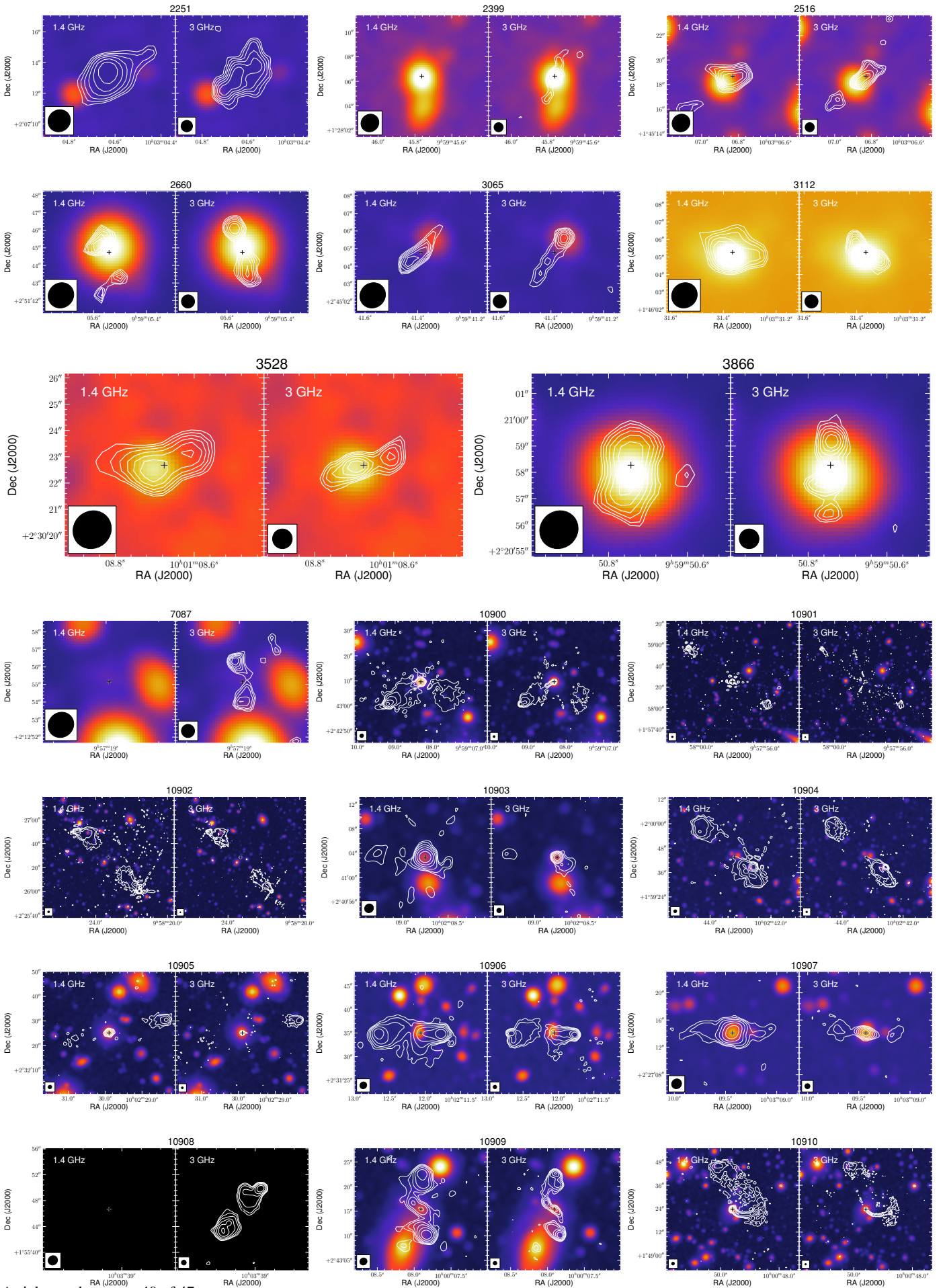


Fig. C.5: (continued)



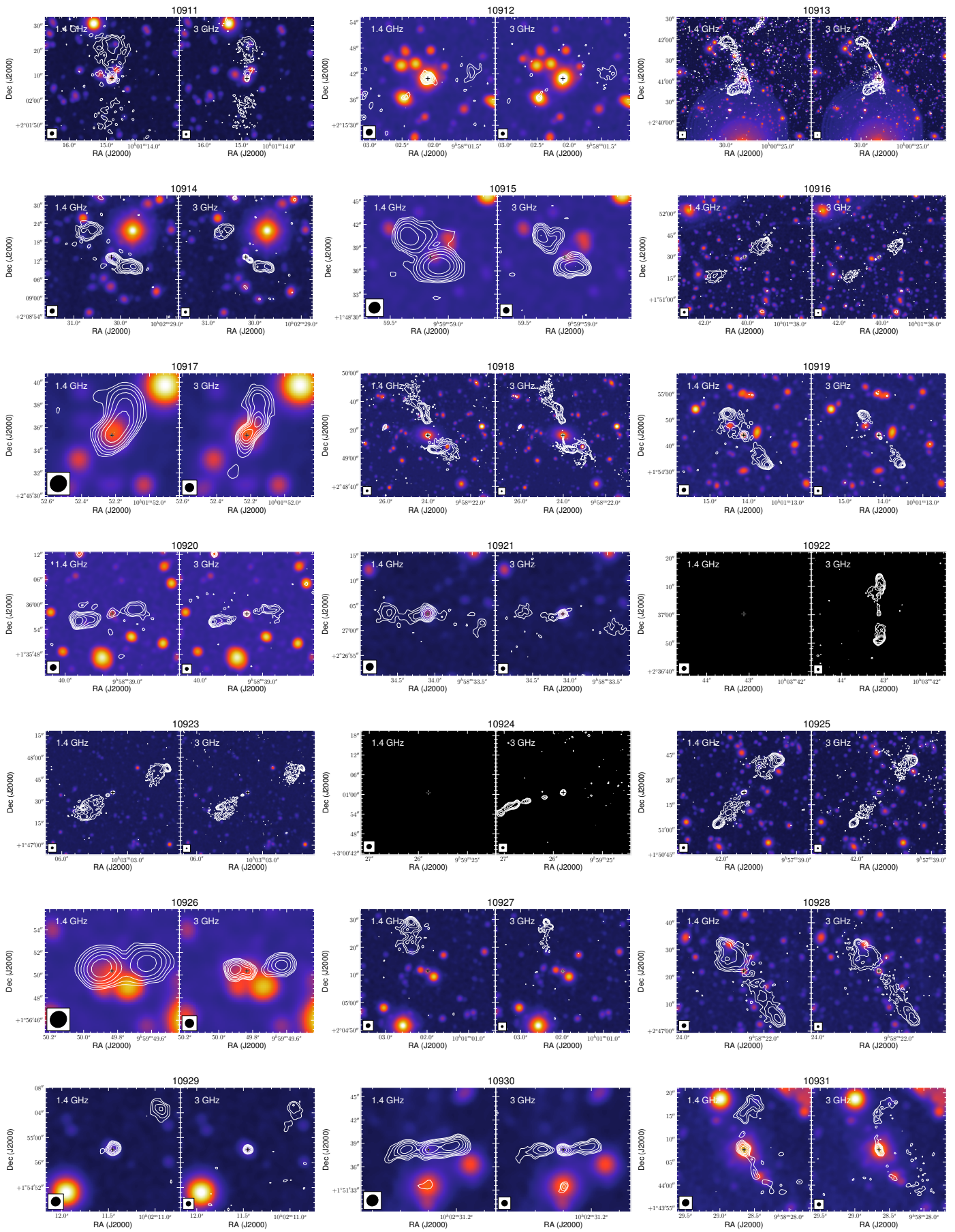


Fig. C.5: (continued)

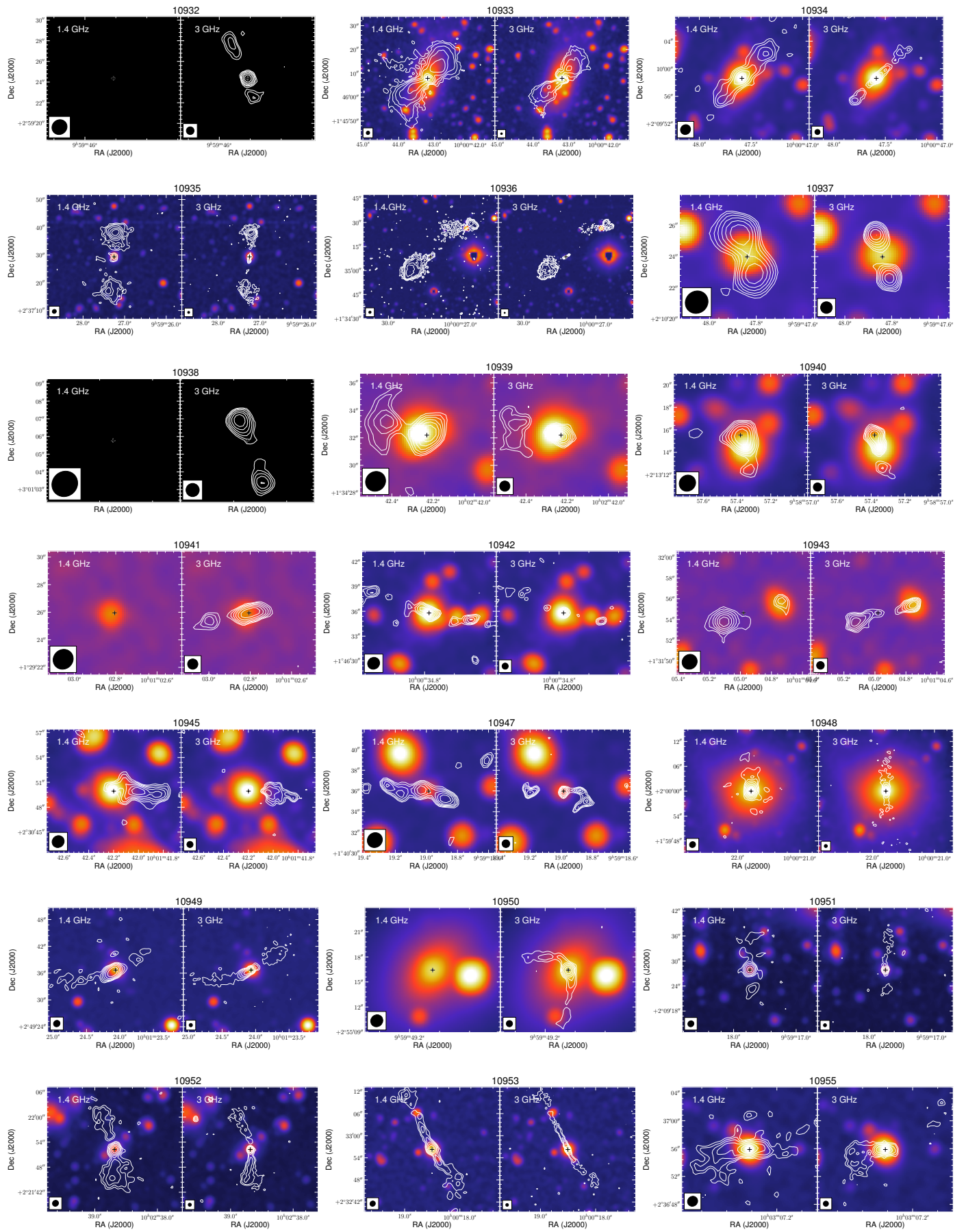


Fig. C.5: (continued)

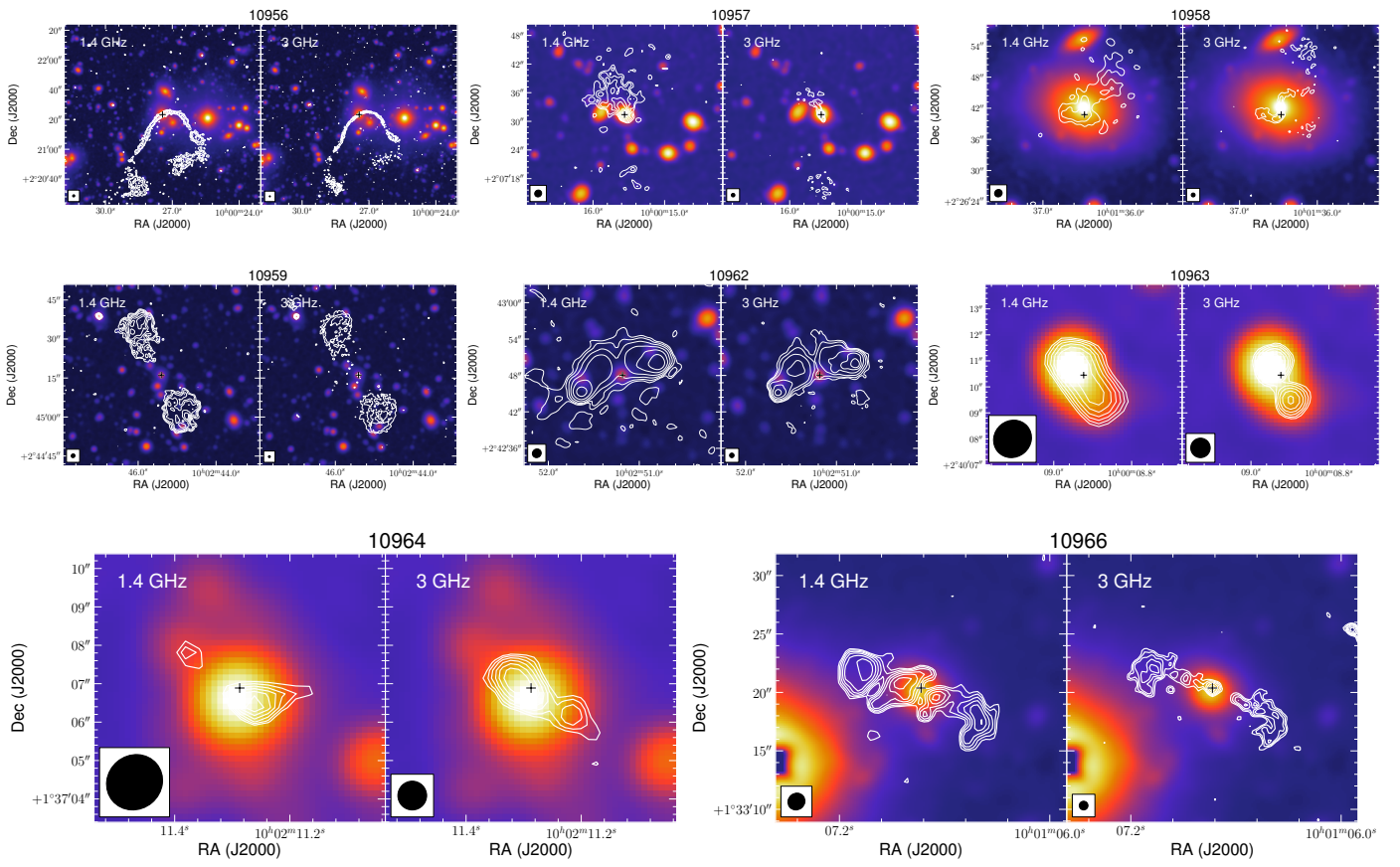


Fig. C.5: (continued)

Table C.4: Intrinsic radio sizes of COM AGN

| ID | D (kpc) | ID | D (kpc) | ID | D (kpc) | ID | D (kpc) |
|-----|------------|-----|------------|-----|------------|-----|------------|
| 1 | 0.0 | 105 | 0.5 | 219 | 0.6 | 345 | 0.5 |
| 2 | 0.0 | 106 | 1.4 | 224 | 0.6 | 346 | 1.1 |
| 3 | 0.0 | 108 | 0.0 | 226 | 0.8 | 350 | 7.8 |
| 5 | 0.9 | 109 | 0.7 | 227 | 0.0 | 352 | 0.9 |
| 6 | 3.0 | 114 | 0.7 | 229 | 4.8 | 353 | 1.7 |
| 7 | 4.4 | 119 | 0.7 | 231 | 1.3 | 356 | 1.4 |
| 8 | 0.0 | 120 | 1.4 | 235 | 4.0 | 357 | 2.9 |
| 16 | 7.9 | 121 | 0.7 | 240 | 0.6 | 358 | 1.3 |
| 17 | 0.0 | 122 | 0.9 | 241 | 0.7 | 359 | 1.5 |
| 18 | 0.4 | 125 | 1.0 | 245 | 0.9 | 361 | 1.6 |
| 19 | 0.0 | 126 | 0.7 | 251 | 0.9 | 363 | 1.4 |
| 22 | 0.9 | 127 | 1.2 | 252 | 0.0 | 364 | 1.6 |
| 23 | 0.0 | 128 | 1.1 | 256 | 0.0 | 366 | 2.1 |
| 25 | 0.0 | 129 | 1.1 | 257 | 2.0 | 367 | 1.4 |
| 29 | 2.7 | 130 | 0.0 | 261 | 0.0 | 369 | 0.0 |
| 30 | 0.0 | 131 | 1.0 | 262 | 0.0 | 370 | 1.7 |
| 31 | 1.4 | 132 | 0.0 | 264 | 0.0 | 374 | 1.2 |
| 35 | 0.6 | 134 | 0.0 | 265 | 1.2 | 375 | 0.0 |
| 37 | 0.8 | 135 | 1.0 | 267 | 2.1 | 376 | 0.6 |
| 39 | 3.1 | 136 | 1.0 | 268 | 0.9 | 377 | 1.8 |
| 40 | 3.6 | 139 | 0.0 | 269 | 0.9 | 378 | 0.7 |
| 41 | 1.0 | 140 | 0.0 | 270 | 0.0 | 380 | 1.3 |
| 42 | 0.0 | 142 | 0.0 | 272 | 0.0 | 381 | 0.0 |
| 43 | 0.7 | 143 | 1.5 | 273 | 0.8 | 383 | 2.1 |
| 45 | 0.0 | 149 | 0.0 | 275 | 1.1 | 384 | 8.1 |
| 46 | 0.0 | 152 | 7.7 | 276 | 1.1 | 387 | 0.0 |
| 47 | 0.0 | 155 | 7.3 | 277 | 1.7 | 389 | 0.0 |
| 50 | 1.0 | 156 | 0.0 | 278 | 0.4 | 390 | 0.0 |
| 51 | 0.0 | 157 | 2.0 | 279 | 0.0 | 392 | 0.0 |
| 52 | 0.0 | 158 | 0.0 | 282 | 0.8 | 396 | 2.8 |
| 53 | 0.9 | 162 | 2.8 | 284 | 0.0 | 397 | 1.7 |
| 55 | 1.2 | 163 | 4.5 | 285 | 1.6 | 398 | 0.0 |
| 56 | 1.8 | 165 | 0.8 | 286 | 1.7 | 401 | 0.0 |
| 57 | 5.6 | 167 | 0.0 | 287 | 0.0 | 402 | 1.6 |
| 58 | 0.0 | 171 | 0.9 | 289 | 1.2 | 405 | 0.0 |
| 61 | 0.0 | 172 | 1.0 | 290 | 2.4 | 406 | 0.4 |
| 63 | 1.0 | 173 | 3.8 | 291 | 1.4 | 407 | 1.6 |
| 65 | 0.0 | 175 | 0.8 | 293 | 1.5 | 408 | 0.0 |
| 66 | 5.1 | 178 | 2.2 | 294 | 1.1 | 409 | 0.8 |
| 67 | 0.6 | 180 | 7.5 | 295 | 4.5 | 411 | 0.0 |
| 68 | 0.0 | 182 | 1.0 | 296 | 1.1 | 413 | 0.0 |
| 70 | 1.0 | 183 | 0.2 | 297 | 4.2 | 415 | 0.0 |
| 72 | 0.0 | 184 | 0.0 | 300 | 1.6 | 416 | 3.3 |
| 73 | 1.0 | 188 | 0.9 | 302 | 0.0 | 422 | 0.0 |
| 74 | 1.2 | 190 | 0.5 | 303 | 2.8 | 425 | 1.2 |
| 75 | 1.0 | 191 | 0.0 | 312 | 1.3 | 428 | 1.3 |
| 76 | 1.4 | 193 | 0.9 | 314 | 8.0 | 432 | 1.0 |
| 79 | 2.0 | 194 | 1.3 | 315 | 2.6 | 435 | 0.0 |
| 81 | 1.3 | 196 | 0.0 | 316 | 0.9 | 438 | 1.4 |
| 84 | 0.0 | 197 | 0.0 | 318 | 0.0 | 439 | 0.0 |
| 85 | 1.0 | 198 | 6.7 | 322 | 0.0 | 440 | 1.8 |
| 88 | 0.0 | 201 | 0.0 | 323 | 0.6 | 443 | 3.7 |
| 90 | 1.6 | 205 | 1.0 | 325 | 1.7 | 444 | 13.6 |
| 91 | 1.1 | 206 | 0.0 | 326 | 1.5 | 445 | 0.0 |
| 92 | 0.9 | 210 | 0.0 | 330 | 0.0 | 446 | 3.8 |
| 93 | 1.0 | 211 | 0.0 | 333 | 1.0 | 449 | 0.0 |
| 98 | 2.7 | 212 | 0.5 | 339 | 2.9 | 450 | 0.0 |
| 99 | 0.0 | 215 | 6.2 | 341 | 2.9 | 452 | 1.9 |
| 102 | 1.9 | 217 | 1.3 | 342 | 8.2 | 454 | 5.2 |
| 103 | 0.0 | 218 | 0.8 | 344 | 0.0 | 455 | 0.9 |

Table C.4: Intrinsic radio sizes of COM AGN (continued)

| ID | D (kpc) | ID | D (kpc) | ID | D (kpc) | ID | D (kpc) |
|-----|------------|-----|------------|-----|------------|------|------------|
| 456 | 1.9 | 603 | 2.4 | 723 | 1.4 | 862 | 0.0 |
| 457 | 0.0 | 605 | 1.8 | 724 | 2.3 | 863 | 2.2 |
| 458 | 0.0 | 608 | 1.0 | 725 | 2.2 | 869 | 0.0 |
| 460 | 3.4 | 611 | 1.6 | 729 | 0.0 | 872 | 0.0 |
| 461 | 2.3 | 612 | 1.0 | 730 | 2.2 | 876 | 0.0 |
| 468 | 10.2 | 614 | 0.0 | 734 | 2.3 | 877 | 2.0 |
| 470 | 1.5 | 615 | 1.8 | 736 | 2.2 | 880 | 3.5 |
| 472 | 1.3 | 616 | 0.8 | 738 | 0.0 | 882 | 2.5 |
| 475 | 2.2 | 617 | 0.0 | 740 | 1.9 | 883 | 3.8 |
| 479 | 2.4 | 618 | 0.0 | 742 | 1.6 | 884 | 3.7 |
| 480 | 0.0 | 620 | 2.0 | 745 | 2.4 | 887 | 6.7 |
| 481 | 0.0 | 621 | 1.2 | 747 | 0.0 | 888 | 2.0 |
| 482 | 1.7 | 623 | 1.3 | 748 | 2.2 | 889 | 1.4 |
| 486 | 0.0 | 624 | 1.4 | 749 | 0.0 | 890 | 2.7 |
| 488 | 0.0 | 625 | 2.4 | 751 | 2.4 | 891 | 4.6 |
| 491 | 2.1 | 626 | 3.0 | 752 | 2.1 | 894 | 1.8 |
| 492 | 1.8 | 627 | 0.0 | 754 | 1.2 | 898 | 0.0 |
| 493 | 3.1 | 630 | 2.1 | 755 | 1.0 | 899 | 0.0 |
| 494 | 1.5 | 631 | 2.4 | 758 | 0.0 | 900 | 0.0 |
| 498 | 2.0 | 633 | 1.4 | 759 | 0.0 | 904 | 0.0 |
| 499 | 1.3 | 635 | 2.9 | 766 | 0.0 | 906 | 4.8 |
| 502 | 0.0 | 638 | 1.4 | 772 | 2.5 | 909 | 1.1 |
| 506 | 0.0 | 639 | 0.0 | 774 | 0.0 | 910 | 3.1 |
| 507 | 2.3 | 643 | 0.0 | 776 | 1.7 | 915 | 0.0 |
| 508 | 0.6 | 644 | 0.0 | 778 | 0.0 | 919 | 3.9 |
| 510 | 1.5 | 645 | 0.0 | 782 | 0.0 | 925 | 0.0 |
| 512 | 1.6 | 646 | 4.2 | 783 | 0.0 | 931 | 1.6 |
| 514 | 1.3 | 648 | 0.0 | 788 | 2.8 | 932 | 0.0 |
| 515 | 0.0 | 655 | 1.7 | 789 | 0.0 | 934 | 2.6 |
| 517 | 2.8 | 658 | 1.5 | 791 | 0.0 | 935 | 0.0 |
| 520 | 2.0 | 662 | 0.0 | 792 | 0.0 | 937 | 0.9 |
| 521 | 8.0 | 663 | 2.0 | 795 | 0.0 | 945 | 0.0 |
| 522 | 0.0 | 664 | 5.8 | 796 | 2.5 | 947 | 0.0 |
| 524 | 1.3 | 666 | 0.0 | 797 | 2.9 | 949 | 0.0 |
| 526 | 0.0 | 668 | 0.0 | 802 | 0.0 | 951 | 3.2 |
| 528 | 1.5 | 671 | 1.8 | 805 | 0.0 | 953 | 3.6 |
| 529 | 0.0 | 672 | 1.4 | 807 | 2.7 | 954 | 0.0 |
| 535 | 7.0 | 676 | 0.0 | 809 | 2.0 | 958 | 4.5 |
| 537 | 0.0 | 678 | 1.4 | 813 | 8.1 | 959 | 1.1 |
| 538 | 1.5 | 680 | 0.0 | 815 | 0.0 | 960 | 1.5 |
| 539 | 0.0 | 681 | 2.0 | 816 | 1.3 | 962 | 2.5 |
| 545 | 2.2 | 682 | 0.0 | 818 | 3.6 | 963 | 0.0 |
| 546 | 2.0 | 683 | 0.0 | 821 | 0.0 | 974 | 0.0 |
| 547 | 0.7 | 684 | 2.7 | 822 | 0.0 | 978 | 0.0 |
| 551 | 1.7 | 686 | 4.5 | 824 | 0.0 | 982 | 1.9 |
| 556 | 2.3 | 688 | 4.1 | 826 | 2.5 | 984 | 0.0 |
| 557 | 2.8 | 689 | 2.1 | 828 | 0.0 | 985 | 1.5 |
| 559 | 12.2 | 690 | 2.3 | 829 | 1.8 | 986 | 1.8 |
| 563 | 1.4 | 695 | 2.1 | 830 | 1.6 | 987 | 0.8 |
| 567 | 0.0 | 696 | 1.4 | 832 | 0.0 | 993 | 2.5 |
| 568 | 0.0 | 701 | 0.0 | 833 | 2.1 | 994 | 5.3 |
| 572 | 3.0 | 706 | 1.7 | 834 | 1.6 | 995 | 1.2 |
| 577 | 12.0 | 707 | 2.6 | 837 | 1.3 | 996 | 2.0 |
| 580 | 1.9 | 708 | 0.0 | 839 | 0.0 | 998 | 2.4 |
| 586 | 0.0 | 714 | 4.8 | 842 | 0.0 | 999 | 1.8 |
| 589 | 2.2 | 715 | 2.5 | 845 | 2.2 | 1000 | 1.8 |
| 594 | 0.0 | 717 | 0.0 | 846 | 1.3 | 1004 | 0.0 |
| 595 | 0.0 | 718 | 1.6 | 852 | 0.0 | 1011 | 3.9 |
| 598 | 0.0 | 719 | 4.7 | 854 | 0.0 | 1012 | 1.1 |
| 601 | 1.8 | 722 | 2.2 | 855 | 0.0 | 1017 | 0.0 |

Notes. Intrinsic sizes are estimated after using `pyBDSF` (Mohan & Rafferty, 2015) on the 3 GHz mosaic (Jiménez-Andrade et al., 2019).

Table C.4: Intrinsic radio sizes of COM AGN (continued)

Table C.4: Intrinsic radio sizes of COM AGN (continued)

| ID | <i>D</i> (kpc) |
|------|-------------------|------|-------------------|------|-------------------|------|-------------------|------|-------------------|------|-------------------|------|-------------------|------|-------------------|
| 1020 | 0.0 | 1216 | 8.1 | 1408 | 3.4 | 1607 | 2.0 | 1829 | 9.1 | 2052 | 0.0 | 2297 | 3.2 | 2581 | 2.4 |
| 1024 | 0.0 | 1222 | 2.2 | 1409 | 2.9 | 1608 | 0.0 | 1830 | 2.7 | 2053 | 0.0 | 2307 | 2.8 | 2585 | 3.4 |
| 1026 | 2.7 | 1224 | 0.0 | 1413 | 3.2 | 1620 | 0.0 | 1836 | 1.5 | 2054 | 0.0 | 2312 | 0.0 | 2594 | 0.0 |
| 1029 | 0.0 | 1225 | 5.1 | 1415 | 1.8 | 1631 | 3.3 | 1838 | 2.4 | 2060 | 0.0 | 2320 | 0.0 | 2596 | 4.5 |
| 1030 | 1.8 | 1228 | 2.4 | 1421 | 1.6 | 1639 | 0.0 | 1845 | 4.9 | 2067 | 1.2 | 2321 | 0.0 | 2602 | 0.0 |
| 1035 | 3.3 | 1230 | 2.2 | 1423 | 0.0 | 1643 | 3.1 | 1847 | 1.5 | 2073 | 2.9 | 2329 | 2.6 | 2604 | 0.0 |
| 1040 | 0.0 | 1231 | 0.0 | 1434 | 2.9 | 1644 | 1.9 | 1849 | 0.0 | 2074 | 0.0 | 2330 | 0.0 | 2614 | 2.6 |
| 1041 | 1.5 | 1235 | 0.0 | 1435 | 3.4 | 1645 | 1.6 | 1852 | 7.3 | 2076 | 2.4 | 2335 | 2.6 | 2617 | 0.0 |
| 1043 | 1.8 | 1237 | 3.2 | 1438 | 2.1 | 1647 | 4.4 | 1857 | 3.4 | 2078 | 2.5 | 2336 | 6.3 | 2619 | 0.0 |
| 1048 | 0.0 | 1245 | 2.0 | 1441 | 0.0 | 1651 | 0.0 | 1859 | 2.7 | 2084 | 4.1 | 2345 | 0.0 | 2627 | 1.6 |
| 1049 | 0.0 | 1249 | 5.3 | 1446 | 7.1 | 1663 | 2.7 | 1862 | 4.5 | 2085 | 0.0 | 2354 | 5.2 | 2628 | 4.8 |
| 1053 | 1.6 | 1251 | 1.9 | 1448 | 5.4 | 1665 | 2.9 | 1864 | 4.5 | 2098 | 0.0 | 2356 | 0.0 | 2631 | 0.0 |
| 1056 | 2.4 | 1259 | 1.5 | 1450 | 2.2 | 1667 | 0.0 | 1865 | 2.6 | 2101 | 4.2 | 2369 | 0.0 | 2632 | 0.0 |
| 1060 | 2.6 | 1260 | 0.0 | 1455 | 0.0 | 1669 | 0.0 | 1866 | 3.1 | 2104 | 3.7 | 2371 | 4.3 | 2634 | 0.0 |
| 1061 | 0.0 | 1265 | 0.0 | 1462 | 3.3 | 1675 | 1.6 | 1869 | 4.0 | 2114 | 2.1 | 2374 | 5.2 | 2635 | 3.4 |
| 1063 | 0.0 | 1283 | 0.0 | 1463 | 0.0 | 1678 | 4.0 | 1870 | 3.5 | 2115 | 5.9 | 2380 | 5.3 | 2641 | 2.8 |
| 1071 | 0.0 | 1284 | 4.5 | 1464 | 3.5 | 1684 | 2.7 | 1871 | 5.0 | 2116 | 0.0 | 2381 | 2.7 | 2653 | 2.5 |
| 1072 | 5.3 | 1285 | 1.4 | 1466 | 0.0 | 1687 | 3.2 | 1872 | 3.1 | 2119 | 0.0 | 2383 | 4.2 | 2659 | 1.7 |
| 1076 | 0.0 | 1291 | 1.3 | 1474 | 0.0 | 1688 | 0.0 | 1882 | 3.1 | 2120 | 0.0 | 2390 | 0.0 | 2678 | 3.3 |
| 1078 | 0.0 | 1298 | 0.0 | 1477 | 2.0 | 1690 | 6.1 | 1883 | 0.0 | 2133 | 3.4 | 2391 | 4.5 | 2679 | 3.3 |
| 1080 | 0.0 | 1301 | 6.4 | 1482 | 3.1 | 1696 | 0.0 | 1891 | 3.0 | 2141 | 1.2 | 2398 | 0.0 | 2681 | 5.1 |
| 1082 | 3.1 | 1304 | 0.5 | 1486 | 2.6 | 1697 | 0.0 | 1895 | 0.0 | 2143 | 3.6 | 2407 | 2.9 | 2685 | 0.0 |
| 1085 | 0.5 | 1305 | 0.0 | 1489 | 2.8 | 1698 | 0.0 | 1896 | 2.6 | 2145 | 3.3 | 2410 | 0.0 | 2687 | 2.9 |
| 1087 | 2.2 | 1306 | 0.0 | 1495 | 0.0 | 1701 | 2.1 | 1903 | 3.4 | 2155 | 2.9 | 2417 | 4.5 | 2688 | 2.7 |
| 1094 | 2.0 | 1310 | 2.9 | 1496 | 3.8 | 1703 | 0.0 | 1911 | 0.0 | 2159 | 4.6 | 2421 | 3.7 | 2693 | 4.7 |
| 1100 | 0.7 | 1312 | 0.0 | 1501 | 2.2 | 1704 | 3.3 | 1913 | 2.1 | 2163 | 3.1 | 2434 | 0.0 | 2700 | 0.0 |
| 1106 | 1.9 | 1315 | 2.9 | 1502 | 2.7 | 1710 | 0.0 | 1914 | 0.0 | 2178 | 3.0 | 2438 | 2.9 | 2710 | 4.2 |
| 1112 | 0.0 | 1317 | 0.0 | 1504 | 2.3 | 1711 | 2.1 | 1919 | 0.0 | 2181 | 2.6 | 2440 | 2.1 | 2713 | 5.6 |
| 1118 | 0.0 | 1323 | 0.0 | 1508 | 2.5 | 1714 | 0.0 | 1920 | 5.3 | 2183 | 4.4 | 2456 | 0.0 | 2716 | 4.3 |
| 1120 | 0.0 | 1326 | 1.2 | 1509 | 0.0 | 1716 | 8.5 | 1922 | 2.4 | 2184 | 5.0 | 2458 | 4.8 | 2727 | 4.0 |
| 1121 | 2.1 | 1331 | 0.0 | 1521 | 0.0 | 1722 | 3.4 | 1929 | 0.0 | 2186 | 1.4 | 2460 | 3.3 | 2732 | 4.0 |
| 1123 | 2.2 | 1332 | 0.0 | 1523 | 3.0 | 1723 | 2.4 | 1933 | 0.0 | 2187 | 3.1 | 2463 | 0.0 | 2733 | 4.2 |
| 1126 | 2.3 | 1337 | 0.0 | 1526 | 3.9 | 1724 | 2.4 | 1938 | 0.0 | 2205 | 2.3 | 2464 | 3.7 | 2736 | 2.5 |
| 1130 | 0.0 | 1338 | 2.8 | 1530 | 2.2 | 1726 | 3.0 | 1939 | 0.0 | 2206 | 2.5 | 2465 | 0.0 | 2737 | 3.1 |
| 1136 | 0.0 | 1342 | 1.9 | 1533 | 7.2 | 1732 | 3.6 | 1952 | 3.9 | 2207 | 4.6 | 2471 | 2.7 | 2744 | 3.9 |
| 1137 | 1.9 | 1353 | 3.3 | 1535 | 1.8 | 1739 | 2.6 | 1954 | 0.0 | 2214 | 7.2 | 2473 | 2.2 | 2746 | 7.3 |
| 1138 | 3.3 | 1355 | 2.2 | 1538 | 2.0 | 1743 | 2.5 | 1957 | 0.0 | 2215 | 0.0 | 2479 | 1.9 | 2749 | 0.0 |
| 1139 | 3.5 | 1357 | 3.1 | 1539 | 3.3 | 1744 | 2.5 | 1962 | 0.0 | 2216 | 3.0 | 2485 | 4.1 | 2754 | 4.1 |
| 1145 | 2.9 | 1359 | 0.0 | 1542 | 0.0 | 1745 | 3.3 | 1963 | 2.6 | 2225 | 1.8 | 2499 | 4.1 | 2758 | 3.5 |
| 1149 | 2.2 | 1362 | 0.0 | 1545 | 4.7 | 1754 | 0.0 | 1969 | 2.6 | 2236 | 3.6 | 2502 | 0.0 | 2759 | 2.5 |
| 1151 | 1.5 | 1363 | 1.5 | 1548 | 2.2 | 1757 | 1.8 | 1971 | 4.7 | 2244 | 0.0 | 2508 | 0.0 | 2760 | 4.7 |
| 1152 | 3.7 | 1364 | 3.2 | 1552 | 0.0 | 1761 | 2.1 | 1983 | 0.0 | 2245 | 3.2 | 2511 | 2.0 | 2774 | 0.0 |
| 1153 | 3.2 | 1365 | 0.0 | 1560 | 1.3 | 1768 | 0.0 | 1984 | 0.0 | 2247 | 0.0 | 2517 | 6.2 | 2782 | 0.0 |
| 1159 | 0.0 | 1367 | 0.0 | 1564 | 4.1 | 1769 | 6.4 | 1989 | 1.9 | 2248 | 2.3 | 2518 | 0.4 | 2783 | 4.5 |
| 1163 | 3.0 | 1370 | 0.0 | 1565 | 0.0 | 1777 | 0.0 | 1990 | 6.7 | 2252 | 0.0 | 2531 | 0.0 | 2788 | 6.7 |
| 1164 | 2.5 | 1371 | 0.0 | 1572 | 3.4 | 1782 | 5.2 | 1994 | 2.7 | 2254 | 0.0 | 2534 | 0.0 | 2791 | 3.7 |
| 1165 | 0.9 | 1377 | 2.1 | 1574 | 0.0 | 1786 | 1.8 | 1995 | 0.0 | 2257 | 3.7 | 2536 | 0.0 | 2799 | 3.0 |
| 1168 | 2.2 | 1382 | 1.8 | 1575 | 0.1 | 1789 | 1.9 | 1997 | 0.0 | 2262 | 1.7 | 2539 | 2.0 | 2800 | 3.2 |
| 1173 | 0.0 | 1384 | 2.2 | 1576 | 2.3 | 1792 | 0.0 | 2005 | 0.0 | 2267 | 2.1 | 2540 | 0.0 | 2807 | 3.5 |
| 1175 | 0.0 | 1391 | 0.0 | 1579 | 4.4 | 1795 | 0.0 | 2021 | 2.8 | 2278 | 0.0 | 2542 | 2.2 | 2811 | 3.3 |
| 1179 | 2.3 | 1393 | 1.7 | 1580 | 4.2 | 1798 | 2.3 | 2028 | 3.2 | 2279 | 0.0 | 2543 | 3.5 | 2818 | 0.0 |
| 1182 | 4.4 | 1396 | 1.5 | 1592 | 0.0 | 1801 | 2.1 | 2029 | 2.8 | 2282 | 3.6 | 2546 | 2.8 | 2824 | 0.0 |
| 1185 | 0.0 | 1397 | 2.5 | 1593 | 0.0 | 1803 | 1.8 | 2033 | 3.5 | 2284 | 1.7 | 2550 | 2.7 | 2828 | 4.1 |
| 1189 | 2.0 | 1398 | 2.9 | 1596 | 0.0 | 1809 | 2.4 | 2036 | 0.0 | 2286 | 2.3 | 2553 | 3.3 | 2831 | 1.8 |
| 1193 | 2.5 | 1399 | 0.0 | 1598 | 0.0 | 1814 | 0.0 | 2039 | 2.0 | 2287 | 1.4 | 2562 | 2.9 | 2832 | 2.6 |
| 1195 | 0.0 | 1401 | 3.1 | 1599 | 2.1 | 1815 | 3.1 | 2044 | 3.0 | 2288 | 2.6 | 2567 | 0.0 | 2834 | 13.6 |
| 1199 | 0.0 | 1402 | 0.0 | 1600 | 3.2 | 1818 | 0.0 | 2046 | 2.6 | 2289 | 4.2 | 2569 | 2.6 | 2838 | 0.0 |
| 1205 | 1.9 | 1403 | 2.1 | 1604 | 0.0 | 1823 | 2.2 | 2047 | 4.8 | 2291 | 0.0 | 2572 | 1.6 | 2840 | 1.3 |
| 1209 | 2.8 | 1404 | 2.9 | 1605 | 0.0 | 1824 | 0.0 | 2049 | 6.0 | 2292 | 3.0 | 2575 | 0.0 | 2843 | 5.5 |
| 1213 | 0.0 | 1406 | 4.1 | 1606 | 1.7 | 1826 | 3.7 | 2051 | 3.1 | 2296 | 4.2 | 2576 | 6.4 | 2847 | 1.0 |

Table C.4: Intrinsic radio sizes of COM AGN (continued)

| ID | D (kpc) | ID | D (kpc) | ID | D (kpc) | ID | D (kpc) |
|------|------------|------|------------|------|------------|------|------------|
| 2853 | 0.0 | 3151 | 0.0 | 3439 | 9.6 | 3844 | 0.0 |
| 2866 | 4.9 | 3161 | 0.0 | 3444 | 7.5 | 3850 | 3.2 |
| 2867 | 1.0 | 3163 | 0.0 | 3445 | 0.0 | 3853 | 2.4 |
| 2876 | 0.0 | 3165 | 4.7 | 3449 | 4.2 | 3862 | 3.4 |
| 2877 | 0.0 | 3172 | 2.7 | 3461 | 0.0 | 3869 | 4.4 |
| 2883 | 0.0 | 3182 | 5.5 | 3471 | 2.5 | 3871 | 3.8 |
| 2886 | 0.0 | 3196 | 0.0 | 3487 | 0.0 | 3880 | 7.3 |
| 2887 | 5.4 | 3197 | 3.2 | 3489 | 3.5 | 3888 | 3.9 |
| 2906 | 0.0 | 3203 | 7.1 | 3501 | 4.0 | 3889 | 0.0 |
| 2909 | 3.6 | 3205 | 0.0 | 3503 | 2.4 | 3895 | 0.0 |
| 2922 | 3.7 | 3213 | 0.0 | 3509 | 0.0 | 3896 | 3.8 |
| 2945 | 0.0 | 3215 | 4.1 | 3515 | 5.0 | 3897 | 2.9 |
| 2948 | 3.7 | 3216 | 0.0 | 3516 | 2.6 | 3905 | 5.6 |
| 2960 | 3.7 | 3220 | 3.6 | 3524 | 0.0 | 3909 | 13.8 |
| 2961 | 3.4 | 3221 | 0.0 | 3525 | 5.2 | 3912 | 4.1 |
| 2964 | 3.8 | 3223 | 0.0 | 3543 | 2.7 | 3918 | 1.4 |
| 2966 | 2.6 | 3225 | 0.0 | 3549 | 3.2 | 3919 | 2.8 |
| 2969 | 0.0 | 3230 | 3.2 | 3554 | 3.0 | 3921 | 2.2 |
| 2982 | 4.6 | 3233 | 3.6 | 3555 | 2.5 | 3922 | 0.0 |
| 2987 | 0.0 | 3236 | 4.0 | 3561 | 3.2 | 3926 | 4.1 |
| 2996 | 4.6 | 3247 | 6.4 | 3573 | 0.0 | 3927 | 4.2 |
| 3002 | 7.2 | 3251 | 5.1 | 3575 | 0.0 | 3943 | 4.6 |
| 3003 | 4.0 | 3252 | 4.5 | 3576 | 4.1 | 3944 | 4.5 |
| 3013 | 0.0 | 3255 | 5.0 | 3581 | 0.0 | 3964 | 0.0 |
| 3024 | 0.0 | 3259 | 0.0 | 3587 | 3.8 | 3968 | 2.8 |
| 3025 | 0.0 | 3262 | 0.0 | 3589 | 3.2 | 3975 | 0.0 |
| 3027 | 3.8 | 3265 | 0.0 | 3597 | 4.5 | 3985 | 0.0 |
| 3031 | 2.5 | 3276 | 2.7 | 3618 | 0.0 | 3987 | 4.3 |
| 3035 | 2.4 | 3281 | 4.7 | 3623 | 0.0 | 3992 | 4.0 |
| 3040 | 3.9 | 3284 | 9.3 | 3639 | 3.7 | 4000 | 1.3 |
| 3041 | 0.0 | 3295 | 0.0 | 3643 | 0.0 | 4043 | 0.0 |
| 3046 | 4.4 | 3298 | 3.7 | 3646 | 0.0 | 4076 | 4.2 |
| 3047 | 3.4 | 3301 | 2.9 | 3648 | 3.1 | 4084 | 6.4 |
| 3049 | 4.7 | 3307 | 0.0 | 3651 | 5.3 | 4090 | 3.9 |
| 3050 | 0.0 | 3317 | 1.5 | 3655 | 4.0 | 4096 | 3.7 |
| 3052 | 0.0 | 3318 | 0.0 | 3660 | 4.0 | 4105 | 4.5 |
| 3054 | 0.0 | 3322 | 3.8 | 3669 | 4.3 | 4118 | 4.8 |
| 3056 | 3.8 | 3325 | 1.7 | 3670 | 5.0 | 4131 | 5.9 |
| 3061 | 0.0 | 3335 | 3.2 | 3675 | 0.0 | 4136 | 0.0 |
| 3063 | 7.2 | 3340 | 0.0 | 3691 | 4.9 | 4138 | 9.4 |
| 3071 | 2.9 | 3345 | 0.0 | 3702 | 4.3 | 4142 | 4.7 |
| 3076 | 0.0 | 3352 | 2.5 | 3723 | 2.7 | 4147 | 0.0 |
| 3077 | 0.0 | 3355 | 0.0 | 3731 | 7.8 | 4150 | 5.3 |
| 3090 | 2.3 | 3356 | 0.0 | 3734 | 4.8 | 4158 | 0.0 |
| 3092 | 4.0 | 3365 | 4.9 | 3739 | 2.5 | 4161 | 0.0 |
| 3094 | 3.7 | 3367 | 3.5 | 3751 | 4.1 | 4166 | 3.6 |
| 3099 | 0.0 | 3374 | 5.1 | 3769 | 3.7 | 4176 | 5.4 |
| 3100 | 4.2 | 3390 | 3.9 | 3770 | 0.0 | 4180 | 11.1 |
| 3102 | 0.0 | 3391 | 5.1 | 3774 | 5.4 | 4184 | 4.8 |
| 3103 | 0.0 | 3393 | 4.9 | 3776 | 0.0 | 4187 | 9.1 |
| 3107 | 3.9 | 3397 | 0.0 | 3780 | 3.1 | 4191 | 2.4 |
| 3123 | 1.3 | 3401 | 12.7 | 3802 | 3.4 | 4193 | 0.0 |
| 3125 | 0.0 | 3414 | 2.5 | 3805 | 1.7 | 4196 | 0.0 |
| 3126 | 0.0 | 3421 | 0.0 | 3824 | 0.0 | 4202 | 2.5 |
| 3130 | 0.0 | 3423 | 2.8 | 3828 | 1.0 | 4205 | 0.0 |
| 3131 | 3.5 | 3424 | 3.7 | 3829 | 8.7 | 4210 | 4.8 |
| 3132 | 0.0 | 3425 | 0.0 | 3832 | 9.9 | 4214 | 0.0 |
| 3134 | 0.0 | 3427 | 4.6 | 3833 | 0.0 | 4232 | 0.0 |
| 3142 | 0.0 | 3429 | 4.4 | 3836 | 4.0 | 4241 | 3.1 |
| 3146 | 0.0 | 3434 | 0.0 | 3838 | 0.0 | 4249 | 3.6 |

Table C.4: Intrinsic radio sizes of COM AGN (continued)

| ID | D (kpc) | ID | D (kpc) | ID | D (kpc) | ID | D (kpc) |
|------|------------|------|------------|------|------------|------|------------|
| 4254 | 0.0 | 4674 | 8.8 | 5125 | 4.4 | 5756 | 6.0 |
| 4260 | 4.0 | 4675 | 3.1 | 5136 | 0.0 | 5761 | 0.0 |
| 4277 | 0.0 | 4680 | 0.0 | 5142 | 3.6 | 5763 | 0.0 |
| 4278 | 0.0 | 4683 | 0.0 | 5164 | 4.0 | 5767 | 4.1 |
| 4284 | 7.6 | 4689 | 4.5 | 5165 | 0.0 | 5775 | 3.9 |
| 4289 | 3.1 | 4701 | 5.4 | 5196 | 0.0 | 5779 | 0.0 |
| 4293 | 0.0 | 4703 | 10.9 | 5200 | 3.5 | 5794 | 4.9 |
| 4294 | 0.0 | 4710 | 0.0 | 5210 | 4.0 | 5814 | 3.9 |
| 4304 | 5.8 | 4713 | 4.6 | 5228 | 6.3 | 5824 | 0.0 |
| 4311 | 3.2 | 4720 | 4.4 | 5255 | 4.4 | 5828 | 4.7 |
| 4323 | 3.6 | 4739 | 3.0 | 5261 | 4.1 | 5830 | 4.9 |
| 4324 | 5.0 | 4760 | 3.9 | 5269 | 0.0 | 5834 | 0.0 |
| 4331 | 6.1 | 4761 | 4.8 | 5286 | 1.5 | 5840 | 0.0 |
| 4338 | 3.2 | 4764 | 3.0 | 5292 | 0.0 | 5845 | 4.6 |
| 4339 | 0.0 | 4766 | 4.1 | 5310 | 0.0 | 5846 | 0.0 |
| 4341 | 2.5 | 4774 | 0.0 | 5313 | 7.5 | 5867 | 5.5 |
| 4358 | 5.3 | 4781 | 2.7 | 5318 | 0.0 | 5871 | 4.8 |
| 4372 | 0.0 | 4786 | 12.0 | 5321 | 4.1 | 5872 | 6.2 |
| 4376 | 4.1 | 4802 | 4.8 | 5344 | 0.0 | 5877 | 3.9 |
| 4378 | 0.0 | 4812 | 2.9 | 5346 | 0.0 | 5883 | 8.7 |
| 4386 | 1.7 | 4813 | 0.0 | 5352 | 6.7 | 5886 | 10.6 |
| 4391 | 0.0 | 4817 | 7.0 | 5359 | 4.3 | 5912 | 3.1 |
| 4412 | 4.8 | 4819 | 0.0 | 5365 | 0.0 | 5913 | 0.0 |
| 4414 | 0.0 | 4822 | 3.4 | 5369 | 0.0 | 5922 | 5.1 |
| 4415 | 5.5 | 4832 | 4.4 | 5371 | 3.1 | 5926 | 5.7 |
| 4417 | 6.9 | 4834 | 3.5 | 5400 | 1.7 | 5931 | 2.4 |
| 4421 | 2.5 | 4837 | 3.9 | 5401 | 5.8 | 5941 | 4.3 |
| 4423 | 5.4 | 4838 | 5.6 | 5418 | 0.0 | 5945 | 4.8 |
| 4426 | 0.0 | 4845 | 3.9 | 5446 | 3.4 | 5956 | 0.0 |
| 4427 | 5.3 | 4855 | 6.0 | 5454 | 0.0 | 5957 | 0.0 |
| 4445 | 1.9 | 4865 | 0.0 | 5462 | 0.0 | 5959 | 7.4 |
| 4451 | 4.2 | 4872 | 7.0 | 5466 | 0.0 | 5963 | 4.2 |
| 4468 | 0.0 | 4895 | 4.9 | 5469 | 6.0 | 5991 | 2.4 |
| 4492 | 1.9 | 4897 | 10.0 | 5477 | 0.0 | 5992 | 0.0 |
| 4493 | 3.7 | 4898 | 3.8 | 5481 | 0.0 | 5995 | 0.0 |
| 4498 | 0.0 | 4901 | 0.0 | 5487 | 4.4 | 6001 | 0.0 |
| 4504 | 0.0 | 4912 | 2.4 | 5529 | 3.3 | 6003 | 4.3 |
| 4519 | 8.7 | 4928 | 4.2 | 5565 | 2.6 | 6017 | 2.9 |
| 4522 | 4.2 | 4931 | 2.4 | 5567 | 4.1 | 6020 | 0.0 |
| 4544 | 2.6 | 4936 | 2.1 | 5576 | 4.6 | 6031 | 4.8 |
| 4554 | 8.0 | 4939 | 4.2 | 5581 | 8.6 | 6050 | 4.7 |
| 4556 | 5.2 | 4941 | 2.8 | 5597 | 4.7 | 6054 | 0.0 |
| 4565 | 3.2 | 5001 | 3.0 | 5604 | 0.0 | 6058 | 3.1 |
| 4573 | 2.1 | 5005 | 0.0 | 5605 | 3.8 | 6083 | 7.5 |
| 4574 | 0.0 | 5017 | 5.5 | 5609 | 0.0 | 6118 | 3.6 |
| 4584 | 9.0 | 5018 | 0.0 | 5610 | 6.5 | 6129 | 3.8 |
| 4595 | 4.1 | 5020 | 6.2 | 5614 | 0.0 | 6131 | 5.4 |
| 4599 | 5.0 | 5028 | 3.3 | 5616 | 0.0 | 6133 | 3.7 |
| 4606 | 2.4 | 5041 | 4.0 | 5633 | 0.0 | 6142 | 0.0 |
| 4611 | 0.0 | 5049 | 0.0 | 5638 | 4.1 | 6149 | 2.2 |
| 4612 | 3.9 | 5051 | 3.7 | 5648 | 0.0 | 6159 | 0.0 |
| 4626 | 2.7 | 5052 | 5.2 | 5654 | 7.3 | 6161 | 0.0 |
| 4629 | 0.0 | 5076 | 1.6 | 5659 | 2.5 | 6166 | 4.4 |
| 4630 | 4.2 | 5079 | 3.7 | 5667 | 5.5 | 6177 | 0.9 |
| 4634 | 0.0 | 5088 | 4.5 | 5673 | 7.4 | 6179 | 3.6 |
| 4644 | 0.0 | 5103 | 0.0 | 5686 | 0.0 | 6189 | 4.5 |
| 4646 | 0.0 | 5110 | 0.0 | 5700 | 3.3 | 6218 | 8.7 |
| 4649 | 5.4 | 5116 | 4.6 | 5701 | 0.0 | 6219 | 6.7 |
| 4659 | 2.0 | 5118 | 3.5 | 5725 | 0.0 | 6224 | 0.0 |
| 4666 | 3.1 | 5124 | 0.0 | 5749 | 9.7 | 6228 | 0.0 |

Table C.4: Intrinsic radio sizes of COM AGN (continued)

| ID | <i>D</i> (kpc) | ID | <i>D</i> (kpc) | ID | <i>D</i> (kpc) | ID | <i>D</i> (kpc) |
|------|-------------------|------|-------------------|------|-------------------|------|-------------------|
| 6231 | 7.8 | 6860 | 0.0 | 7757 | 0.0 | 8338 | 0.0 |
| 6232 | 0.0 | 6880 | 0.0 | 7779 | 0.0 | 8341 | 0.0 |
| 6240 | 2.9 | 6906 | 3.9 | 7781 | 9.5 | 8355 | 7.1 |
| 6263 | 6.8 | 6930 | 7.5 | 7787 | 3.9 | 8356 | 0.0 |
| 6283 | 3.0 | 6933 | 12.6 | 7788 | 8.5 | 8361 | 0.0 |
| 6286 | 0.0 | 6935 | 3.2 | 7802 | 0.0 | 8365 | 0.0 |
| 6318 | 0.0 | 6945 | 0.0 | 7813 | 5.1 | 8372 | 3.8 |
| 6319 | 4.9 | 6961 | 7.3 | 7821 | 7.4 | 8373 | 4.9 |
| 6345 | 5.0 | 6964 | 6.7 | 7830 | 6.0 | 8384 | 0.0 |
| 6346 | 3.6 | 7001 | 2.7 | 7831 | 0.0 | 8410 | 5.5 |
| 6348 | 0.0 | 7013 | 4.7 | 7843 | 7.5 | 8429 | 9.7 |
| 6361 | 0.0 | 7016 | 0.0 | 7845 | 2.9 | 8457 | 0.0 |
| 6377 | 6.5 | 7020 | 4.9 | 7846 | 5.7 | 8489 | 13.0 |
| 6391 | 3.2 | 7021 | 2.8 | 7851 | 0.0 | 8510 | 5.8 |
| 6400 | 4.1 | 7031 | 0.0 | 7852 | 0.0 | 8542 | 4.5 |
| 6401 | 9.1 | 7043 | 7.9 | 7854 | 0.0 | 8555 | 0.0 |
| 6404 | 5.9 | 7056 | 4.0 | 7855 | 11.3 | 8557 | 0.0 |
| 6413 | 3.5 | 7059 | 0.0 | 7886 | 6.7 | 8584 | 0.0 |
| 6434 | 5.1 | 7070 | 5.1 | 7905 | 5.3 | 8599 | 0.0 |
| 6449 | 6.1 | 7080 | 0.0 | 7915 | 6.1 | 8602 | 7.0 |
| 6456 | 0.0 | 7088 | 3.5 | 7947 | 6.1 | 8628 | 11.3 |
| 6482 | 4.8 | 7098 | 0.0 | 7968 | 6.4 | 8632 | 1.1 |
| 6484 | 6.5 | 7119 | 0.0 | 7977 | 13.1 | 8635 | 4.2 |
| 6495 | 0.0 | 7123 | 0.0 | 7983 | 0.0 | 8637 | 0.0 |
| 6514 | 0.0 | 7134 | 0.0 | 8002 | 8.0 | 8651 | 6.3 |
| 6517 | 0.0 | 7156 | 0.0 | 8004 | 8.9 | 8673 | 0.0 |
| 6521 | 0.0 | 7168 | 5.3 | 8009 | 0.0 | 8675 | 0.0 |
| 6529 | 0.0 | 7178 | 3.0 | 8028 | 4.5 | 8692 | 0.0 |
| 6538 | 3.8 | 7244 | 0.0 | 8033 | 0.0 | 8713 | 0.0 |
| 6559 | 6.3 | 7253 | 6.4 | 8034 | 3.0 | 8714 | 0.0 |
| 6568 | 0.0 | 7258 | 7.1 | 8039 | 0.0 | 8730 | 5.2 |
| 6582 | 2.7 | 7268 | 8.9 | 8044 | 0.0 | 8738 | 7.3 |
| 6583 | 4.0 | 7274 | 0.0 | 8045 | 0.0 | 8751 | 8.3 |
| 6586 | 5.2 | 7308 | 7.4 | 8048 | 5.3 | 8760 | 0.0 |
| 6587 | 0.0 | 7317 | 3.1 | 8060 | 0.0 | 8762 | 0.0 |
| 6594 | 0.0 | 7326 | 4.1 | 8077 | 4.6 | 8776 | 0.0 |
| 6596 | 5.0 | 7362 | 1.8 | 8086 | 6.6 | 8785 | 8.5 |
| 6602 | 5.4 | 7367 | 5.5 | 8139 | 0.0 | 8786 | 0.0 |
| 6607 | 3.9 | 7406 | 5.3 | 8144 | 8.1 | 8788 | 8.1 |
| 6614 | 0.0 | 7450 | 2.7 | 8148 | 2.2 | 8830 | 0.0 |
| 6623 | 4.8 | 7454 | 6.8 | 8152 | 0.0 | 8849 | 0.0 |
| 6653 | 3.1 | 7466 | 0.0 | 8159 | 4.4 | 8856 | 4.7 |
| 6657 | 0.0 | 7483 | 6.1 | 8162 | 11.7 | 8880 | 5.8 |
| 6658 | 4.3 | 7490 | 0.0 | 8167 | 3.3 | 8887 | 0.0 |
| 6659 | 5.3 | 7518 | 6.8 | 8176 | 0.0 | 8908 | 0.0 |
| 6665 | 5.0 | 7543 | 0.0 | 8189 | 0.0 | 8919 | 0.0 |
| 6672 | 5.7 | 7549 | 7.8 | 8192 | 0.0 | 8920 | 4.9 |
| 6674 | 0.0 | 7589 | 0.0 | 8198 | 7.3 | 8928 | 4.8 |
| 6676 | 0.0 | 7600 | 0.0 | 8207 | 0.0 | 8934 | 0.0 |
| 6709 | 8.7 | 7613 | 8.4 | 8209 | 10.0 | 8936 | 2.7 |
| 6712 | 0.0 | 7617 | 0.0 | 8255 | 4.2 | 8938 | 0.0 |
| 6732 | 2.9 | 7626 | 3.4 | 8257 | 6.3 | 8951 | 6.2 |
| 6736 | 5.6 | 7627 | 0.0 | 8258 | 8.8 | 8968 | 5.2 |
| 6764 | 0.0 | 7632 | 5.3 | 8292 | 3.2 | 8983 | 0.0 |
| 6775 | 3.9 | 7634 | 4.2 | 8302 | 7.9 | 8992 | 0.0 |
| 6782 | 0.0 | 7644 | 12.3 | 8305 | 7.7 | 9006 | 5.0 |
| 6788 | 4.3 | 7693 | 0.0 | 8312 | 3.7 | 9007 | 6.0 |
| 6815 | 4.8 | 7704 | 3.5 | 8324 | 0.0 | 9019 | 4.1 |
| 6836 | 8.5 | 7713 | 0.0 | 8332 | 0.0 | 9020 | 5.9 |
| 6857 | 4.3 | 7724 | 5.4 | 8337 | 6.7 | 9026 | 4.8 |

Table C.4: Intrinsic radio sizes of COM AGN (continued)

| ID | <i>D</i> (kpc) | ID | <i>D</i> (kpc) | ID | <i>D</i> (kpc) |
|------|-------------------|-------|-------------------|-------|-------------------|
| 9029 | 0.0 | 9851 | 6.5 | 10629 | 0.0 |
| 9059 | 2.8 | 9853 | 0.0 | 10631 | 0.0 |
| 9063 | 0.0 | 9890 | 0.0 | 10633 | 0.0 |
| 9069 | 0.0 | 9899 | 0.0 | 10637 | 0.0 |
| 9074 | 7.7 | 9909 | 6.2 | 10696 | 0.0 |
| 9103 | 0.0 | 9925 | 0.0 | 10698 | 0.0 |
| 9106 | 6.0 | 9933 | 0.0 | 10734 | 0.0 |
| 9113 | 0.0 | 9938 | 10.0 | 10748 | 0.0 |
| 9120 | 6.3 | 9947 | 0.0 | 10754 | 0.0 |
| 9123 | 15.5 | 9965 | 0.0 | 10765 | 0.0 |
| 9124 | 4.2 | 9985 | 0.0 | 10781 | 5.2 |
| 9135 | 8.8 | 10010 | 2.4 | 10811 | 0.0 |
| 9138 | 0.0 | 10026 | 0.0 | 10814 | 0.0 |
| 9141 | 0.0 | 10048 | 4.7 | 10824 | 0.0 |
| 9144 | 0.0 | 10054 | 0.0 | 10843 | 0.0 |
| 9151 | 5.0 | 10074 | 0.0 | 10857 | 0.0 |
| 9164 | 8.5 | 10075 | 0.0 | 10896 | 0.0 |
| 9201 | 10.6 | 10077 | 3.7 | 10946 | 6.4 |